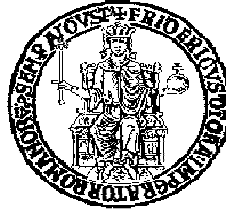


University of Naples “Federico II”

Faculty of Engineering



Department of Chemical, Materials and Industrial Production Engineering

PHD IN MATERIALS AND STRUCTURES ENGINEERING

XXV CYCLE

**A NOVEL ROUTE TOWARDS THE DESIGN OF
3D MORPHOLOGICALLY CONTROLLED MAGNETIC
SCAFFOLDS FOR ADVANCED BONE TISSUE ENGINEERING**

Coordinator:

Prof. G. Mensitieri

Supervisor:

Prof. P. A. Netti

Tutor:

Prof. A. Gloria

Prof. R. De Santis

Prof. L. Ambrosio

Author:

Ugo D'Amora

*"Scegliamo il nostro mondo successivo in base a ciò che noi apprendiamo in questo.
Se non impari nulla, il mondo di poi sarà identico a quello di prima, con le stesse limitazioni."*

Richard Bach
da *"Il gabbiano Jonathan Livingston"*

Table of Contents

Preface	1
Chapter 1	5
State of the Art	5
1.1 Tissue Engineering and Regenerative Medicine.....	5
1.2 Cell-material interaction	8
1.3 Physical and chemical properties of scaffolds for tissue engineering applications	10
1.4 Bone tissue: structure-properties relationship.....	12
1.5 Bone tissue engineering: from conventional approaches to magnetic scaffolds	19
1.6 Scaffold preparation techniques.....	25
1.6.1 3D fiber deposition technique	28
References	34
Chapter 2	43
A basic approach in the development of poly(ϵ-caprolactone)/iron oxide nanocomposite magnetic scaffolds	43
Preface	43
2.1 Materials and Methods	44
2.1.1 Poly(ϵ -caprolactone).....	44
2.1.2 Iron oxide nanoparticles.....	47
2.1.3 Design and preparation of PCL/Fe ₃ O ₄ nanocomposite scaffolds.....	49
2.1.4 Morphological Analysis: Micro-CT and Optical Imaging.....	50
2.1.5 Tensile Tests on PCL/Fe ₃ O ₄ nanocomposite fibers.....	50
2.1.6 Compression Tests on PCL/Fe ₃ O ₄ nanocomposite scaffolds.....	51
2.1.7 Magnetic Analysis	51
2.1.8 Biological Analysis.....	52
2.2 Results and Discussion	53

II

2.2.1 Morphological Analysis: Micro-CT and Optical Imaging.....	53
2.2.2 Tensile Tests on PCL/Fe ₃ O ₄ nanocomposite fibers.....	54
2.2.3 Compression Tests on PCL/Fe ₃ O ₄ nanocomposite scaffolds	56
2.2.4 Magnetic Analysis	57
2.2.5 Biological Analysis.....	58
Conclusions	60
References	61
Chapter 3.....	65
Poly(ϵ-caprolactone)/iron-doped hydroxyapatite nanocomposite magnetic substrates	65
Preface	65
3.1 Materials and Methods	67
3.1.1 Iron-doped hydroxyapatite synthesis.....	67
3.1.2 Design and preparation of PCL/FeHA nanocomposite substrates	69
3.1.3 Morphological Analysis: SEM/EDS and Micro-CT	70
3.1.4 Contact Angle Measurements	70
3.1.5 Small Punch Tests	71
3.1.6 Magnetic Analysis	71
3.1.7 Biological Analysis.....	72
3.2 Results and Discussion	75
3.2.1 Morphological Analysis: SEM/EDS and Micro-CT	76
3.2.2 Contact Angle Measurements	78
3.2.3 Small Punch Tests	79
3.2.4 Magnetic Analysis	81
3.2.5 Biological Analysis.....	84
Conclusions	88
References	90

Chapter 4.....	93
From the design of 2D substrates to 3D poly(ϵ-caprolactone)/iron-doped hydroxyapatite nanocomposite magnetic scaffolds.....	93
Preface	93
4.1 Materials and Methods	94
4.1.1 Design and preparation of 3D PCL/FeHA nanocomposite scaffolds.....	94
4.1.2 Morphological Analysis: SEM and TEM	95
4.1.3 Compression Tests on PCL/FeHA nanocomposite scaffolds	95
4.1.4 Biological Analyses	96
<i>4.1.4.1 The effect of a sinusoidal magnetic field on cell adhesion and proliferation</i>	<i>96</i>
<i>4.1.4.2 Magnetically-charged cells and magnetic scaffolds: Scaffold-cell loading</i>	<i>102</i>
4.2 <i>In vivo</i> experiments and histological analysis.....	104
4.3 Results and Discussion	106
4.3.1 Morphological Analysis: SEM and TEM	106
4.3.2 Compression Tests on PCL/FeHA nanocomposite scaffolds	107
4.3.3 Biological Analyses	108
<i>4.3.3.1 The effect of a sinusoidal magnetic field on cell adhesion and proliferation</i>	<i>108</i>
<i>4.3.3.2 Magnetically-charged cells and magnetic scaffolds: Scaffold-cell loading</i>	<i>112</i>
4.4 <i>In vivo</i> experiments and histological analysis.....	114
Conclusions	115
References	117
Conclusions and Future Trends	123
Appendix	127
References	142

Preface

Tissue engineering is an interdisciplinary field that has the goal of creating new tissues and organs. Ideal bone *scaffold*, which is the key element, should possess important chemical, biochemical and biophysical properties, but the biomechanical environment introduces another level of complexity. Scaffold needs to be able to withstand external forces, and it is known that bone regeneration, modeling and remodeling is mediated by mechanical stimuli known as mechanotransduction. Mechanical stimuli transferred by scaffolds to cells rely exclusively on intrinsic scaffold properties, such as material stiffness and architecture. Consequently, the introduction of rapid prototyping technologies in the biomedical field has allowed to obtain scaffolds characterized by a precise control of its internal architecture, including precise pore size, pore geometry, spatial distribution of pores and interconnectivity, which may be considered as critical features to their *in vivo*, biological and mechanical performances.

In order to obtain a complete histomorphologically and biologically mature tissue, as bone, the restoration of the mechanical resistance to physiological stresses should be also followed by angiogenesis, which is a crucial aspect in the development of regenerative medicine approaches that require rapid vascularization of tissue-engineered structures.

The main driving idea of this work is creating a conceptually new type of bioactive scaffold able to be manipulated *in situ* by means of magnetic forces in order to repair large bone defects and osteochondral lesions. **Chapter 1** has been focused on the State of the Art, whilst **Chapter 2** deals with a preliminary approach in the design of a magnetic scaffold for advanced bone tissue engineering providing new opportunity in terms of scaffold fixation and functionalization. The first kind of scaffold, which was obtained by embedding iron oxide (Fe_3O_4) magnetic nanoparticles in a poly(ϵ -caprolactone) (PCL) matrix, was designed and developed through a rapid prototyping

technique (3D fiber deposition). To avoid the dangerous problem of leaving any non bioresorbable magnetic inclusion, as in the case of magnetite, inside the repaired tissue, materials as iron-doped hydroxyapatite nanoparticles (FeHA) have been employed. **Chapter 3** and **Chapter 4** basically describe the effect of the inclusion of FeHA nanoparticles embedded in the PCL matrix on the mechanical, morphological, magnetic and biological performances. In a first analysis, the study has involved the design, the preparation and the characterization of magnetic substrates obtained through molding and solvent casting techniques employing different polymer-to-particle weight ratios. Successively, the selected polymer-to-nanoparticle weight ratio, showing the best compromise between mechanical, magnetic and biological performances, has been employed to develop 3D morphologically controlled nanocomposite magnetic scaffolds. Finally, in the last part of Chapter 4, *in vitro* and *in vivo* biological analyses have shown interesting results.

Chapter 1

State of the Art

1.1 Tissue Engineering and Regenerative Medicine

Tissue engineering and regenerative medicine (TERM) is an interdisciplinary field that involves cell biology, materials science, reactor engineering, medicine, and clinical research with the goal of creating new tissues and organs.¹ Due to the limitations of traditional treatments based on organ transplantation and biomaterial implantation,^{2,3} it aims to produce “artificial” organs and tissue substitutes that can grow with the patient, without causing adverse reactions.² The concept of “scaffolding” was firstly introduced by Barth in 1893.⁴ He indicated as *scaffold* a porous matrix or an implant in which cells can infiltrate and regenerate the local tissue. In these terms, scaffold acts as a temporary extracellular matrix (ECM) during the process of new tissue growth.^{5,6} In the last two decades, with the term *scaffold* researchers have indicated natural and synthetic structures that can temporarily support cells and the release of biological factors that can regulate tissue growth.

In tissue engineering, two important strategies are usually pursued. The first is based on seeding cells *in vitro* on a synthetic three-dimensional (3D) scaffold that acts as a template and stimulus for tissue regeneration. The cell-construct is then implanted into the patient where, degrading into nontoxic products, it allows cells to produce their own extracellular matrix (Figure 1). On the contrary, a second strategy is based on implanting a scaffold, mainly resorbable, *in situ*, directly into a defect site. In this case, the body is used as its own bioreactor.^{3,7}

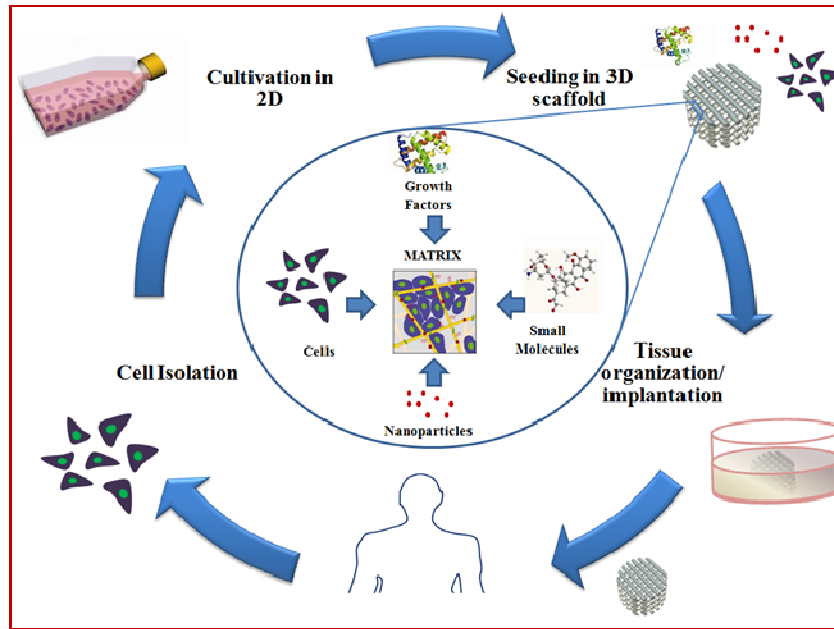


Figure 1: Tissue engineering approach.

However, scaffold should be considered as the key element for *in vitro* or *in vivo* tissue regeneration.

Therefore, the design of scaffolds able to guide the process of tissue growth represents one of the most challenging goals. The ideal scaffold should possess a set of chemical, biochemical and biophysical properties able to control and promote specific events at the cellular level.^{8,9} Scaffold should be easily manufactured into a variety of shapes and sizes, it should not induce adverse reactions, it should exhibit biocompatibility, tailored biodegradability and/or bioresorbability and, finally, it should have suitable mechanical properties and appropriate morphology and surface chemistry.^{5,8,10,11}

A wide range of biomaterials is being investigated for TERM scaffolds.^{5,10-12}

Natural, synthetic, semi-synthetic and hybrid materials have been widely proposed and tested as scaffolds for tissue regeneration.⁸ Synthetic and natural polymers may be considered as an attractive alternative to the growth of most tissues. Natural polymers used in tissue engineering include collagen, alginate, agarose, chitosan, fibrin, and hyaluronic acid.

Unlike natural polymers, synthetic polymers are man-made polymers that may present several advantages such as more flexibility and processability. The physico-chemical, mechanical and degradation properties can be tailored. Among all the biodegradable polymers, poly(lactic acid) (PLA), poly(glycolic acid) (PGA), their copolymer (PLGA) and poly(ϵ -caprolactone) (PCL) are the most commonly used polymers for tissue engineering. If compared to ceramic scaffolds, polymeric scaffolds turned out to be too flexible, while the ceramic ones tended to be too brittle.^{8,13,14} Consequently, research attention has been focused on composite materials consisting of polymers reinforced with inorganic ceramic fillers. Different polymer-based composites have been studied for biomedical applications. Specific advantages have been obtained in using polymer-based composite biomaterials that are also called “biocomposites”.^{8,15,16}

Compared to neat polymers, composites should present improved mechanical properties, better flexibility and structural integrity than brittle ceramic materials.

In particular, typical biomaterials for bone and cartilage tissue engineering include hydroxyapatite, calcium carbonate and bioactive glass.

Even though these ceramic materials resemble the natural inorganic component of bone and possess osteoconductivity^a properties,^{8,17,18} they are brittle and cannot match the mechanical properties of bone. Furthermore, ceramic scaffolds have also been found to be unsuitable for the growth of soft tissues that are characterized by different cellular receptors and mechanical performances than hard tissues. However, none of these materials used on their own can satisfy all the goals required for creating optimal tissue scaffolding, such as suitable fracture strength, stiffness, toughness, osteoinductivity^b, osteoconductivity as well as *in vitro* and *in vivo* controlled rate of degradation.⁵

Therefore, the tailored combination of biomaterials to form biocomposite is being increasingly considered for the development of optimal scaffolds.^{5,19,20}

^a ability to support bone growth and encourage the ingrowth of surrounding bone

^b ability to initiate bone formation in a non-bone site

1.2 Cell-material interaction

A bidirectional complex combination of events takes place between the material and the biological environment, once it is implanted. The success of a biomaterial depends on its interactions with the physiological fluids and cells. Cell-material interaction process consists of different stages.

In a first stage, which is highly dependent on the material surface properties, the initial contact takes place between material surface and water molecules forming a water coating layer.

The successive stage consists of the interaction of all the macromolecules existing in the physiological medium, namely sugars, lipids, proteins with the material surface. During this stage, the “Vroman effect”^c takes place and the material surface is covered by an adsorbed layer of proteins. Biocompatibility and material interactions with biological entities are dependent on the proteins adsorbed to the surface. By this point of view, surface features, surface energy and chemical composition of the material strongly influence cell-material interaction process determining the nature of the proteins adsorbed to the surface and their orientation and conformation which are crucial parameters.

Finally, a third stage occurs, during which, cells get in contact with the material and interact with it. Cell-material interaction takes place through cell adhesion proteins known as integrins that interact with particular peptide motifs from the protein adsorbed to the material surface.

Integrins are cell transmembrane proteins that possess two glycoproteic units (α and β) and three domains (cytoplasmatic, transmembrane and the extracellular one). The extracellular domains of the α and β units possess receptors for the specific recognition of cell adhesive peptides motifs that are contained in some adhesive proteins present in the ECM.^{21,23}

Thus, cell attachment and proliferation are integrin-mediated processes. Although integrins are the first contact point between cells and the material surface, cell interaction with the material surface is carried out through their cytoplasm, specifically through cell structures named *lamellipodia* or

^c Dynamic process that regulates the absorption of serum on a surface. In particular, firstly proteins with low weight and high concentration are adsorbed. These proteins are then replaced by more large proteins with low concentration but a greater affinity for the surface.

pseudopodia which are cell extensions formed by actin filaments.^{21,24} *Filopodia* are the actuators of the adhesion, morphology, spreading and motility processes. Integrins, located within these long and thin cytoplasm extensions, interact with the substrate surface creating focal contacts that are points where several integrin receptors meet to form stronger adhesion points. The just described mechanism is schematically reported in figure 2. The cell is rounded at the beginning (A), then assumes an expanse form and results well spread (B).

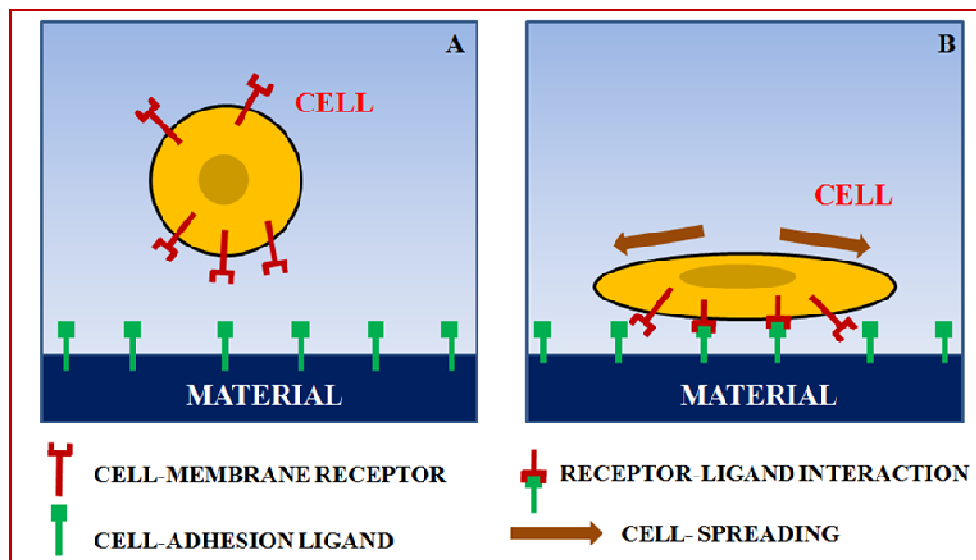


Figure 2: Cell-material interactions.

A biocomposite material should be able to activate specific processes by the generation of signals that trigger different cascades through these surfaces receptors. In this sense, the composite should be able to deliver biochemical and/or biophysical signals, which could be the constituents of the composite. In addition to the surface properties, there are other physical and chemical features related to the intrinsic properties that also affect the tissue regeneration process.²¹

1.3 Physical and chemical properties of scaffolds for tissue engineering applications

In order to replicate the original morphology and structure of the damaged tissue for promoting the integration with the surrounding biological environment, scaffolds should be easily manufactured into a variety of shapes and sizes.^{5,8,10,11}

Mechanical properties of the bioresorbable scaffold-tissue construct at the time of implantation should match that of the host tissue as closely as possible. It may be required to provide sufficient initial mechanical strength and stiffness to substitute the diseased or damaged tissue for a period until the *in vivo* tissue ingrowth has replaced the slowly vanishing scaffold matrix.²⁵

An important feature in the design of scaffolds for TERM applications is their 3D porous architecture. To favor tissue integration and vascularization, scaffold should be characterized by interconnecting pores of the right scale, in which cells reside.^{5,26} It is recognized that highly porous and interconnected structures are required to allow cell seeding and migration throughout the entire scaffold. The combination of different pore sizes in hierarchical 3D structures allows not only the growth and the colonization of the relevant cells but also capillary ingrowth for vascularization of the new tissues, as well as the path of diffusion of nutrients and metabolic waste.^{5,27} In particular, pore shape and dimension influence cell differentiation. Small pores (100-200 μm) favor hypoxic conditions and induce chondrogenesis differentiation. In contrast, large pores (300-400 μm) rapidly induce vascularization and lead to direct osteogenesis.²⁵

Mechanical properties, microstructure, 3D porosity are not the only factors that determine the success of a scaffold. Cell response in contact with a solid surface is affected by the surface physico-chemical parameters such as surface energy, surface charges, and chemical composition.

Surface topography is one of the most important cues for cells.^{5,28}

The primary cell-material interaction is strongly dependent on the material surface roughness, where the presence of nanoscale features plays a key role. Although cells have micrometer dimensions, they get *in vivo* in close contact with the ECM, and its topographical/structural features

of nanometer size.^{5,28} Consequently, there is increasing interest in developing methods to modify biomaterial in order to mimic the nanoscale topographical features presented to cells. These nanoscale surface features should promote functions such as cell adhesion, mobility and differentiation.⁵

Surface chemistry together with surface topography play an important role in the scaffold design. Biological tissues consist of cells immersed in the extracellular matrix, which is a complex mixture of proteins and glycosaminoglycans with both mechanical and signaling functions. Integrin heterodimers bind to specific amino acid sequences, such as the arginine-glycine-aspartic acid (RGD) recognition motif that is largely present in many ECM proteins.^{29,30,31} Thus, small synthetic peptides that contain the RGD amino acid sequence can mediate cell attachment as well as the large parental molecule.^{29,30}

Benefiting from this basis, great efforts have been made to develop surface treatment approach (i.e. aminolysis) and biomimetic approaches for conjugating short peptides (i.e. RGD) onto synthetic or natural substrates, the aim being to obtain multifunctional biomaterials able to promote and improve cell attachment.^{29,32,33}

Functional groups exposed at the material surface are responsible for surface properties such as wettability, surface electrical charges and free energy that in turn influence protein adsorption and cell behavior. Thus, by tailoring the functional groups available at the material surface, it is possible to modify and enhance protein-surface interactions.²⁵

One of the most important chemical cues that a scaffold should possess is a tailored biodegradability and/or bioresorbability. Scaffold should exhibit a degradation rate that matches the tissue growth rate in order to maintain the mechanical strength and to avoid the collapse or the stress shielding effect. Besides, the material has to be degradable over an appropriate timescale into products that can be metabolized or excreted. Degradation rate is highly dependent on the intrinsic properties of the material. Polymer biodegradability is mainly originated by hydrolysis of the polymer backbone and to a lesser extent by enzymatic activity.^{21,34} Degradation rate depends on

polymer crystallinity, molecular weight, thermal history, porosity, monomer concentration, geometry and location of the implant. In an aqueous environment, water penetrates the bulk of the polymer sample and attacks the chemical bonds of the amorphous phase, shortening the polymer chains.²¹ Crystalline regions remain and support the physical properties of the device until water attacks the crystalline regions. In a second stage, enzymatic attack takes place. Several studies have shown that the incorporation of an inorganic phase into a polymeric matrix not only modifies the mechanical performances of the porous structure^{21,35} and enhances the bioactivity of the scaffold, but also changes the degradation pattern of the polymer.

1.4 Bone tissue: structure-properties relationship

Bone is a dynamic, highly vascular and mineralized connective tissue which, together with cartilage, builds up the skeletal system. Its main functions are to provide mechanical support, protection of vital organs and a site of muscle attachment for locomotion. Furthermore, bone tissue serves as a mineral reservoir of calcium and phosphate.³⁶

Bone is a natural hybrid hierarchical nanocomposite (Figure 3), with the lowest level belonging to the nanoscale range that consists in a mineral component, hydroxyapatite nanocrystals, dispersed in an organic matrix formed predominantly of oriented collagen.

Consequently, in order to understand the mechanical properties of bone material, it is important to understand the mechanical properties of its constituents, and the structural relationship between them at the various levels of the hierarchical structural organization.³⁷

These levels and structures are:

- ✓ the subnanostructure (<100 nm): molecular structure of constituent elements, such as mineral, collagen, and non-collagenous organic proteins;
- ✓ the nanostructure (100 nm–1 μm): fibrillar collagen and embedded mineral;
- ✓ the sub-microstructure (1–10 μm): *lamellae*;
- ✓ the microstructure (10 to 500 μm): Haversian systems, osteons, single *trabeculae*;

✓ the macrostructure: cancellous and cortical bone.

This structure gives bone its balance of stiffness, toughness, and vibrational damping properties.^{38,39}

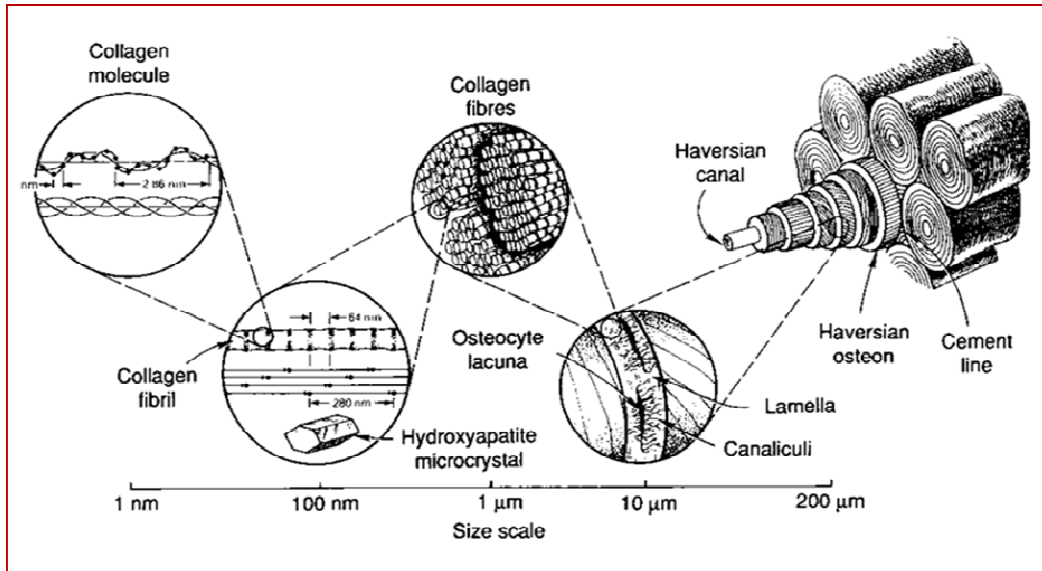


Figure 3: Hierarchical structure of human bone.⁴⁰

Bone consists of approximately 70% of inorganic and 30% of organic components.

The mineral component of bone is an analogue of the naturally occurring mineral hydroxyapatite (HA) in the form of spindle- or plate-shaped crystals.

The unit cell of HA has the following formula: $\text{Ca}_{10}(\text{PO}_4)_6(\text{OH})_2$. However, the natural mineral component of bone consists in biological apatites that are poorly crystalline and contain anionic and cationic substitutions in the sites of HA crystal structure, thus resulting far from the typical stoichiometric HA.⁴¹ Natural bone shows a Ca:P molar ratio ranging from 1.3:1 to 1.9:1.

The organic matrix is composed of proteoglycans (type I and type II), glycoproteins (osteonectin, alkaline phosphatase, fibronectin, sialoproteins, γ -carboxyglutamic acid based proteins (or “Gla” proteins as osteocalcin) and type I collagen.^{42,43}

90 % of organic matrix is represented by macromolecular chains of collagen which are arranged in the triple helix structure of tropocollagen, stabilized by hydrogen bonding between the amide

14 - Chapter 1

groups and the matrix water. The helical structure of tropocollagen stops the polyamide chains from collapsing into a random coil structure and facilitates the orientation of collagen in biological tissues such as bone.³⁸

Only 2% of the organic fraction consists of cells, growth factors and cytokines, such as Fibroblast Growth Factors (FGFs), Platelet-Derived Growth Factors (PDGFs), Transforming Growth Factor-Beta (TGF β) and Bone Morphogenic Proteins (BMPs).

Depending on the collagen fibers arrangement, bone tissue can be classified as non-lamellar bone and lamellar bone tissue.

The first one is characterized by the presence of collagen fibers randomly arranged, gathered in large bundles, parallel or twisted without any definite orientation. It can be found in the embryo and *fetus* or into the bone that is formed temporarily after a fracture.

The latter, on the other hand, has collagen fibers oriented tidily in a single direction.

The lamellar bone tissue is mainly found in the bones of adult mammals. In the adult skeleton, it is arranged in two architectural forms: cortical or compact bone (around 80% of the total skeleton) and trabecular, or spongy bone also called cancellous (around 20% of the total skeleton).⁴²

The proportions of these two architectural forms differ at various locations in the skeleton.

Cortical bone is a thick and dense protective layer of calcified tissue which has a high resistance to bending and torsion, thus is almost solid, being only 10% porous.⁴² It is an anisotropic material, which shows mechanical properties depending on the load direction. Its basic unit is an “osteon” (Figure 4), which is also known as a “Haversian System”. Each Haversian system has a cylindrical structure that consists of four parts:

1. A central tube called as Haversian Canal, which contains blood vessels and nerves. There are also other canals, named Volkmann canals, which extend in an oblique direction with respect to Haversian ones.
2. *Lamellae*, are concentric rings of a strong matrix formed from mineral salts including calcium, phosphates and collagen fibers. They surround the Haversian Canal.

3. *Lacunae*, the small spaces between the *lamellae* in which the bone cells (called “osteocytes”) are located. *Lacunae* are linked together by minute channels called *canaliculi*.
4. *Canaliculi*, minute channels, by which nutrients can reach the osteocytes and waste products can leave them.

In cortical bone the mechanical properties are influenced greatly by the porosity, the mineralization level and the organization of the solid matrix. In general, at the macrostructural level, the mechanical properties vary from one bone to another as well as within different regions of the same bone.^{37,44,45}

For example, the average values of strength and elastic modulus of human long bones (*tibia*, and femur) evaluated in compression are about 200 MPa and 20 GPa, respectively, while in tension they are about 144 MPa and 18 GPa.³⁸

At microstructural level, the results, obtained from mechanical tests performed on compact bone, have shown that tensile Young's modulus and stress at break are greater in the osteons characterized by oriented longitudinally *lamellae*, while compression tests have shown that these values are greater in osteons characterized by oriented transversely *lamellae*.^{46,47}

Bending tests have revealed that osteons with a transverse arrangement of the *lamellae* have greater stiffness but faster fracture mechanisms, while osteons with a longitudinal arrangement of the *lamellae* show significant deformation at break and a higher resistance to torsion.^{48,49}

On the other end, **trabecular bone** is arranged in a spongy-like form, with a honeycomb form, plates and rods of various sizes called *trabeculae* (Figure 4). As cortical bone, it is an anisotropic material, which shows mechanical properties depending on the anatomical site, the load direction and the conditions under which tests are carried out. Trabecular bone presents a higher porosity, 50-90%, higher elasticity, consequently, its modulus and ultimate compressive strength are around 20 times inferior to those of cortical bone.^{42,43} Furthermore, the tensile stiffness of trabecular bone is significantly smaller than that in compression.^{50,51}

16 - Chapter 1

The values of tensile strength and elastic modulus of cancellous bone are much lower than the corresponding values obtained for cortical bone. For example, as for the human distal femur, the values of tensile strength and elastic modulus are about 6 and 400 MPa.⁵²

At the level of single *trabeculae* the assessment of mechanical properties is quite a challenging task. Mechanical tests performed on individual *trabeculae* have shown values for the Young's modulus between 1 GPa and 15 GPa. The cause of this broad discrepancy in Young's modulus results might be in sample preparation, different testing protocols or anisotropy and asymmetry of the microsamples.⁵²

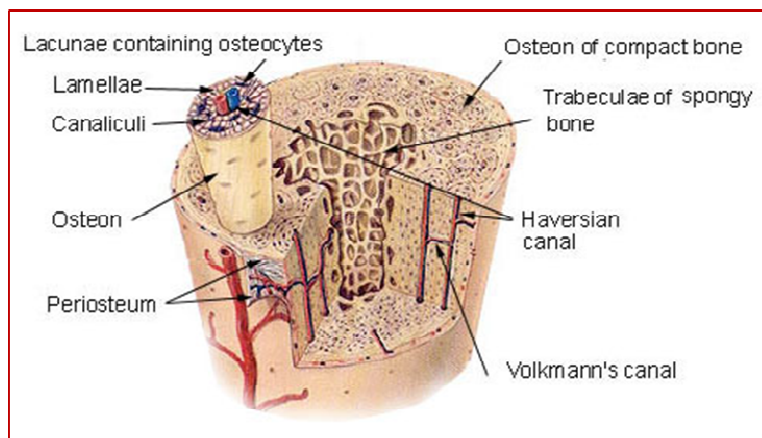


Figure 4: Schematic picture of bone structure showing *lamellae*, *trabeculae* and osteons.

Anatomically, bones are classified as: long bones (femur and *tibia*), short bones (wrist and ankle) and flat bones (skull vault and irregular bones). All these bone types, regardless of their anatomical form, are composed of both spongy and compact bone.⁴²

Trabecular bone is commonly found in the vertebral bodies, in short bones, flat bones and in the epiphyses of long bones (the proximal and distal ends of all long bones) covered by cortical bone, which can be also found in the diaphysis (central part) of long bones and in flat bones.⁴² The external surface of all bones is covered with the *periosteum*, a fibrous membrane which contains the blood vessels and nerves (located in Haversian canals) that provide nourishment and sensation to

the bone. It also plays an important role in osteogenesis, as it is colonized by bone cells.⁵³ Also the internal bone surface is lined by a thin layer of osteogenic and other cells (*endosteum*).

Progenitor cells or pre-osteoblasts, osteoblasts, osteocytes and osteoclasts are the major types of bone cells.

Osteoblasts are bone-forming cells. They originate from local pluripotent mesenchymal stem cells, either bone marrow stromal cells residing in the *endosteum* or connective tissue mesenchymal stromal cells from the *periosteum*. These cells are very active in synthesizing and secreting the components of the bone matrix and have well-developed rough endoplasmic reticulum, Golgi bodies and granules. Osteoblasts are rich in the enzyme alkaline phosphatase, which plays a major role in the formation of the mineral deposits in the matrix. The collagen fibers are synthesized and secreted by the osteoblasts.

Lining the bone surface, they are gradually trapped in the bone matrix which they produce and that calcifies. As a result those cells dramatically decrease their metabolic activity, now becoming fully differentiated mature bone cells (osteocytes) enclosed in small *lacunae*. Thus, osteocytes, the most abundant cell type in bone tissue, are mature bone cells that develop from osteoblasts and are located in *lacunae* within the bone matrix. Osteocytes have cytoplasmic processes located in *canaliculi*, which penetrate the bone matrix. In contrast to osteoblasts and osteocytes, osteoclasts are giant multinucleated bone resorbing cells, which differentiate from hematopoietic progenitors of the monocyte/macrophage lineage. Like osteoblasts, they are situated on the bone surface⁵⁴ and can be found on the eroding surfaces of bone.

The correct interplay between those cell types is essential in bone homeostasis, remodeling and repair. Skeletal elements are initially formed as soft tissue templates that thereafter undergo gradual ossification and growth leading to an increase in size with relatively little changes in shape. This phase of bone formation lasts from the early stages of fetal life until adulthood.

Two distinct mechanisms are responsible for bone formation: intramembranous, and endochondral ossification. Both types of ossification involve initial condensation of mesenchyme followed by the

18 - Chapter 1

formation of calcified bone. Whereas intramembranous bone formation accomplishes this directly giving rise to flat bones (e.g. skull bones, *scapula*, mandible and *ilium*), endochondral ossification involves an intermediate step in which a cartilaginous template regulates the growth and patterning of the developing skeletal element, creating long bones (e.g. *tibia*, femur, humerus and *vertebrae*). The cartilaginous center subsequently becomes hypertrophic and a center of ossification forms by vascular invasion. The secretion and mineralization of ECM is mediated by osteoblasts. As bone grows, this center of ossification expands and the inside of the shaft region is resorbed.^{55,56}

The skeleton is a metabolically active organ undergoing continuous remodeling process. These processes control the reshaping or replacement of bone following injuries like fractures but also micro-damage, which occur during normal activity. Remodeling responds also to functional demands of the mechanical loading.

The process of bone remodeling is a turnover mechanism, which allows old bone replacement as well as changes in shape, architecture or density of the skeleton. It involves three consecutive phases: resorption, during which osteoclasts digest old mineralized bone; reversal, when mononuclear cells appear on the bone surface, and formation, when osteoblasts lay down new bone until the resorbed bone is completely replaced.⁵⁷ Bone healing is initiated by hematoma formation and inflammation at the fracture site.

The inflammatory phase is a critical period characterized by low oxygen tension, impaired perfusion, and the migration of a wide array of growth factors. As a second step, bone is very rapidly formed through endochondral or intramembranous ossification. However, it is progressively replaced by mature bone, during the following remodeling process.⁵⁸

1.5 Bone tissue engineering: from conventional approaches to magnetic scaffolds

The guiding process of bone regeneration is gaining importance as an alternative treatment of bone defects, as a novel strategy that recourses neither to synthetic prostheses nor to bone grafts. It aims to restoring the function of large bone defects and overcomes the limitations of prostheses and bone grafts.

Synthetic prostheses partially restore large defects for a relatively short useful life. On the other hand, autologous bone graft is not always available in sufficient amounts. Bone allografts are expensive and have known risks of bacterial contamination, viral transmission and immunogenicity if compared to autologous bone grafts.

Ideal bone scaffold should possess all the properties described above, but the biomechanical environment introduces another level of complexity. In fact, the scaffold needs to be able to withstand external forces, and it is known that bone regeneration, modeling and remodeling is mediated by mechanical stimuli known as mechanotransduction.^d Mechanical stimuli transferred by scaffolds to cells rely exclusively on intrinsic scaffold properties, such as material stiffness and architecture.

Re-establishing the full functionality in damaged tissues, through tissue engineering approach, requires a relatively long regeneration time. Thus, the temporal control of the various aspects of the tissue growth is very important to allow optimal clinical outcomes. In order to obtain a complete histomorphologically and biologically mature tissue, as bone, the restoration of the mechanical

^d The process by which mechanical energy is converted into electrical and/or biochemical signals.^{21, 59} At the cellular level, a bidirectional integrin mediated process takes place between cells and their surroundings in which they experience different types of forces. A normal tissue cell not only applies a force but responds through the cytoskeleton organization to the resistance that cell senses regardless of a synthetic substrate or an adjacent cell. In trabecular as well as in compact bone, the three-dimensional organization of its structure depends on the direction of the principal mechanical stresses during daily loading and movement.^{21,60-62} The loading information is communicated to effector cells that can make new bone or destroy old bone.²¹ It is currently believed that when bones are loaded, the resulting deformation will drive the thin layer of interstitial fluid surrounding the network of osteocytes to flow from regions under high pressure to regions under low pressure.⁶³⁻⁶⁵ This flow of fluid is sensed by the osteocytes which in turn produce signaling molecules that can regulate bone resorption through the osteoclasts, and bone formation through the osteoblasts, leading to adequate bone remodeling.⁶³⁻⁶⁵ This concept is known as the fluid flow hypothesis.

resistance to physiological stresses should be followed by angiogenesis^e, which is a crucial aspect in the development of regenerative medicine approaches that require rapid vascularization of tissue-engineered structures. Using the traditional scaffolds approaches, where the growth factors are usually seeded before the implantation, a temporal control is hardly achievable.

Pre-loading limits the delivery of localized and temporally controlled growth factors, thus reducing the scaffold tissue regeneration potential.

The possibility of developing innovative scaffolds, able to modify intrinsic properties on demand, affords new opportunities to control the bone regeneration process.

In the last years, research attention has been focused on the design and development of new conceptually type of bioactive scaffold able to be manipulated *in situ* by means of magnetic forces⁶⁷ in order to repair large bone defects and osteochondral lesions of the skeletal system.

In designing magnetic substrates/scaffolds, the rationale should be summarized in the possibility to obtain structures that can be manipulated *in situ* by applying external magnetic fields, also able to control specific processes at cell level by releasing biomolecules and bioactive factors, in turn linked to magnetic nanocarriers.^{67,72}

The previously described concept of magnetic guidance basically spans from biomedicine to tissue engineering, involving drug delivery, hyperthermia treatment of tumors, magneto-mechanical stimulation/activation of cell-constructs and mechanosensitive ion channels, magnetic cell-seeding procedures, controlled cell proliferation and differentiation.^{67,68-89}

In the field of biomedicine, magnetic nanoparticles (MNPs) possess peculiar physical properties and provide some attractive possibilities because of their dimensions, ranging from a few nanometers up to tens of nanometers, which make them comparable to several biological entities. They show sizes

^e The physiological process through which new blood vessels are developed starting from pre-existing vessels. It is critical to tissue functionality for the delivery of nutrients and oxygen and depends on the tightly coordinated interplay between a specific peptide sequence known as Vascular Endothelial Growth Factor (VEGF) and other signaling molecules. VEGF induces endothelial cells which are the ones lining the lumen of blood vessels to proliferate, migrate and sprout neovessel. Simultaneous interactions between different molecules such as angiopoietin-2 and basic Fibroblast Growth Factor (BFGF) contribute to the induction of this process whereas sequential collaboration with Platelet Derived Growth Factor (PDFG) and angiopoietin-1 mediate recruitment of mural cells and stabilization of endothelium.^{21,66}

that are close to or smaller than those of a protein (5-50 nm), a virus (20-450 nm), a cell (10-100 μm), or a gene (10-100 nm). Basically, their magnetic features allow for manipulating them by properly applying an external magnetic field gradient. This suggests that it would be possible to immobilize and/or to transport the MNPs themselves and magnetically-tagged biological units. Drugs or a group of radionuclide atoms could be suitably delivered to a targeted region of the body (i.e., a tumor). MNPs can resonantly respond to a time-varying magnetic field and several advantages can be obtained by the energy transfer from the exciting field to the MNPs.^{68,73}

As an example, MNPs may be heated up allowing their use as hyperthermia agents able to deliver thermal energy to targeted bodies (i.e., tumors) or as elements capable of improving chemotherapy or radiotherapy by providing a degree of tissue warming appropriate for the destruction of malign cells.^{68,73}

Markaki A.E. and Clyne W.T.(2004 and 2005) studied the magneto-mechanical stimulation and actuation of a bonded array of ferromagnetic fibers (i.e., nickel-free ferritic stainless steel) in a non magnetic matrix located in inter-fiber space, evidencing the possibility to generate a change shape of the magnetized fiber array, straining the matrix and inducing a possible mechanism for bone growth stimulation by magnetic field application.^{68,76,77} Mannix R.S. et al. (2008) focused their attention on the nanomagnetic actuation of receptor-mediated signal transduction, describing a magnetic nanotechnology which activates a biochemical signaling mechanism normally switched-on by binding of multivalent chemical ligands.^{68,78} However, an interesting approach related to a selective activation of mechanosensitive ion channels using magnetic particles has been also reported by Hughes S. et al. (2008). This technique should permit the direct manipulation of ion channels in real time without the needs for pharmacological drugs, and should be potentially considered as a tool for the treatment of human diseases ascribed to ion-channel dysfunction.^{68,79}

Interestingly, Kanczler J.M. et al. (2010) studied the controlled differentiation of human bone marrow stromal cells using remote magnetic field activation and MNPs.^{68,80} In the field of tissue engineering, novel methodologies, defined as “magnetic force-based tissue engineering”, and

techniques for designing tissue-engineered tubular and sheet-like constructs using MNPs and magnetic force were proposed and studied by Ito A. et al. (2005).^{68,81,82} It has also been reported that magnetic forces enable rapid endothelialization of a knitted Dacron graft externally covered by a magnetic sheet, benefiting from biophysical forces able to attach blood-derived endothelial outgrowth cells (EOCs) to the surface of prosthetic vascular grafts, since EOCs endocytose magnetic particles and result attracted to the magnetized graft surfaces.^{68,83}

The basic principles in designing a novel magnetic force mechanical conditioning bioreactor for tissue engineering was proposed by Dobson J. et al. (2006).^{68,84,85} Furthermore, by binding MNPs to the surface of cells, the possibility to manipulate and control cell function through the application of an external magnetic field has been studied, providing information on cellular mechanics and ion channel activation.^{68,86} This technique has been proposed as an investigative potential tool for actively controlling cellular function and processes with a special focus toward tissue engineering and regenerative medicine.^{68,86}

Magnetically actuable tubular scaffolds for smooth muscle tissue engineering were firstly fabricated from sheets of electrospun fibrils of biocompatible and biodegradable polymers containing uniform dispersions of Fe₂O₃ NPs and then wound into tubes for cell seeding from the inner layer to the outer one.^{68,87} As a consequence of the magnetic field application, the induced deformation produces strains in the tube walls and fluid pumping through the walls, which should promote cell proliferation and differentiation. The design of these tubular scaffolds was optimized through a model used to predict the deformation and fluid flow for specific magnetic field strength, material properties and geometrical parameters.^{68,87} Furthermore, involving direct magnetic cell-seeding procedures and MNPs, novel strategies for vascular tissue engineering were proposed by Perea H. et al. (2006)^{68,88} and Shimizu K. et al. (2007).^{68,89}

Firstly, the idea to develop magnetic scaffolds for additionally controlling angiogenesis *in vivo* has been considered by Bock N. et al. (2010).⁶⁷ In that work, magnetic scaffolds were manufactured

through dip-coating of the scaffolds in aqueous ferrofluids that contained iron oxide nanoparticles coated with different polymers for biomedical applications.⁶⁷

From a magnetic point of view, nanoparticles below 30 nm in size of these materials present superparamagnetic behavior (see Appendix), stressing their ability to be magnetized by applying a magnetic field without remanence once the field is turned off.^{67, 68,73, 90}

Taking into consideration a superparamagnetic material, the resulting magnetic scaffold may be able to reach appropriate magnetization values (i.e., up to 15 emu/g at 10 kOe) for ferrofluid or MNPs adhesion when applying an external magnetic field as reported by Bock N. et al. (2010), but it may also be magnetically “turned off” by removing the applied magnetic field.^{67,68}

The scaffold works like a magnetic focusing lens or local field amplifier: its relatively strong internal magnetization can be aligned in the same direction by relatively weak external field. Forces in the order of piconewtons (0.1-1 pN) can be easily achieved by reasonable gradients (0.1-1 T/cm), and such forces can efficiently move nanoparticles (1-10 femtograms) and bioaggregates against the physiologic fluid viscosity.

The magnetic scaffold modifies the magnetic flux distribution and leads to much higher concentration of magnetic “lines” near/inside the scaffold. This point results crucial as these magnetization values can generate magnetic gradients, and via magnetic driving scaffolds may attract and take up cells or other bioagents bound to MNPs and *in vivo* growth factors. In particular, MNPs act as shuttles that can transport these bioagents towards the static scaffold (Figure 5). The magnetic moment of this new type of scaffold allows to control bone regeneration reloading continuously from an external supervising center with tissue growth factors. Thus, a magnetic scaffold can be imagined as a fixed “station” that offers a long-living assistance to implanted tissue engineering constructs, providing a unique possibility to “adjust” the scaffold activity to the personal needs of the patient, when and where tissue regeneration process requires.⁶⁷

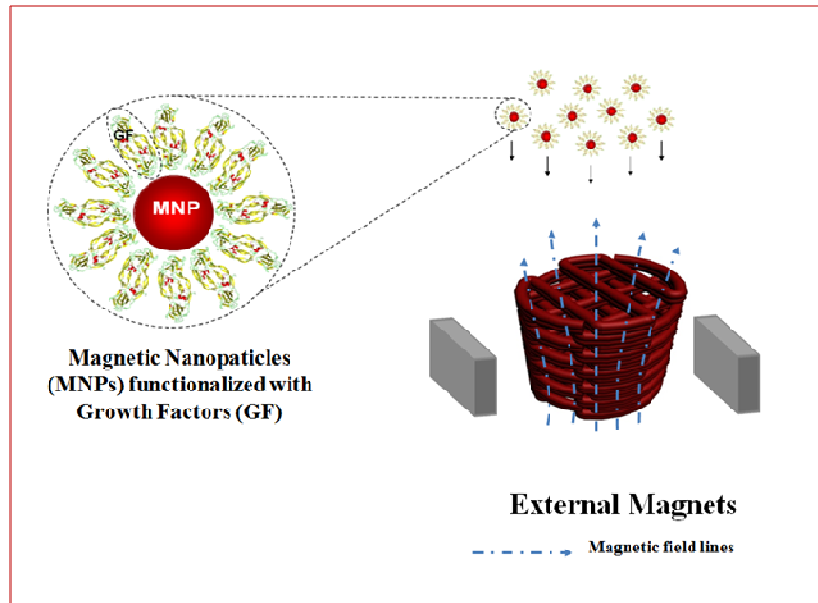


Figure 5: A magnetic scaffold, manipulated *in situ* by applying external magnetic fields, is able to release biomolecules and bioactive growth factors, in turn linked to magnetic nanocarriers.

In addition to the reloading function, magnetic scaffolds will be able to play a number of very important roles.

Magnetic scaffolds and MNPs will be used as delivery systems triggered by a temperature switch due to the possibility to control their temperature through the use of an external variable magnetic field. This approach can be also used to investigate the effect of a prolonged localized temperature increase on angiogenesis during the repair process. From this point of view, it is known that the application of magnetic fields stimulates angiogenesis and osteogenic precursor proliferation, and can also promote bone formation within suitable matrices.⁹¹

Magnetic scaffolds will be used to achieve efficient scaffold fixation via magnetic forces providing a very elegant and simple solution to the clinical problems of fixation that many scaffolds meet.

Today, in the treatment of small osteochondral lesions, most surgeons do not use any fixation system while in the treatment of large bone defects, fixation is achieved by means of external systems, intramedullary nails, plates and screws, complicate procedures that require continuous control and often multiple surgical interventions. By this point of view, Russo A. et al. (2012) have

proposed an innovative magnetic fixation approach based on the application of a magnetic scaffold (with a saturation value of 17 emu/g).⁹²

In that work, different configurations have been proposed and a finite element modeling (FEM) was exploited to investigate the fixation efficiency (Figure 6)

It was found that for most appropriate magnetic materials and optimized magnet-scaffold positioning, all the considered configurations provide a sufficient scaffold fixation.⁹²

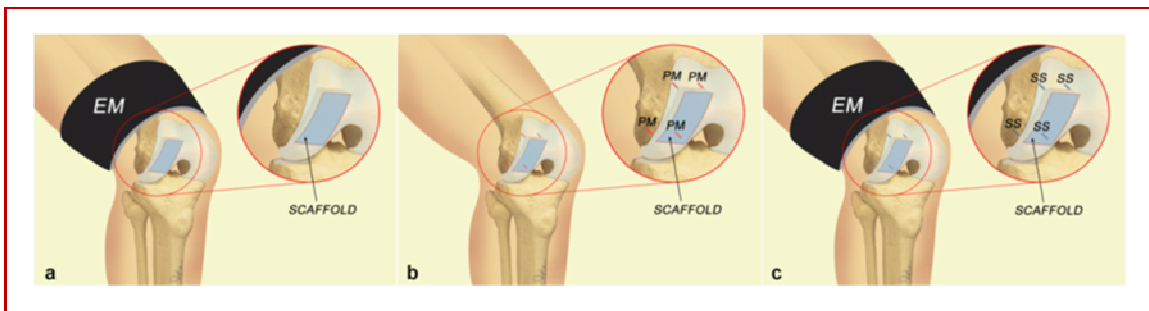


Figure 6: Schematic representation of magnet-scaffold configurations: (a) external permanent magnet ring (EM); (b) implanted permanent magnet pins (PM); (c) implanted stainless steel pins in the field of external magnet (EM + SS).⁹²

1.6 Scaffold preparation techniques

In order to obtain 3D porous scaffolds, several different techniques, with their own advantages and limitations, have been developed.

Usually, scaffold fabrication techniques have been classified into two groups, defined as “conventional” and “novel” methods.^{2,17,93}

Basically, conventional methods, such as fiber bonding, gas foaming, solvent casting/particulate leaching, phase separation, freeze drying, solution casting, are unable to precisely control the internal architecture of scaffolds, including pore size, pore geometry, spatial distribution of pores and interconnectivity, which are critical features for their *in vivo*, biological and mechanical performances.

Conversely, the introduction of solid freeform fabrication (SFF) techniques, named also “rapid prototyping” (RP) techniques, into biomedical field has allowed to produce customized scaffolds with reproducible internal morphology.

SFF was initially developed in 1987 for fabricating prototype engineering parts and manufacture objects in a layer-by-layer fashion from the 3D computer design of the object.^{2,17,93,94}

All SFF technologies are characterized by three basic steps in their process: data input, data file preparation, and object building.^{2,17,94} In particular, the general process is based on a computer-generated model obtained through the use of a computer-aided design (CAD) software. Successively, a CAD model is expressed as a series of cross-sectional layers, and the data are implemented by the SFF machine that creates the physical model.

Accordingly, customized scaffolds for tissue engineering may be designed and manufactured by integrating different techniques such as image capture (i.e. computed tomography or magnetic resonance imaging), 3D modeling and rapid prototyping with those related to the preparation of polymer and nano/microcomposite materials for scaffolds processing.

Among all the SFF techniques, 3D printing, Fused Deposition Modeling (FDM), ink-jet printing, stereolithography, Selective Laser Sintering (SLS), 3D Bioplotting and 3D fiber deposition have gained great importance.

3D printing is a technology based on a binder ejection from a jet head that moves in accordance with the CAD data onto a polymer powder surface. The binder dissolves to join powder particles. The process is then repeated until the structure is obtained.¹⁷

FDM is an additive manufacturing technology. It uses a moving extrusion system which follows a tool-path defined by the CAD file in order to build layer-by-layer a physical model starting from a polymeric fiber. The nozzle is heated to melt the material and can be moved in both horizontal and vertical directions by a numerically controlled mechanism, using a computer-aided manufacturing (CAM) software package.¹⁷

Ink-jet printing is based on a system that consists in a build platform, set on top of an elevator with a rolling cutter blade on one side of the platform and two print jets mounted on x, y rails. In order to build a 3D structure, two print materials are used, build materials and support materials. The build jet first lays down the design pattern by printing droplets onto the platform. The support jet then prints support material around the printed pattern. After printing, the cutter blade comes over and cuts the build layer to a predetermined layer thickness, thereby controlling the accuracy in the z-direction. The build jet then prints build material for the next layer. The process repeats itself until the entire object is completed.¹⁷

Stereolithography allows to build accurate parts directly from 3D CAD data without tooling by converting liquid materials and composites into solid cross-sections, layer-by-layer, using an ultraviolet laser (UV). The UV beam is guided onto the liquid monomer surface placed on an elevator. After the first layer is built, the elevator is lowered. Then, a resin-filled blade sweeps across the cross-section of the part, re-coating it with fresh material. The process is repeated until a 3D part is built; finally, it is immersed in a chemical bath in order to be cleaned of excess resin and is subsequently cured in an ultraviolet oven.¹⁷

In SLS, the material is not melted; powder grains of polymeric or polymer coated ceramic material are fused together by heating the materials shortly just above the glass transition temperature, so that only outer layer of the powder grains melts and fuses to the adjacent grain. This technique uses a high power laser (i.e. CO₂) to fuse the small particles into a mass that has a desired three-dimensional shape. The laser selectively fuses powdered material by scanning cross-sections generated from a 3D digital description of the part (i.e. CAD data) on the surface of a powder bed. After each cross-section is scanned, the powder bed is lowered by one layer thickness, a new layer of material is applied on top, and the process is repeated until the part is completed.¹⁷

3D Bioplotting is an additive technology very similar to FDM. The Bioplotter system, developed by researchers at the University of Freiburg, involves a moving extruder head (x-, y- and z-axis control) and uses compressed air to force out a liquid or a paste-like plotting medium into the form

of filaments, which solidify onto the platform. The extruder head can be heated to the required temperature. The medium solidifies when it comes in contact with the substrate or previous layer.¹⁷

1.6.1 3D fiber deposition technique

Among all of the rapid prototyping techniques, 3D plotting⁹⁵⁻⁹⁷ and 3D fiber deposition⁹⁸ have been recently developed and used for tissue-engineering purposes.

In particular, 3D fiber deposition may be considered as a modified technique of 3D plotting for the extrusion of highly viscous polymers, and it is a fused deposition technique in which a molten polymer is extruded and then deposited through a servo-mechanically controlled syringe that applies pressure (Figure 7).⁹⁹⁻¹⁰¹ This process allows to obtain scaffolds, with a customized shape and size by CAD/CAM techniques and 100% interconnectivity.

The key-element of the 3D fiber deposition technique is a dispensing machine known as Bioplotter, which was developed by Landers et al.⁹⁵⁻⁹⁷ to produce scaffolds from hydrogel for soft tissue engineering.

It consists of a dispenser, equipped with a heating jacket that is movable in three dimensions. The basic process involves dispensing of a flowable material stored into a cartridge through a thin needle by air-pressure control, and its subsequent hardening (Figure 7).

The material can be dispensed in a liquid that has the advantage of preventing deformation⁹⁵ or in presence of air if highly viscous materials, such as polymer melts, are processed. Hardening processes can be obtained through thermally induced solidification, solidification induced by a chemical reaction, and solidification induced by precipitation.

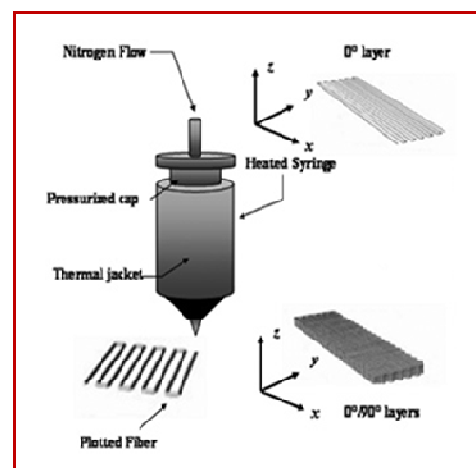


Figure 7: Plotting process.

The knowledge of the critical processing parameters results crucial to develop 3D fiber deposited scaffolds. The building process for 3D plotting is dependent on a large number of parameters such as: needle (i.e. type, length and diameter), dispensing pressure gradient, deposition speed or feeding rate, layer thickness, fiber spacing or strand distance, sequence of stacking or lay-down pattern.

The needle length is significant for the dispensing process as it is closely connected with the viscosity of the plotter material. Low-viscosity materials are usually processed with long, thin dispensing needles, while on the other hand, short (often conical) dispensing needle types are used for highly viscous materials.

If a molten polymer is assumed as a viscous Newtonian fluid and the Hagen-Poiseuille equation as valid,^{98, 102} the flow rate from the nozzle can be expressed according to:

$$Q = \frac{\pi \Delta P d^4}{128 \eta l} \quad (1)$$

The above Hagen-Poiseuille equation (1) indicates that the flow rate (Q) is directly proportional to both the pressure gradient (ΔP) across the syringe and needle tip, and the needle diameter (d). Moreover, the flow rate (Q) is inversely proportional to needle length (l) and polymer viscosity (η). A high Q value may result in over-deposition of the fiber, thus reducing porosity, whilst a low Q value reduces the fiber diameter, compromising the overall scaffold integrity. A decrease in needle diameter reduces the flow rate, requiring considerably greater pressures to extrude fibers, and in the case of small needle diameters the pressures required to achieve a suitable flow rate can be greater than those usually used in practice, thus needing changes in viscosity.⁹⁸ Even though for small needle diameters polymer viscosity can be reduced through the addition of specific solvents or increasing the syringe temperature, the incomplete removal of solvents post-processing or polymer exposure to high temperatures can be detrimental to scaffold biocompatibility.

Moroni L. et al.⁹⁹⁻¹⁰¹ designed, manufactured and characterized 3D fiber deposited PEOT/PBT scaffolds. Poly(ethylene oxide terephthalate)–poly(butylene terephthalate) (PEOT/PBT) block copolymers belong to a class of materials known as thermoplastic elastomers, and possess

mechanical properties depending on their weight ratio in block form and on the molecular weight of the initial poly(ethylene glycol) (PEG) blocks.⁹⁹⁻¹⁰¹

Several PEOT/PBT copolymer compositions were used to fabricate scaffolds with a Bioplotter device through heating polymer pellets. Moreover, pores were varied in shape and size, by changing fiber diameter, spacing, sequence of stacking, and layer thickness.^{17,99-101} However, since pore geometry (and, hence, porosity) is defined by fiber diameter and spacing, and layer thickness, it is also strongly dependent on the deposition speed or feeding rate used during the process (Figure 8).⁹⁹

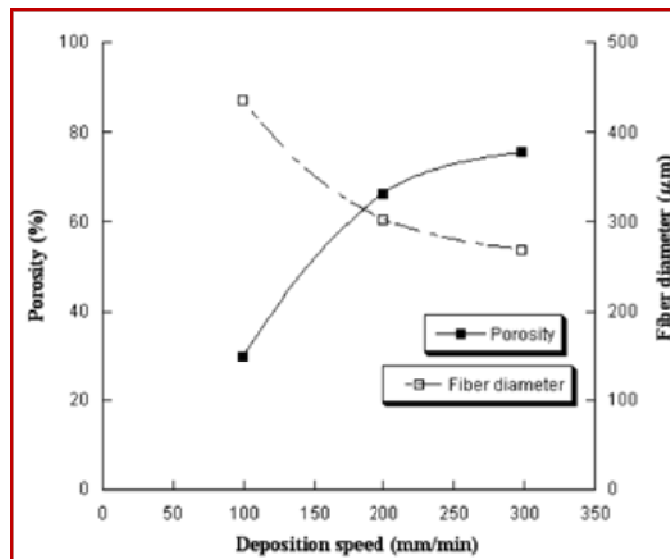


Figure 8: Effect of deposition speed on scaffold porosity and fiber diameter.⁹⁹

The feeding rate is dependent on the material flow through the nozzle and the rate at which the material hardens. The faster a material hardens, the faster the feeding rate has to be, ensuring that the adhesiveness of the plotter material is still adequate to bond the layers when it reaches the layer below. On the other hand, if the material hardens very slowly it needs to choose a relatively slow feeding rate, to give the previously dispensed plotter material time to harden before the new layer is dispensed on to it. The material flow through the nozzle and the feeding rate must be coordinated with each other.

Accordingly, in order to assess the influence of the pores geometry and architecture on the mechanical performances, 3D fiber deposited PEOT/PBT scaffolds were characterized through dynamic-mechanical analysis (DMA). In particular, with increasing porosity, DMA analysis showed a decrease of the elastic properties such as the storage modulus (E') (Figure 9a),^{100,101} whilst an increase of the modulus was evaluated with decreasing the fiber spacing (Figure 9b).^{100,101} Furthermore, it is worth noting that for PEOT/PBT scaffolds with the same composition and porosity but different architectures, E' varied within a wide range of values (Figure 9c).

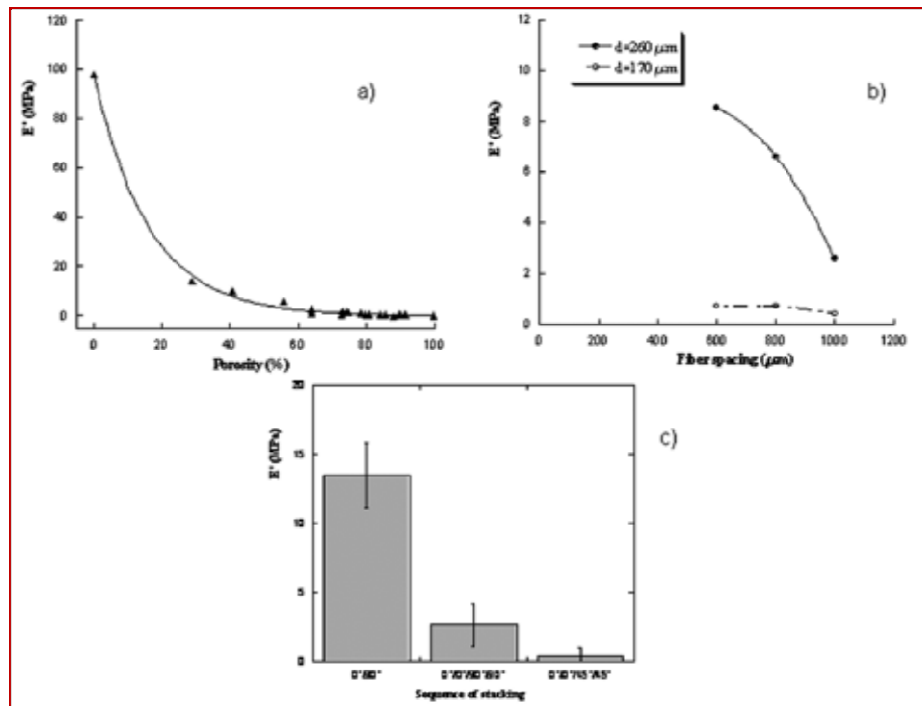


Figure 9: a) Effect of porosity on the storage modulus E' for 3D fiber deposited PEOT/PBT scaffolds with specific composition,¹⁰⁰ b) Effect of fiber spacing on the storage modulus E' for 3D fiber deposited PEOT/PBT scaffolds with specific composition and architecture, considering two different fiber diameters,¹⁰⁰ c) Effect of architecture on the storage modulus E' for 3D fiber deposited PEOT/PBT scaffolds with same composition and porosity.¹⁰⁰

Another interesting approach was to make hollow fibers directly integrated in a 3D fiber deposited structure, thus obtaining scaffolds which can be used in tissue engineering and controlled drug delivery applications as possible smart biomaterial devices.¹⁰³ To obtain hollow fibers, with controllable hollow cavity diameter and shell thickness, a rheological phenomenon, which is known

as “viscous encapsulation” and often undesired in molten polymeric blends, has to be considered.¹⁰³

Briefly, when two components of a polymer blend possess a significant difference in viscosity in the molten state, fibers with a shell-core configuration can be extruded.

The polymer with lower viscosity tends to shift, when flowing through a narrow duct, such as the nozzle of an extruder (e.g. the needle used during the 3D Bioplotting process), towards the walls of the nozzle during extrusion.

Due to the higher shear stresses at the walls this separation of the components produces stratification or “canalization” effect, thus providing fibers with a shell-core structure (Figure 10).

By removing the core polymer by selective dissolution, hollow fibers can be obtained.¹⁰³

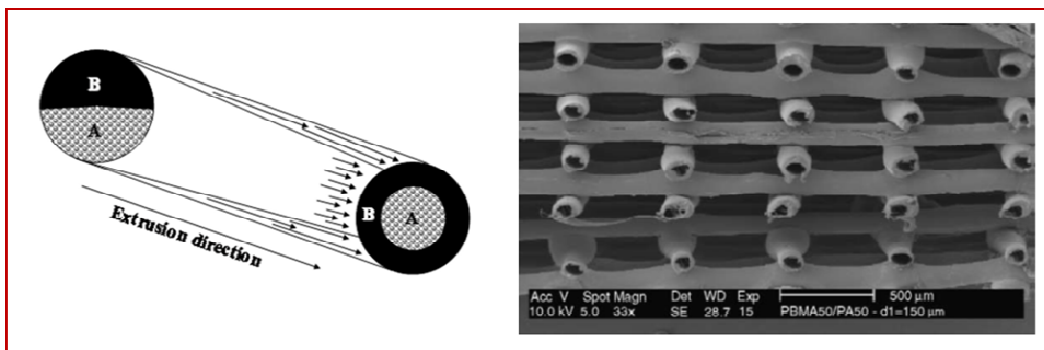


Figure 10: (left) Viscous encapsulation phenomenon: arrows indicate the encapsulation of the high viscosity polymer (A) by the low viscosity polymer (B), due to higher shear stress (longer arrows) at the nozzle walls,¹⁰³ (right) 3D fiber deposited structure with shell-core fibers.¹⁰³

The use of these biphasic shell-core 3D fiber deposited scaffolds with appropriate mechanical and surface properties has been demonstrated to be a promising solution for cartilage tissue engineering.

Finally, since cell-seeding efficiency still remains a critical factor for optimal tissue regeneration, the possibility to combine the 3D fiber deposition technique with electrospinning was also demonstrated (Figure 11);^{17,104} therefore, obtaining scaffolds where the periodical macrofibers typical of 3D fiber deposited structures were integrated with the random electrospun ones. In these integrated structures, the 3D fiber deposited scaffold acts as a structural support with adequate

mechanical properties, whilst the electrospun network mainly works as a cell entrapment system.^{17,104,105}

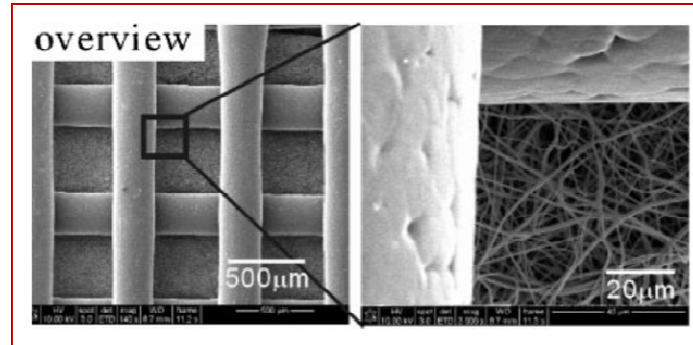


Figure 11: SEM images of hybrid poly(ϵ -caprolactone) (PCL) scaffolds obtained combining 3D fiber deposition and electrospinning technologies.¹⁰⁵

In conclusion, the mechanical behavior of the 3D fiber deposited scaffolds is dependent not only on the intrinsic properties of the material processed, but also on the different 3D architectural and geometric features, thus highlighting the possibility to tailor their mechanical properties suitably.

Consequently, if mimicking the biomechanical behavior of the tissue to be grown is a key point in tissue engineering, the 3D fiber deposition technique may be considered as a powerful tool to create scaffolds for specific applications.¹⁷

References

1. Lavik E., Langer R. *Tissue engineering: current state and perspectives*. Appl. Microbiol. Biotechnol. 65: 1–8, 2004.
2. Sachlos E., Czernuske J.T. *Making tissue engineering scaffold work: review on the application of SFF technology to the production of tissue engineering scaffolds*. Eur. Cell Mat. 5: 29-40, 2003.
3. Langer R., Vacanti J. *Tissue Engineering*. Science. 260: 920-926, 1993.
4. Barth A. *Ueber histologische befunde nach knochenimplantationen*. Arch. Klein. Chir. 46: 409-17, 1893.
5. Meng D., Boccaccini A.R. *Nanostructured biocomposites for tissue engineering scaffolds*. In: Ambrosio L, ed. Biomedical composites. Cambridge, UK: Woodhead Publishing Limited, CRC Press. 509-546, 2010.
6. Atala A., Lanza R.P. *Methods of tissue engineering*. Academic Press, San Diego, 2001.
7. Ohgushi H., Caplan A.I. *Stem cell technology and bioceramics: From cell to gene engineering*. J. Biomed. Mater. Res. 48:913–27, 1999.
8. Gloria A., De Santis R., Ambrosio L. *Polymer-based composite scaffolds for tissue engineering*. J. Appl. Biomater. Biomech. 8 (2): 57-67, 2010.
9. Causa F., Netti P.A., Ambrosio L. *A multi-functional scaffold for tissue regeneration: the need to engineer a tissue analogue*. Biomaterials. 28: 5093-9, 2007.
10. Guarino V., Causa F., Ambrosio L. *Bioactive scaffolds for bone and ligament tissue*. Expert. Rev. Med. Devices. 4 (3): 405-418, 2007.
11. Chaikof E.L., Matthew H., Kohn J., Mikos A.G., Prestwich G.D., Yip C.M. *Biomaterials and scaffolds in reparative medicine*. Ann. N. Y. Acad. Sci. 961: 96-105, 2002.
12. Hutmacher D.W., Schantz J.T., Lam C.X.F., Tan K.C., Lim T.C. *State of the art and future directions of scaffold-based bone engineering from a biomaterials perspective*. J. Tissue Eng. Regen. Med. 1: 245-260, 2007.
13. Mathieu L.M., Mueller T.L., Bourban P.E., et al. *Architecture and properties of anisotropic polymer composite scaffolds for bone tissue engineering*. Biomaterials. 27: 905-16, 2006.
14. Devin J.E., Attawia M.A., Laurencin C.T. *Three-dimensional degradable porous polymer-ceramic matrices for use in bone repair*. J. Biomater. Sci. Polymer Ed. 7: 661-9, 1996.
15. Nicolais L., Gloria A., Ambrosio L. *The mechanics of biocomposites*. In: Ambrosio L, ed. Biomedical composites. Cambridge, UK: Woodhead Publishing Limited, CRC Press. 411-40, 2010.
16. Ramakrishna S., Mayer J., Wintermantel E., Leong K.W. *Biomedical applications of polymer-composite materials: a review*. Comp. Sci. Tech. 61: 1189-1224, 2001.

17. Gloria A., Russo T., De Santis R., Ambrosio L. *3D fiber deposition technique to make multifunctional and tailor-made scaffolds for tissue engineering applications*. J. Appl. Biomater. Biomech. 7: 141-52, 2009.
18. Le Geros R.Z. *Properties of osteoconductive biomaterials: calcium phosphates*. Clin. Orthop. Relat. Res. 395: 81-98, 2002.
19. Rezwani K., Chen Q.Z., Blaker J.J., Boccaccini A.R. *Biodegradable and bioactive porous polymer/inorganic composite scaffolds for bone tissue engineering*. Biomaterials. 27: 3143-3431, 2006.
20. Zhang K., Wang Y., Hillmeyer M.A. Francis L.F. *Processing and properties of porous poly(L-lactide)/bioactive glass composites*. Biomaterials. 25: 2489-2500, 2004.
21. Plannel J.A., Navarro M. *Developing targeted biocomposites in tissue engineering and regenerative medicine*. In: Ambrosio L, ed. Biomedical composites. Cambridge, UK: Woodhead Publishing Limited, CRC Press. 573-592, 2010.
22. Mc Farland C.D., Mayer S., Scotchford C., Dalton B.A., Stelle J.C., Downes S. *Attachment of cultured human bone cells to novel polymers*. J. Biomed. Mater. Res. 1: 1-11, 1999.
23. Siebers M.C., Ter Brugge P.J., Walboomers X.F., Jensen J.A. *Integrins as linker proteins between osteoblasts and bone replacing materials. A critical review*. Biomaterials. 21: 2453-2460, 2005.
24. Anselme K. *Osteoblast adhesion on biomaterials*. Biomaterials. 21: 667-681, 2000.
25. Tampieri A., Sprio S., Landi E., Sandri M. *Developing biocomposites as scaffolds in regenerative medicine*. In: Ambrosio L, ed. Biomedical composites. Cambridge, UK: Woodhead Publishing Limited, CRC Press. 547-572, 2010.
26. Karageorgiou V., Kaplan D. *Porosity of 3D biomaterial scaffolds and osteogenesis*. Biomaterials. 26: 5474-5491, 2005.
27. Boccaccini A.R., Maquet V. *Bioresorbable and bioactive polymer/Bioglass® composites with tailored pore structure for tissue engineering applications*. Compos. Sci. Technol. 63: 2417-2429, 2003.
28. Engel E. et al. *Nanotechnology in regenerative medicine: the materials side*. Trend Biotechnol. 26 (1): 39-47, 2003.
29. Gloria A., Causa F., Russo T., Battista E., Della Moglie R., Zeppetelli S., De Santis R., Netti P.A., Ambrosio L. *Three-Dimensional Poly(ε-caprolactone) Bioactive Scaffolds with Controlled Structural and Surface Properties*. Biomacromolecules. 13: 3510–3521, 2012.
30. Causa F., Battista E., Della Moglie R., Guarnieri D., Iannone M., Netti P.A. *Surface investigation on biomimetic materials to control cell adhesion: the case of RGD conjugation on PCL*. Langmuir. 26: 9875–9884, 2010.
31. Garcia A.J., Reyes C.D. *Bio-adhesive surfaces to promote osteoblast differentiation and bone formation*. J. Dent. Res. 84: 407–413, 2005.

36 - Chapter 1

32. El-Amin S.F., Kofron M.D., Attawia M.A., Lu H.H., Tuan R.S., Laurencin C.T. *Molecular regulation of osteoblasts for tissue engineered bone repair*. Clin. Orthop. Rel. Res. 427: 220–225, 2004.
33. Hersel U., Dahmen C., Kessler H. *RGD modified polymers: biomaterials for stimulated cell adhesion and beyond*. Biomaterials. 24: 4385–4415, 2003.
34. Li S.M., Mc Carthy S. *Further investigations on the hydrolytic degradation of poly(DL-lactide)*. Biomaterials. 20: 35.44, 1999.
35. Navarro M., Ginebra M.P., Planel J.A., Zeppetelli S., Ambrosio L. *Development and cell response of a new biodegradable composite scaffold for bone guided regeneration*. J. Mater. Sci. Mater. Med. 15: 419-422, 2004.
36. Baron R. *Anatomy and ultrastructure of bone - histogenesis, growth and remodeling. Diseases of bone and mineral metabolism*. Frederick Singer, MD; 2008.
37. Rho J.Y., Kuhn-Spearing L., Zioupos P. *Mechanical properties and the hierarchical structure of bone*. Med. Eng. Phys. 20: 92–102, 1998.
38. Purbrick M., Ambrosio L., Ventre M., Netti P. *Natural composites: structure-property relationships in bone, cartilage, ligament and tendons*. In: Ambrosio L, ed. Biomedical composites. Cambridge, UK: Woodhead Publishing Limited, CRC Press. 3-24, 2010.
39. Fyhrie D.P., Kimura J.H. *Cancellous bone biomechanics*. J. Biomech. 32: 1139, 1999.
40. Lakes R.S. *Materials with structural hierarchy*. Nature. 361: 511-515, 1993.
41. Landi E., Logroscino G., Proietti A., Tampieri A., Sandri M., Sprio S. *Biomimetic Mg-substituted hydroxyapatite: from synthesis to in vivo behavior*. J. Mat. Sci. Mat. Med. 19: 239-247, 2008.
42. Salgado A.J., Coutinho O.P., Reis R.L. *Bone tissue engineering: state of the art and future trends*. Macromol Biosci. 4(8):7 43-65, 2004.
43. Sommerfeldt D.W., Rubin C.T., *Biology of bone and how it orchestrates the form and function of the skeleton*. Eur. Spine J. 10 (2), S86-95, 2001.
44. Rho J.Y., Hobatho M.C., Ashman R.B. *Relations of density and CT numbers to mechanical properties for human cortical and cancellous bone*. Med. Eng. Phys. 17: 347–55, 1995.
45. Goldstein S. *The mechanical properties of trabecular bone: dependence on anatomic location and function*. J. Biomech. 20: 1055–61, 1987.
46. Ascenzi A., Bonucci E. *The Compressive Properties of Single Osteons*. Anat. Record. 161(3): 377-391, 1968.
47. Ascenzi A., Bonucci E. *The Tensile Properties of Single Osteons*. Anat. Record. 158(4): 375-386, 1967.

48. Ascenzi A., Baschieri P., Benvenuti A. *The Bending Properties of Single Osteons*. J. Biomech. 23(8): 763-771, 1990.
49. Ascenzi A., Baschieri P., Benvenuti A. *The Torsional Properties of Single Selected Osteons*. J. Biomech. 27(7): 875-884, 1994
50. Kaplan S.J., Hayes W.C., Stone J.L., Beaupre G.S. *Tensile strength of bovine trabecular bone*. J. Biomech.; 18: 723-727, 1985.
51. Stone J.L., Beaupre G., Hayes W.C. *Multiaxial strength characteristics of trabecular bone*. J. Biomech. 16: 743-752, 1983.
52. Jiroušek O. *Nanoindentation of Human Trabecular Bone – Tissue Mechanical Properties Compared to Standard Engineering Test Methods*. In Nanoindentation in Materials Science, edited by Jiri Nemecek. ISBN 978-953-51-0802-3, 2012.
53. Hutmacher D.W., Sittinger M. *Periosteal cells in bone tissue engineering*. Tissue Eng. 9: S45-S64., 2003.
54. Gallo J., Raska M., Mrazek F., Petrek M. *Bone remodeling, particle disease and individual susceptibility to periprosthetic osteolysis*. Phys. Res.57: 339-49, 2008.
55. Ornitz D.M., Marie P.J. *FGF signaling pathways in endochondral and intramembranous bone development and human genetic disease*. Genes Dev. 16: 1446-65, 2002
56. Salle B.L., Rauch F., Travers R., Bouvier R., Glorieux F.H. *Human fetal bone development: Histomorphometric evaluation of the proximal femoral metaphysis*. Bone. 30: 823-8, 2002.
57. Nakahama K. *Cellular communications in bone homeostasis and repair*. Cell. Mol. Life Sc. 67: 4001-9, 2010.
58. Pape H.C., Marcucio R., Humphrey C., Colnot C., Knobe M., Harvey E.J. *Trauma induced inflammation and fracture healing*. J. Orthop. Trauma. 24: 522-5, 2010.
59. Burger E.H. and Klein-Nulend J. *Mechanotransduction in bone-role of the lacuno canalicular network*. FASEB J. 13: S101-S112, 1999.
60. Petryl M., Hert J., Fiala P. *Spatial organization of the Harvesian bobe in man*. J. Biomech. 29: 161-169, 1996.
61. Fiala P. and Hert J. *Principal types of functional architecture of cancellous bone in man*. Funct. Dev. Morphol. 3: 91-99, 1993.
62. Hert J. *A new attempt at the interpretation of the functional architecture of the cancellous bone*. J. Biomech. 27: 239-242, 1994.
63. Santos A., Bakker A.D., Klein-Nulend J. *The role of osteocytes in bone mechanotransduction*. Osteoporos Int. 20:1027- 1031, 2009.

64. You J., Yellowley C.E., Donahue H.J. et al. *Substrate deformation levels associated with routine physical activity are less stimulatory to bone cells relative to loading induced oscillating fluid flow.* *J. Biomech. Eng.* 122: 387- 393, 2000.
65. Cowin S.C., Weinbaum S., Zeng Y. *A case for bone canaliculi as the anatomical site of strain generated potentials.* *J. Biomech.* 28: 1281-1297, 1995.
66. Hirshi K.K., Scalak T.C., Peirce S.M., Little C.D. *Vascular assembly in natural and engineered tissues.* *Ann. NY Acad. Sci.* 961: 223-242, 2002.
67. Bock N., Riminucci A., Dionigi C., et al. *A novel route in bone tissue engineering: Magnetic biomimetic scaffold.* *Acta Biomater.* 6: 786-96, 2010.
68. Gloria A., Russo T., D'Amora U., Zeppetelli S., D'Alessandro T., Sandri M., Bañobre-Lopez M., Piñeiro-Redondo Y., Uhlarz M., Tampieri A., Rivas J., Herrmannsdörfer T., Dediu V.A., Ambrosio L., De Santis R. *Magnetic poly(ϵ -caprolactone)/iron-doped hydroxyapatite nanocomposite substrates for advanced bone tissue engineering.* *J. R. Soc. Interface.* 80 (10): 1-11, 2013.
69. Tampieri A., Sprio S., Sandri M., Valentini F. *Mimicking natural bio-mineralization processes: a new tool for osteochondral scaffold development.* *Trends Biotechnol.* 29: 526–535, 2011.
70. Patel Z.S., Young S., Tabata Y., Jansen J.A., Wong M.E., Mikos A.G. *Dual delivery of an angiogenic and osteogenic growth factor for bone regeneration enhances in a critical size defect model.* *Bone.* 43: 931–940, 2008.
71. Laschke M.W., Harder Y., Amon M., Martin I., Farhadi J., Ring A., Torio-Padron N., Schramm R., Rucker M., Junker D., et al. *Angiogenesis in tissue engineering: breathing life into constructed tissue substitutes.* *Tissue Eng.* 12: 2093–2104, 2006.
72. Schieker M., Seitz H., Drosse I., Seitz S., Mutschler W. *Biomaterials as scaffold for bone tissue engineering.* *Eur. J. Trauma.* 32: 114–124, 2006.
73. Pankhurst Q.A., Connolly J., Jones S.K., Dobson J. *Applications of magnetic nanoparticles in biomedicine.* *J. Phys. D: Appl. Phys.* 36: R167-R181, 2003.
74. Barry S.E. *Challenges in the development of magnetic particles for therapeutic applications.* *Int. J. Hyperthermia.* 24: 451–66, 2008.
75. Muthana M., Scott S.D., Farrow N., Morrow F., Murdoch C., Grubb S., Brown N., Dobson, J., Lewis C.E. *A novel magnetic approach to enhance the efficacy of cell-based gene therapies.* *Gene Ther.* 15: 902–910, 2008.
76. Markaki A.E., Clyne W.T. *Magneto-mechanical actuation of bonded ferromagnetic fibre arrays.* *Acta Mater.* 53: 877–889, 2005.
77. Markaki A.E., Clyne T.W. *Magneto-mechanical stimulation of bone growth in a bonded array of ferromagnetic fibres.* *Biomaterials.* 25: 4805–4815, 2004.

78. Mannix R.J., Kumar S., Cassiola F., Montoya-Zavala M., Feinstein E., Prentiss M., Ingber, D.E. *Nanomagnetic actuation of receptor-mediated signal transduction*. Nature Nanotech. 3: 36-40, 2008.
79. Hughes S., McBain S., Dobson J., El Haj A.J. *Selective activation of mechanosensitive ion channels using magnetic particles*. J. Royal Soc. Interface. 5: 855-863, 2008.
80. Kanczler J.M., Sura H.S., Magnay J., Attridge K., Green D., Oreffo R. O.C., J Dobson, J.P., El Haj A.J. *Controlled Differentiation of Human Bone Marrow Stromal Cells Using Magnetic Nanoparticle Technology*. Tissue Eng. 16: 3241-3250, 2010.
81. Ito A., Hibino E., Kobayashi C., Terasaki H., Kagami H., Ueda M., Kobayashi T., Honda H. *Construction and delivery of tissue-engineered human retinal pigment epithelial cell sheets, using magnetite nanoparticles and magnetic force*. Tissue Eng. 11: 489-496, 2005.
82. Ito A., Ino K., Hayashida M., Kobayashi T., Matsunuma H., Kagami H., Ueda M., Honda H. *Novel methodology for fabrication of tissue-engineered tubular constructs using magnetite nanoparticles and magnetic force*. Tissue Eng. 11: 1553-1561, 2005.
83. Pislaru S.V., Harbuzariu A., Agarwal G., Witt T., Gulati R., Sandhu N. P., Mueske C., Kalra M., Simari R. D., Sandhu G. S. *Magnetic forces enable rapid endothelialization of synthetic vascular grafts*. Circulation. 114: I314-I318, 2006.
84. Dobson J. *Magnetic nanoparticles for drug delivery*. Drug Dev. Res. 67: 55–60, 2006.
85. Dobson J., Cartmell S.H., Keramane A., El Haj A. J. *Principles and Design of a Novel Magnetic Force Mechanical Conditioning Bioreactor for Tissue Engineering, Stem Cell Conditioning, and Dynamic In Vitro Screening* IEEE Trans. NanoBiosci. 5, 173-177, 2006.
86. Dobson J. *Remote control of cellular behaviour with magnetic nanoparticles*. Nat. Nanotech. 3: 139-143, 2008.
87. Mack J.J., Cox B.N., Sudre O., Corrin A.A., dos Santos S.L., Lucato, Ma C., Andrew J. S. *Achieving Nutrient Pumping and Strain Stimulus by Magnetic Actuation of Tubular Scaffolds*, Smart Mater. Struct. 18: 104025-104040, 2009.
88. Perea H., Aigner J., Hopfner U., Wintermantel E. *Direct magnetic tubular cell seeding: A novel approach for vascular tissue engineering*. Cells Tiss. Org. 183: 156-165, 2006.
89. Shimizu K., Ito A., Arinobe M., Murase Y., Iwata Y., Narita Y., Kagami H., Ueda M. Honda H. *Effective cell-seeding technique using magnetite nanoparticles and magnetic force onto decellularized blood vessels for vascular tissue engineering*. J. Biosci. Bioeng. 103: 472-478, 2007.
90. Tampieri A., D'Alessandro T., Sandri M., Sprio S., Landi E., Bertinetti L., Panseri S., Pepponi G., Goettlicher J., Bañobre-López M., Rivas, J. *Intrinsic magnetism and hyperthermia in bioactive Fe-doped hydroxyapatite*. Acta Biomater. 8: 843-51, 2012.
91. Nakajima T., Ishiguro A., Wakatsuki Y. *Formation of Super Wires of Clusters by Self-Assembly of Transition Metal Cluster Anions with Metal Cations*. Angew. Chem. Int. Ed. 40 (6): 1066-1068, 2001.

92. Russo A., Shelyakova T., Casino D., Lopomo N., Strazzari A., Ortolani A., Visani A., Dediu V., Marcacci M. *A new approach to scaffold fixation by magnetic forces: Application to large osteochondral defects*. Med. Eng. Phys. 34: 1287–1293, 2012.
93. Peltola S.M., Melchels F.P.W., Grijpma D.K., Kellomäki M. *A review of rapid prototyping techniques for tissue engineering purposes*. Ann. Med. 40: 268-80, 2008.
94. Chu T.M.G. *Solid freeform fabrication of tissue engineering scaffolds*. In: Ma PX, Elisseeff J., eds. Scaffolding in Tissue Engineering. Northwest Florida: Taylor and Francis. 139-53, 2006.
95. Landers R., Pfister A., Hubner U., John H., Schmelzeisen R., Mulhaupt R. *Fabrication of soft tissue engineering scaffolds by means of rapid prototyping techniques*. J. Mat. Sci. 37: 3107–3116, 2002.
96. Landers R., Mulhaupt R. *Desktop manufacturing of complex object, prototypes and biomedical scaffolds by means of computer-assisted design combined with computer-guided 3D plotting of polymers and reactive oligomers*. Macromol. Mater. Eng. 282: 17–21, 2000.
97. Landers R., Hubner U., Schmelzeisen R., Mulhaupt R. *Rapid prototyping of scaffold derived from thermoreversible hydrogels and tailored for application in tissue engineering*. Biomaterials. 23: 4437–4447, 2000.
98. Woodfield T.B.F., Malda J., de Wijn J., Peters F., Riesle J., Van Blitterswijk C.A. *Design of porous scaffolds for cartilage tissue engineering using a three-dimensional fiber-deposition technique*. Biomaterials. 25: 4149–4161, 2004.
99. Moroni L., de Wijn J.R., Van Blitterswijk C.A. *3D fiber-deposited scaffolds for tissue engineering: influence of pores geometry and architecture on dynamic mechanical properties*. Biomaterials. 27: 974-85, 2006.
100. Moroni L., Poort G., Van Keulen F., de Wijn J., Van Blitterswijk C.A. *Dynamic mechanical properties of 3D fiber-deposited PEOT/PBT scaffolds: an experimental and numerical analysis*. J. Biomed. Mater. Res. 78A: 605–614, 2006.
101. Moroni L., de Wijn J.R., Van Blitterswijk C.A. *Three-dimensional fiber-deposited PEOT/PBT copolymer scaffolds for tissue engineering: influence of porosity, molecular network mesh size and swelling in aqueous media on dynamic mechanical properties*. J. Biomed. Mater. Res. A. 75: 957–965, 2005.
102. Vozzi G., Previti A., De Rossi D., Ahuwalia A. *Microsyringe-based deposition of two-dimensional polymer scaffolds with a well-defined geometry for application to tissue engineering*. Tissue Eng. 8: 1089-98, 2002.
103. Moroni L., Schotel R., Sohier J., de Wijn J.R., Van Blitterswijk C.A. *Polymer hollow-fiber three-dimensional matrices with controllable cavity and shell thickness*. Biomaterials. 27: 5918-26, 2006.
104. Moroni L., Schotel R., Hamann D., de Wijn J.R., Van Blitterswijk C.A. *3D fiber-deposited electrospun integrated scaffold enhance cartilage tissue formation*. Adv. Funct. Mater. 18: 53-60, 2008.

105. Kim G.H, Son J., Park S., Kim W. *Hybrid Process for Fabricating 3D Hierarchical Scaffolds Combining Rapid Prototyping and Electrospinning*. *Macromol. Rapid Commun.* 29: 1577–1581, 2008.

Chapter 2

A basic approach in the development of poly(ϵ -caprolactone)/iron oxide nanocomposite magnetic scaffolds

Preface

In the last years, great attention has been given to nanotechnology which may enhance the performance of all the materials used for bone tissue engineering. This approach has led to the design of materials with nanostructured surface features or constituent nanomaterials, such as fibers, grains, or particles, which show at least one dimension from 1 to 100 nm, which may reproduce the natural nanostructure of bone tissue. Nanocomposites can mimic the constituents of natural bone better than the individual components. Thus, nanocomposites consisting of a natural or synthetic polymer reinforced with an inorganic phase (i.e., ceramic phase) are increasingly preferred for bone tissue regeneration because they more closely mimic the structure of natural bone. In comparison with conventional composites, nanocomposites better induce cell response because of their similarity with the natural structure. Moreover, the mechanical performances of nanocomposites may also be further improved.¹ A conceptually innovative solution for the design of magnetic scaffolds for tissue engineering was recently proposed.²

Accordingly, the aim of this work was to propose an approach in the design and development of 3D fiber deposited poly(ϵ -caprolactone)/iron oxide (PCL/Fe₃O₄) magnetic scaffolds. The effect of Fe₃O₄ nanoparticle inclusion on the biological, mechanical, and magnetic performances was also investigated.^{3,4}

2.1 Materials and Methods

2.1.1 Poly(ϵ -caprolactone)

Poly(ϵ -caprolactone) is a synthetic semicrystalline polymer, belonging to the family of linear aliphatic polyesters. It is a biodegradable thermoplastic polymer characterized by low viscosity and ease of processing, a low melting point (around 60°C), a low glass transition temperature (-60°C) if compared to other bioresorbable polymers.⁵ Its decomposition temperature is equal to 360°C. In addition, PCL has a good resistance against chlorine, oil, water and solvents in general. For this reason it has been approved by Food and Drug Administration (FDA). These features make it widely used in the field of biomedical applications for drug delivery devices, as suture or adhesion barrier, for tissue engineering, in odontology or dentistry.⁶ PCL is obtained from ring opening polymerization of ϵ -caprolactone, using as catalyst, the stannous octanoate (Figure 1).

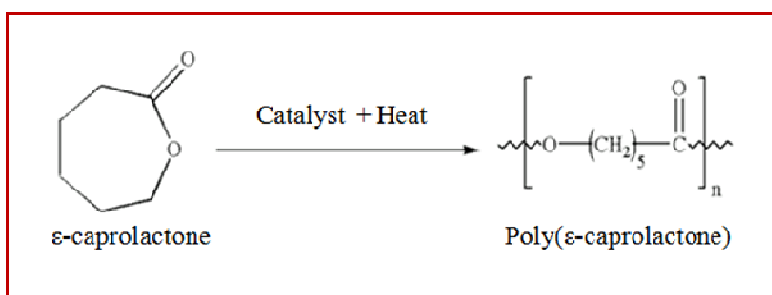


Figure 1: Ring opening polymerization of ϵ -caprolactone.

PCL is able to dissolve at room temperature when it is in contact with different solvents as dimethylacetamide (DMAc), tetrahydrofuran (THF) and chloroform (CLF), which are usually chosen, taking into account the specific field of application.

The most important chemical feature is its ability to degrade in the physiological environment; in particular, it is affected by degradation phenomena caused by the interaction between aliphatic ester bonds, presents along the main chain, and water molecules. This degradation mechanism activated

by chemical hydrolysis allows the polycaprolactone to be counted as one of the leading members of the class of bioerodible polymers.⁷

Several important factors influence hydrolysis kinetic:

- the diffusion coefficient of water in the polymer and the water absorption;
- the crystallinity of the polymer, since the amorphous areas are more quickly involved in the process being more accessible to water molecules;
- the temperature, since its increase up to values above the glass transition temperature of the material determines a greater mobility of chain, thus favoring the penetration of water;
- the chemical structure, in particular the presence of hydrophobic or hydrophilic groups can make the process more or less smooth;
- the surface morphology, since the presence of inhomogeneities and roughness accelerate typically the degradation process.

In particular, PCL degradation process consists of at least two discrete phases; the first one involves the non-enzymatic bulk hydrolysis of the ester bond auto-catalyzed by carboxylic groups present along the main chain, whereas the second one involves a surface erosion mechanism.

The amorphous phase firstly degrades, resulting in an increase in the degree of crystallinity, while the molecular weight remains constant.⁷ Then, cleavage of ester bonds results in a mass loss.^{8,9}

The polymer degrades by end chain scission at higher temperatures, while it degrades by random chain scission at lower temperatures.¹⁰

PCL degradation is auto-catalyzed by the carboxylic acids liberated during hydrolysis of the ester bond^{9,11} but it can also be catalyzed by enzymes, resulting in faster decomposition¹² since many microbes, in nature, are able to completely biodegrade PCL.¹³

Anyway, while PCL can be enzymatically degraded in the environment, it cannot be degraded enzymatically in the body.¹⁴

Many studies were made in order to better understand the degradation process of the PCL. For example, some studies have shown that free radicals, produced by the reaction between the carboxylic groups, are much more reactive than oxygen radicals produced by reaction with oxydrile groups (OH).¹¹ Other works aimed to study the evolution of physical and chemical properties during the degradation process.

Figure 2 shows the trend of the molecular weight (M_w) of the polymer in distilled water. It is clear that, due to the activation of hydrolysis, the breaking of bonds along the aliphatic macromolecules, which gradually become shorter, begins and this causes the loss of molecular weight, faster at first, and, then, most significant slower, until the complete degradation of the polymer.¹¹ Similarly, as the mechanism of degradation goes on, surface erosion mechanism plays a crucial role in determining a percentage reduction in the amount of polymer.¹⁵

The period of time where the degradation process takes place is pretty long: in distilled water, it is of about 30 weeks, in agreement with the figure 2.¹⁶

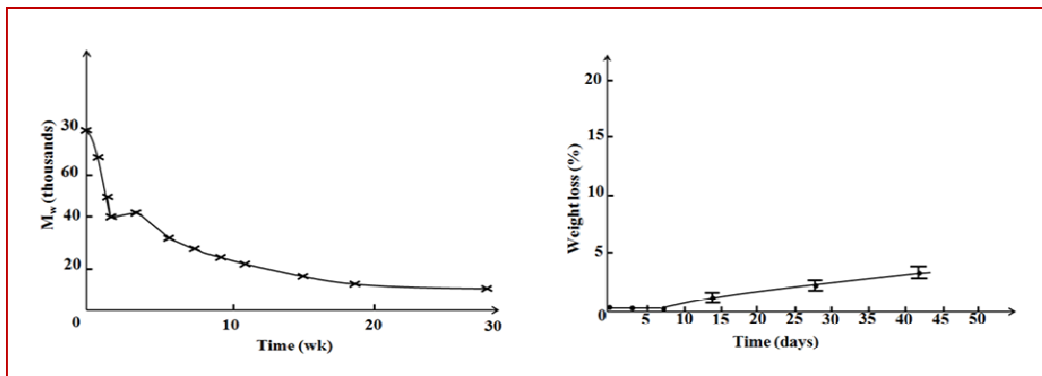


Figure 2: (left) PCL molecular weight (M_w) versus time, during degradation in distilled water; (right) PCL weight loss versus time, during degradation in distilled water.¹⁶

Sun et al. (2008) highlighted that the *in vivo* degradation of PCL was observed for 3 years in rats. The disruption, absorption and excretion of PCL were traced in rats by radioactive labeling. PCL capsules with initial molecular weight of 66000 g mol^{-1} remained intact in shape during 2-year implantation. It broke into low molecular weight ($M_w = 8000 \text{ g mol}^{-1}$) pieces at the end of 30

months. The molecular weight of PCL decreased with time and followed a linear relationship between $\log M_w$ and time (Figure 3).¹⁷

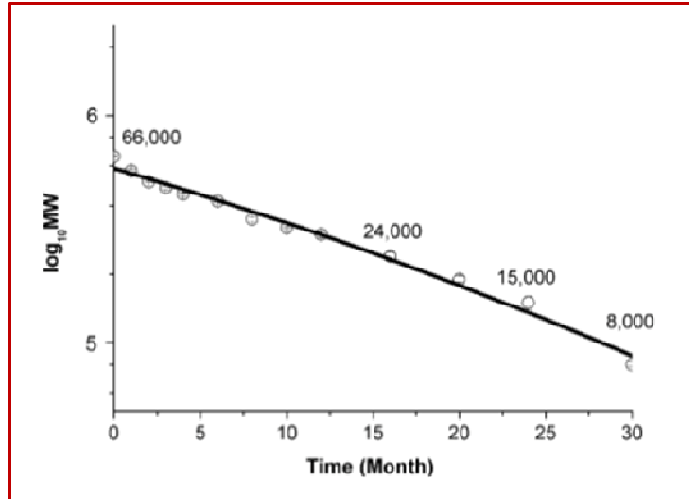


Figure 3: Decrease in the molecular weight (M_w) of PCL capsules, implanted in rats, with time. A linear relationship between the logarithm of M_w and time was observed.¹⁷

Due to its chemical structure, PCL is highly hydrophobic and the main limitation lies in its mechanical properties: compressive strength and tensile strength which are equal to 1.58 MPa¹⁵ and to 20.7 MPa,¹⁸ respectively. For this reason, research attention has been focused on the development of polymer-based composites consisting of polymers reinforced with inorganic ceramic micro/nanofillers. Compared with poly(ϵ -caprolactone), polymer-based composites possess enhanced mechanical properties, while showing flexibility and structural integrity better than ceramic materials.

2.1.2 Iron oxide nanoparticles

Since many years, different kinds of magnetic micro/nanoparticle carriers have been optimized and proposed for drug delivery, hyperthermia treatment and other applications. Magnetic nanoparticles (MNPs) may be properly shielded from the surrounding environment or functionalized/bioactivated with specific molecules, biocompatible polymers (i.e., Polyvinyl Alcohol (PVA),

Polyvinylpyrrolidone (PVP), dextran, or others). Inorganic silica-based materials have also been considered as coatings for magnetite (Fe_3O_4)^a or maghemite ($\gamma\text{-Fe}_2\text{O}_3$)^b MNPs.¹⁹

Iron oxide nanoparticles exhibit hydrophobic surfaces with a large surface area to volume ratio. Due to the hydrophobic interaction, these particles tend to agglomerate and to form clusters with an increase in overall particle size. The clusters display strong dipolar attractions to other particles and exhibit ferromagnetic behavior.^{20,21} Since magnetic attraction exists between particles, additional Van der Waals forces result in the usual aggregations, and therefore, in order to stabilize iron oxide nanoparticles, an appropriate surface modification is needed.²⁰ Moreover, it is worth noting that for medical applications the stabilized iron oxide nanoparticles should be nontoxic and biocompatible.²² An important strategy is represented by coating nanoparticles with several materials for biomedical applications including organic, inorganic, polymeric and non-polymeric materials.

In this stage of the work, magnetite nanoparticles coated by Polyvinylpyrrolidone (0.2 w % PVP) with an average diameter of about 25 nm (NanoAmor, Houston, TX) were used.^{3,4}

^a The cubic spinel Fe_3O_4 is ferromagnetic at temperature below 858 K. Magnetite particles are commonly synthesized by treating a solution of a mixture of iron salts (Fe^{2+} and Fe^{3+}) with a base under an inert atmosphere. For example, the addition of an aqueous solution of ammonia to a solution of FeCl_2 and FeCl_3 (1:2) yields nanoparticles, which are transferred into a hexane solution by treatment with oleic acid.^{23,24} The repeated selective precipitation gives Fe_3O_4 nanoparticles with a rather narrow size distribution.

^b Among several crystalline modifications of Fe_2O_3 , there are two magnetic phases, namely, rhombohedral $\alpha\text{-Fe}_2\text{O}_3$ (hematite) and cubic $\gamma\text{-Fe}_2\text{O}_3$ (maghemite) phases. In the $\gamma\text{-Fe}_2\text{O}_3$ all Fe^{3+} ions having the structure of a cation-deficient AB_2O_4 spinel, the metal atoms A and B occur in tetrahedral and octahedral environments, respectively.²³ A bulk $\gamma\text{-Fe}_2\text{O}_3$ sample is a ferrimagnet below 620°C. Nanoparticles are commonly obtained^{23,25} by mild oxidation (on treatment with Me_3NO) of pre-formed metallic nanoparticles. The same result can be attained by direct introduction of $\text{Fe}(\text{CO})_5$ into a heated solution of Me_3NO . The oxidation with air oxygen is also used to prepare $\gamma\text{-Fe}_2\text{O}_3$ nanoparticles. For this purpose, the Fe_3O_4 nanoparticles are boiled in water at pH 12-13. The most popular route to $\gamma\text{-Fe}_2\text{O}_3$ nanoparticles is thermal decomposition of Fe^{3+} salts in various media. For example, good results have been obtained by using iron complexes with cupferron.^{23,26,27}

2.1.3 Design and preparation of PCL/Fe₃O₄ nanocomposite scaffolds

PCL ($M_w = 65000$, Aldrich, St. Louis, MO) pellets were dissolved in tetrahydrofuran with stirring at room temperature. Polyvinylpyrrolidone coated Fe₃O₄ (NanoAmor, Houston, TX) nanoparticles and then ethanol were added to the PCL/THF solution during stirring. A PCL/Fe₃O₄ weight ratio (w/w) of 90/10 was used. An ultrasonic bath (Branson 1510 MT, Danbury, CT) was also used to optimize the Fe₃O₄ nanoparticle dispersion in the polymer solution. Accordingly, a homogeneous paste was obtained, and then, the solvent was totally removed. Successively, PCL/Fe₃O₄ (90/10 w/w) pellets were made. Nanocomposite fibers, 3D block-shaped scaffolds with a 0°/90° pattern and 3D cylindrical scaffolds with a 0₂°/90₂° lay-down pattern were preliminary manufactured by the processing PCL/Fe₃O₄ (90/10 w/w) pellets through a 3D fiber deposition technique.

In particular, nanocomposite scaffolds were built by extruding and alternatively depositing the fibers along the 0° direction and the 90° direction between successive layers, thus obtaining the selected lay-down pattern. PCL/Fe₃O₄ (90/10 w/w) pellets were initially placed in a stainless steel syringe and then heated at a temperature of 130–140°C with a heated cartridge unit placed on the mobile arm of a biplotter-dispensing machine (Envisiontec GmbH, Gladbeck, Germany). Successively, a nitrogen pressure of 8.5–8.9 bar was applied to the syringe through a cap. The nozzle used to extrude the PCL/Fe₃O₄ fibers was stainless steel characterized by an inner diameter of 400 or 600 µm. Scaffolds were characterized not only by the fiber diameter (depending on the needle diameter and/or the deposition speed) but also by the fiber spacing (strand distance, that is, center-to-center distance between two adjacent fibers) and layer thickness, which influenced the overall pore size. A deposition speed of 30 mm/min was used. Images of the PCL/Fe₃O₄ nanocomposite fibers and scaffolds are shown in figure 4.

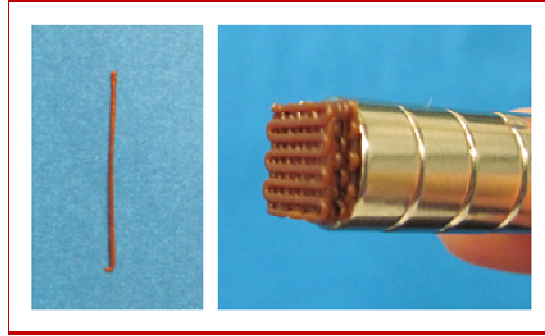


Figure 4: Representative image of a PCL/Fe₃O₄ nanocomposite fiber and of a 3D block-shaped PCL/Fe₃O₄ magnetic scaffold obtained through rapid prototyping technique, attracted by a neodymium magnet.

2.1.4 Morphological Analysis: Micro-CT and Optical Imaging

Micro-Computed Tomography (Micro-CT) was performed at a resolution of 5.8 μm through a SkyScan 1072 system (Aartselaar, Belgium) with a rotational step of 0.9° over an angle of 180° to capture the image and, hence, shape and size of the polymer and nanocomposite fibers. Cross-sections and 3D models of the nanocomposite fibers were then reconstructed with SkyScan's software package, Image J, and Materialise Mimics software (version 12.0, Materialise, Leuven, Belgium) for image analysis and visualization of the results from Micro-CT scanning.

Also, a Nikon Eclipse 80i microscope (Mellville, NY) equipped with a Nikon digital camera was used for optical imaging of the scaffolds.

2.1.5 Tensile Tests on PCL/Fe₃O₄ nanocomposite fibers

Tensile tests were performed, with an Instron 5566 dynamometer (Bucks, UK), on PCL and PCL/Fe₃O₄ nanocomposite fibers having a diameter (D) of 340–360 μm and 380 μm , respectively. The fiber length (l) between the grips was set to 20 mm. The fibers were tested at a constant crosshead speed of 50 mm/min, according to the standard practice ASTM D 3822. The engineering stress ($\sigma = F/A$) was obtained as the force measured by the loading cell divided by the total area of the fiber cross-section: $A = \pi D^2/4$, whereas the strain ($\varepsilon = \Delta l/l$) was defined as the ratio between the

vertical displacement (i.e., the elongation), assumed to be equal to the crosshead displacement, and the initial distance between the grips.

Statistical differences for the tensile modulus (E), maximum stress (σ_{max}), and maximum strain (ε_{max}) between the polymeric and nanocomposite groups were assessed with a one-way analysis of variance through the software package OriginPro 7 (Origin- Lab Corp., Northampton, UK).

2.1.6 Compression Tests on PCL/Fe₃O₄ nanocomposite scaffolds

Compression tests were carried out on 3D cylindrical scaffolds characterized by a diameter (D_0) of 6.0 mm, a height (h_0) of 6.5 mm, a 0°/90° pattern by a fiber diameter of 500 μm , a layer thickness of 390-400 μm , a center-to-center fiber distance of 1000 μm . All the tests were performed at a rate of 1 mm/min up to a strain value of 0.4 mm/mm, using an INSTRON 5566 testing machine (Bucks, UK). The stress ($\sigma = F/A_0$) was defined as the ratio between the force (F) measured by the load cell and the apparent cross-section of the scaffold ($A_0 = \pi D_0^2 / 4$). The strain ($\varepsilon = \Delta h / h_0$) was evaluated as the ratio between the scaffold height variation (Δh) and the initial height (h_0).

2.1.7 Magnetic Analysis

Magnetization measurements were performed in a Squid magnetometer (San Diego, CA) designed for the operation ranges $-7 \text{ T} \leq B \leq +7 \text{ T}$ and $1.8 \text{ K} \leq T \leq 400 \text{ K}$.

Firstly, direct-current magnetization and alternating-current susceptibility at low magnetic field - several millitesla (mT) - were measured as functions of temperature.

The field-dependent magnetization curve, which is of practical interest for biomedical applications, was taken at *in vivo* temperature conditions of $T = 310 \text{ K}$.

Assuming monodisperse particle size, we fitted the experimental curve with a Langevin function common for superparamagnetic behavior (see Appendix):

$$M = M_s \left(\coth(\mu_p H / k_B T) - k_B T / \mu_p H \right) \quad (1)$$

where M_s is the saturation magnetization, μ_p stands for the magnetic moment of a particle, k_B is the Boltzmann constant, T and H the temperature and the magnetic field.

2.1.8 Biological Analysis

Cell Adhesion Study

Human Mesenchymal Stem Cells (hMSCs, 1.0×10^4 cells/sample) were seeded on PCL and PCL/Fe₃O₄ substrates and grown in Dulbecco's modified Eagle medium (DMEM) supplemented with 10% fetal bovine serum (FBS, BioWhittaker, Walkersville, MD).

The different kinds of cell-constructs were analyzed through Confocal Laser Scanning Microscopy (CLSM). They were fixed with 4% paraformaldehyde, rinsed twice with phosphate-buffered saline (PBS buffer) and incubated with Phosphate-Buffered Saline and Bovine Serum Albumin (PBS-BSA 0.5%). Preliminary CLSM analyses were carried out to study human mesenchymal stem cell adhesion and spreading on the PCL/Fe₃O₄ nanocomposite fibers at 72 h after seeding. To visualize the cells adhered to the nanocomposite fibers, the phalloidin-labeled actin filament fluorescence intensity was measured with several steps along the length of the fibers by means of a confocal laser scanning microscope (Zeiss LSM 510/Confocor 2, Oberkochen, Germany).

Accordingly, actin microfilaments were stained with phalloidin-tetramethylrhodamine B isothiocyanate (Sigma Aldrich). Phalloidin was diluted in PBS-BSA 0.5% and incubated at room temperature for a suitable time. CLSM was equipped with helium–neon laser sources at a wavelength of 543 nm and with a 20x objective.

2.2 Results and Discussion

2.2.1 Morphological Analysis: Micro-CT and Optical Imaging

The first step of the morphological study through Micro-CT has involved the evaluation of the fiber diameter produced through a bioplotter, whereas the second one showed the distribution of Fe₃O₄ nanoparticle clusters. As for the diameter, the results have evidenced values of 340–360 and 380 μm for the PCL and PCL/Fe₃O₄ fibers, respectively.

The images obtained through the Micro-CT system scan have allowed for obtaining the 3D reconstruction of the nanocomposite fibers also assessing the distribution of Fe₃O₄ nanoparticles (Figure 5).

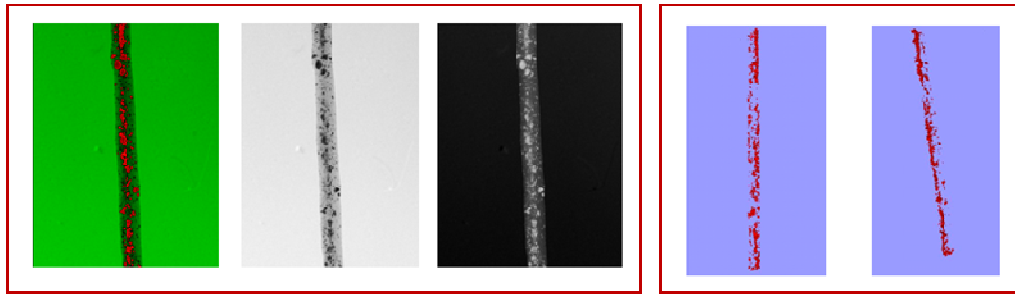


Figure 5: Two different reconstructions of nanocomposite fibers obtained through (left) Image J and (right) Materialise Mimics that have highlighted the distribution of Fe₃O₄ particles.

In particular, 3D reconstructions through Materialise Mimics have highlighted an evident distribution of Fe₃O₄ nanoparticle clusters; thus, a uniform distribution of nanoparticles along each fiber composing the scaffold was expected. The clustering effect of high surface-to-volume ratio particles is widely documented; levels much lower than 10% usually produce clusters. If clusters are effective for magnetic features of the scaffold, higher amount of clusters are known to drastically reduce the mechanical properties.

Figure 6 shows the imaging through optical microscopy of the investigated scaffolds. Optical imaging has shown that the fibers composing the scaffold were very well aligned and regularly spaced along each layer; this suggests proper performance of the fiber deposition process.

Moreover, a 100% interconnectivity among macropores was observed. Therefore, morphologically controlled composite scaffolds based on a PCL matrix can be fabricated in similar fashion to the neat PCL structures.²⁸⁻³⁰

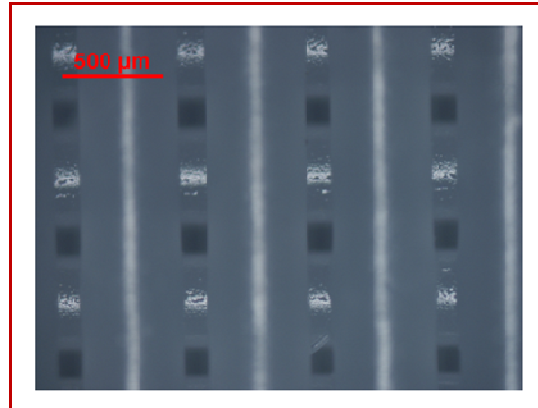


Figure 6: Optical microscopy image of a PCL/Fe₃O₄ scaffold showing that fibers composing the scaffold are very well aligned and regularly spaced along each layer, thus suggesting a proper performance of the 3D fiber deposition process.

2.2.2 Tensile Tests on PCL/Fe₃O₄ nanocomposite fibers

The results from the tensile tests have evidenced a ductile behavior for both the PCL and PCL/Fe₃O₄ fibers. Typical stress-strain curves are reported in figure 7.

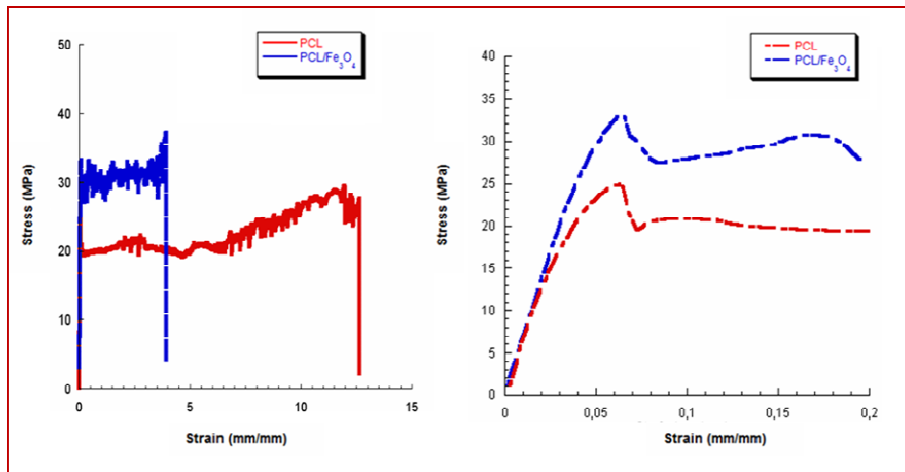


Figure 7: Typical stress-strain curves obtained from tensile tests performed on PCL and PCL/Fe₃O₄ fibers evidencing a ductile behavior: (left) Stress-strain curves reported up to break; (right) Stress-strain curves reported up to a strain level of 0.2 mm/mm in order to better highlight the initial mechanical behavior.

They have shown an initial linear region, firstly followed by a small decrease in the slope up to a local maximum stress (σ_{max}) value; and, then, by a decrease of the tensile stress.

It is worth noting that a plateau-like region and, finally, a new increase were observed until maximum stress (σ_{max}) was reached. Values of the tensile modulus (E), maximum stress (σ_{max}), and maximum strain (ϵ_{max}) are reported in Table I.

Fibers	E (MPa)	σ_{max} (MPa)	ϵ_{max} (mm/mm)
PCL	571.5 ± 45.6	29.3 ± 3.2	12.3 ± 2.0
PCL/Fe ₃ O ₄	640.0 ± 60.4	38.1 ± 4.1	5.5 ± 1.4

Table I: Tensile modulus (E), maximum stress (σ_{max}) and maximum strain (ϵ_{max}) reported as mean value ± standard deviation

In particular, the values of the modulus (E) obtained for the PCL fibers were consistent with the literature data;²⁸ however, the slightly greater value measured in this investigation may have been related to the higher speed of testing (50 mm/min).

Even though the inclusion of Fe₃O₄ nanoparticles strongly reduced the maximum strain (ϵ_{max}), the results have suggested that the modulus and maximum stress (σ_{max}) were enhanced. The increase of stiffness and strength observed for PCL/Fe₃O₄ have suggested that the use of 10% by weight of magnetic nanoparticles was still an effective reinforcement, even if a maximum effect was expected at lower amounts of nanoparticles. The higher number of clusters, which can be detected from figure 5, have highlighted that further increasing the amount of nanoparticles might break down mechanical properties. It is also interesting to observe that the mechanical properties of these scaffolds (Table I) were in the range of those related to trabecular bone. Therefore, the variation in the amount of nanoparticles may be a useful tool for tailoring mechanical features.

The results from the statistical analysis have highlighted a significant statistical difference between the polymeric and nanocomposite groups ($p < 0.01$) for both σ_{max} and ϵ_{max} , whereas a weaker

difference ($p < 0.05$) was observed for the modulus. Furthermore, the values of the modulus obtained for the fibers seemed to match those of trabecular bone.³¹

2.2.3 Compression Tests on PCL/Fe₃O₄ nanocomposite scaffolds

Results from compression tests have highlighted that the 3D rapid prototyped scaffolds show a mechanical behavior, which is similar to that of flexible foams.

A linear region is evident at low values of strain, suggesting an initial stiff mechanical response.

This zone is followed by a region with lower stiffness. Finally, another stiff zone of the stress-strain curve can be observed (Figure 8).

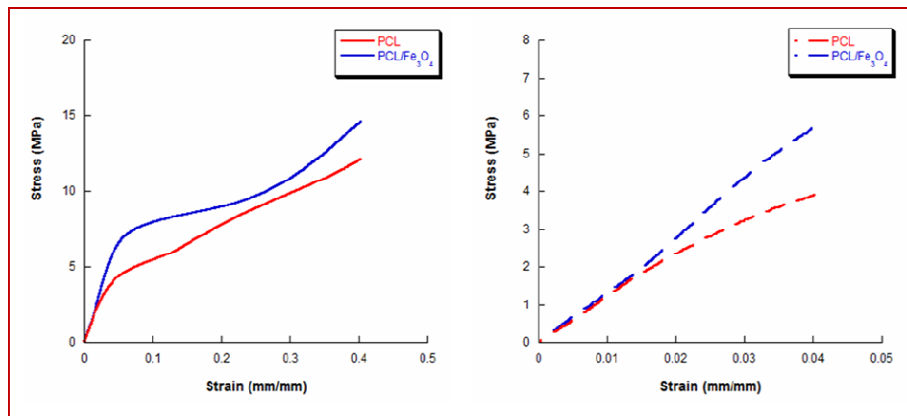


Figure 8: Typical stress-strain curves obtained from compression tests performed on PCL and PCL/Fe₃O₄ cylindrical scaffolds: left) Stress-strain curves reported up to a strain level of 0.4 mm/mm; (right) Stress-strain curves reported up to a strain level of 0.04 mm/mm in order to better highlight the initial mechanical behavior.

According to previous works,^{28,30} in contrast to the typical behavior of the flexible foams²⁸ and 3D scaffolds obtained through fused deposition modeling³² the central region of the stress-strain curve does not present a plateau, however, showing a lower stiffness in comparison with the other two regions of the curve.

Compressive modulus and maximum stress (at a strain level of 0.4 mm/mm) have been reported in Table II.

Scaffolds	Compressive modulus, E (MPa)	Maximum Stress, σ_{max} (MPa)
PCL	92.1 ± 19.1	12.1 ± 1.9
PCL/Fe ₃ O ₄	132.3 ± 19.7	14.5 ± 2.3

Table II: Compressive modulus (E) and maximum stress (σ_{max}) at a strain level of 0.4 mm/mm reported as mean value ± standard deviation.

2.2.4 Magnetic Analysis

The magnetization curves, have shown a superparamagnetic behavior at 310 K for these PCL-based scaffolds containing 10% by weight of magnetic Fe₃O₄ nanoparticles with a blocking temperature at about 250 K (Figure 9).

The particle moment (μ_p), estimated from Langevin fit, was about $10^6 \mu_B$. As each Fe₃O₄ molecule carried a magnetic moment of $4.7 \mu_B$, a particle diameter of about 28 nm has been estimated, which was equivalent to a particle mass of about $2 * 10^5$ Fe₃O₄ molecules. This agreed well with the grain diameter provided by the producer. This further result has suggested a mass concentration of nanoparticles of $N=M_s/\mu_p \approx 1.5*10^{15}$ particles per gram where M_s is the saturation magnetization.

Even if the saturation value was low if compared to a dip-coated scaffold,² it was still encouraging because these scaffolds could be attracted and fixed by a magnetic field and they were capable of attracting magnetized bioaggregates used for scaffold functionalization, benefiting from the fully interconnected porosity of the 3D rapid prototyped structures.

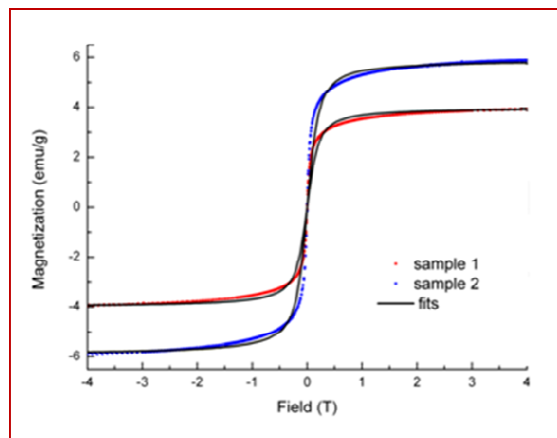


Figure 9: Magnetic moment per mass measured at 310 K for two different PCL/Fe₃O₄ samples. Black solid lines represent fits of the Langevin function to the experimental data points.

2.2.5 Biological Analysis

Cell Adhesion Study

Confocal images have shown interesting results in terms of cell adhesion and spreading (Figure 10 and 11). Hence, preliminary studies suggest a high ability of the magnetic scaffolds to support adhesion and proliferation human bone marrow stem cells, at least *in vitro*. Therefore, this new type of scaffold is a valuable candidate for tissue engineering applications and offers novel magnetic options.

In particular, confocal analysis has highlighted an increase in the adhered number and a more evident spreading of human mesenchymal stem cells when compared to the results usually obtained from only PCL fibers. This could have probably been due to the presence of Fe₃O₄ nanoparticles or to the surface topography and roughness of the nanocomposite fibers. With regard to the release of nanoparticles, several *in vitro* and *in vivo* investigations have already confirmed that magnetic nanoparticles with adequate biocompatible coatings do not have cytotoxic effects on cell behavior.³³ Furthermore, some magnetic nanoparticles coated with arginine-glycine-aspartic acid (RGD) peptides showed good biocompatibility in contact with osteoblasts.³⁴

Dobson J. (2008) also highlighted that the change in the magnetic properties of magnetic nanoparticles in the presence of a magnetic field had no influence on cellular toxicity³⁵. However, further research is needed to assess whether this enhanced cell-material behavior is related to the presence of magnetic Fe₃O₄ powder or to changes in the surface topography of fibers as a consequence of the presence of nanoparticles.

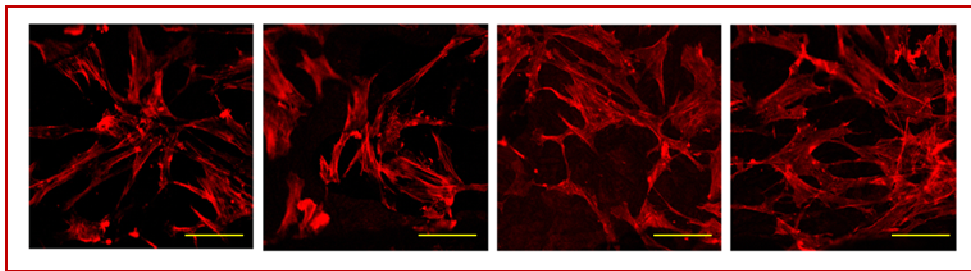


Figure 10: Images obtained from confocal analysis with several steps along the length of the nanocomposite fibers, highlighting the phalloidin-labeled actin filaments. Scale Bar - 100 μ m

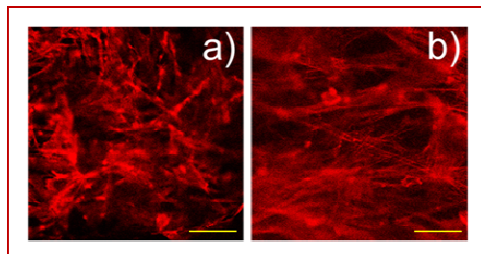


Figure 11: Image obtained from confocal analysis: (a) evidencing the great number of cells adhered to the scaffold; Scale Bar - 100 μ m (b) a higher magnification (Scale Bar - 50 μ m) of the central zone reported in figure (a).

Conclusions

Fully interconnected PCL/Fe₃O₄ nanocomposite magnetic scaffolds were successfully prototyped through 3D fiber deposition. An amount of 10% by weight of nanoparticles enhanced stiffness and strength of the scaffolds and provided magnetic features that allowed the design of novel fixation methods and functionalization of the scaffold, thus providing novel strategies for designing scaffolds for bone tissue engineering. Moreover, a biological *in vitro* investigation has suggested an increase in the adhered number and a marked spreading of human mesenchymal stem cells.

Dr. A. Sytcheva and prof. T. Herrmannsdörfer from Helmholtz-Zentrum Dresden-Rossendorf (HZDR), Dresden High Magnetic Field Laboratory (HLD), Dresden, Germany, dr. C. Dionigi and Prof. V.A. Dediu from the Institute of Nanostructured Materials, National Research Council, Bologna, Italy are gratefully acknowledged for their support and collaboration in the magnetic analysis of nanocomposite scaffolds.

References

1. Rogel M.R., Qiu H., Ameer G.A. The role of nanocomposites in bone regeneration. *J. Mater. Chem.* 18: 4233, 4242, 2008.
2. Bock N., Riminucci A., Dionigi C., Russo A., Tampieri A., Landi E., Goranov V.A., Marcacci M., Dediu V. *A novel route in bone tissue engineering: magnetic biomimetic scaffolds.* *Acta Biomater.* 6: 786-796, 2010.
3. De Santis R., Gloria A., Russo T., D'Amora U., Zeppetelli S., Ambrosio L. *An approach in developing 3D fiber-deposited magnetic scaffolds for tissue engineering.* In: D'Amore A., Acierno D. and Grassia L., eds. Vth International Conference on Times of Polymers (TOP) and Composites. Am. Inst. Phys. Melville, New York. 420-2, 2010.
4. De Santis R., Gloria A., Russo T., D'Amora U., Zeppetelli S., Dionigi C., Sytcheva A., Herrmannsdörfer T., Dediu V.A., Ambrosio L. *A Basic Approach Toward the Development of Nanocomposite Magnetic Scaffolds for Advanced Bone Tissue Engineering.* *J. Appl. Pol. Sc.*122: 3599–3605, 2011.
5. Iroh J.O. *Poly(ϵ -caprolactone).* In: Polymer Data Handbook. Mark JE (ed.), Oxford Press, Oxford. 361–362, 1999.
6. Langer R. *Selected advances in drug delivery and tissue engineering.* *J. Contr. Rel.* 62: 7-11, 1999.
7. Lam C.X.F., Teoh S.H., Hutmacher D.W. *Comparison of Degradation of PCL & PCL-TCP scaffolds in Alkaline Medium.* *Polymer Inter.* 56: 718–728, 2007.
8. Peña J., Corrales T., Izquierdo-Barba I., Doadrio A.L., Vallet-Regí M. *Long term degradation of poly(ϵ -caprolactone) films in biologically related fluids.* *Pol. Degrad. Stabil.* 91: 1424–1432, 2006.
9. Sinha V.R., Bansal K., Kaushik R., Kumria R., Trehan A. *Poly- ϵ -caprolactone microspheres and nanospheres: an overview.* *Inter. J. Pharm.* 278: 1–23, 2004.
10. Joshi P., Madras G. *Degradation of polycaprolactone in supercritical fluids.* *Pol. Degrad. Stabil.* 93: 1901–1908, 2008.
11. Bancroft G.N., Mikos A.G. *Fluid flow increases mineralized matrix deposition in 3D perfusion culture of marrow stromal osteoblasts in a dose- dependent manner.* *Proceed. Nat. Acad. Sci. USA.* 99: 12600–12605, 2002.
12. Chen D.R., Bei J.Z., Wang S.G. *Polycaprolactone microparticles and their biodegradation.* *Pol. Degrad. Stabil.* 67: 455–459, 2000.
13. Gross R.A., Kalra B. *Biodegradable Polymers for the Environment.* *Science.* 297: 803–807, 2002
14. Ikada Y., Tsuji H. *Biodegradable polyesters for medical and ecological applications.* *Macromol. Rapid Comm.* 21: 117–132, 2000.

62 - Chapter 2

15. Ramakrishna S., Mayer J., Wintermantel E., Leong K.W. *Biomedical applications of polymer-composite materials: a review*. Compos. Sc. Technol. 61: 1189-122, 2001.
16. Ali S.A.M., Zhong S.P., Doherty P.J., Williams D.F. *Mechanism of polymer degradation in implantable devices*. Biomaterials. 14: 1409-1418, 1993.
17. Sun H., Mei L., Song C., Cui X., Wang P. *The in vivo degradation, absorption and excretion of PCL-based implant*. Biomaterials. 27: 1735–1740, 2006.
18. Yu X., Laurencin C.T. *Bioreactor-based bone tissue engineering*. PNAS. 101: 11203-11208, 2004.
19. Pankhurst Q.A., Connolly J., Jones S.K., Dobson J. *Applications of magnetic nanoparticles in biomedicine*. J. Phys. D Appl. Phys. 36: R167–R181, 2003.
20. Gupta A.K., Gupta M. *Synthesis and surface engineering of iron oxide nanoparticles for biomaterial applications*. Biomaterials. 26: 3995-4021, 2005.
21. Hamley I.W. *Nanotechnology with Soft Materials*. Angew. Chem. Int. Ed. 42: 1692 –1712, 2003.
22. Ito A., Shinkai M., Honda H., Kobayashi T. *Medical application of functionalized magnetic nanoparticles*. Soc. biotech. 100: 1-11, 2005.
23. Gubin P.S., Koksharov Y.A., Khomutov G.B., Yurkov G.Y. *Magnetic nanoparticles: preparation, structure and properties*. Rus. Chem. Rev. 74 (6): 489 - 520, 2005.
24. Fried T., Shemer G., Markovich G. *Ordered Two-Dimensional Arrays of Ferrite Nanoparticles*. Adv. Mater. 13: 1158, 2001.
25. Tang J., Myers M., Bosnick K.A., Brus L.E. *Magnetite Fe₃O₄ Nanocrystals: Spectroscopic Observation of Aqueous Oxidation Kinetics*. J. Phys. Chem. B 107: 7501, 2003.
26. Rockenberger J., Scher E.C., Alivisatos A.P. *A new nonhydrolytic single-precursor approach to surfactant-capped nanocrystals of transition metal oxides*. J. Am. Chem. Soc. 121: 11595, 1999.
27. Hyeon T., Lee S.S., Park J., Chung Y., Na H.B. *Synthesis of highly crystalline and monodisperse maghemite nanocrystallites without a size-selection process*. J. Am. Chem. Soc. 123: 12798, 2001.
28. Kyriakidou K., Lucarini G., Zizzi A., Salvolini E., Mattioli Belmonte M., Mollica F., Gloria A., Ambrosio L. *Dynamic Co-Seeding of Osteoblast and Endothelial Cells on 3D Polycaprolactone Scaffolds for Enhanced Bone Tissue Engineering*. J. Bioact. Compat. Polym. 23: 227-243, 2008.
29. Gloria A., De Santis R., Ambrosio L. *Polymer-based composite scaffolds for tissue engineering*. J. Appl. Biomater. Biomech. 8: 57-67, 2010.

30. Gloria A., Russo T., De Santis R., Ambrosio L. *3D fiber deposition technique to make multifunctional and tailor-made scaffolds for tissue engineering applications*. J. Appl. Biomater. Biomech. 7: 141-152, 2009.
31. De Santis R., Ambrosio L., Mollica F., Netti P., Nicolais L. In *Modeling of Biological Materials*; Mollica F., Preziosi L., Rajagopal K.R., Eds.; Birkhauser: Boston, 2007.
32. Hutmacher, D.W., Schantz T., Zein I., Ng K.W., Teoh S.H., Tan K.C. *Mechanical properties and cell cultural response of polycaprolactone scaffolds designed and fabricated via fused deposition modelling*. J. Biomed. Mat. Res. 55: 203-216, 2001.
33. Butoescu N., Seemayer C.A., Foti M., Jordan O., Doelker E. *Dexamethasone-containing PLGA superparamagnetic microparticles as carriers for the local treatment of arthritis*. Biomaterials. 30: 1772, 2009.
34. Hughes S., Dobson J., El Haj A.J. *Magnetic targeting of mechanosensors in bone cells for tissue engineering applications*. J. Biomech. 40: S96, 2007.
35. Dobson J. *Remote control of cellular behaviour with magnetic nanoparticles*. Nat. Nanotechnol. 3: 139, 2008.

Chapter 3

Poly(ϵ -caprolactone)/iron-doped hydroxyapatite nanocomposite magnetic substrates

Preface

Even though iron oxide-based phases such as maghemite or magnetite have been widely considered in biomedical applications, their long-term effects in the human body remain still unclear.¹⁻³ Clearly, the development of suitably surface-modified magnetic nanoparticles (MNPs) through the design of specific biocompatible layers consisting of polymers, inorganic phases or metals deposited on their surface avoid dangerous problems related to their eventual toxicity, such as to leave any non bioresorbable magnetic inclusion (for example, magnetite) inside the repaired tissue.^{1,4,5} Consequently, research attention has been focused on the synthesis of biocompatible and fully biodegradable materials as iron-doped hydroxyapatite (HA) nanoparticles, that can be potentially employed to develop new magnetic ceramic scaffolds with enhanced regenerative properties for bone surgery.^{4,6,7}

Chemical modification and the engineering of hydroxyapatite has been widely investigated in order to produce new biomimetic non-stoichiometric apatites which would better resemble the chemical composition and structure of the mineral phase in bones, providing higher rate of biodegradability and bioactivity compared to stoichiometric apatites or to improve HA mechanical properties by optimizing the processing and the sintering regimes.^{6,8-10}

The ionic substitutions can modify the surface structure and electrical charge of HA. Among the substituents of the calcium ion (Ca^{2+}), Mg^{2+} is of great interest.

The effect of Mg ion substitution on the crystallization of HA has been reported in literature. The presence of Mg ion accelerates the nucleation kinetics of HA, inhibits its crystallization, producing a synthetic apatite more similar to natural one.^{6,8-10}

Mg-doped hydroxyapatite results more soluble and absorbable than non-doped apatites but there is a limit to the introduction of Mg ion into the apatite network without altering the reticular structure. The introduction of carbonate ions (CO_3^{2-}) into the apatite structure may allow to increase Mg ion substitution. The carbonate ion can partially substitute the OH^- sites (site A), leading to an apatite characterized by less affinity to osteoblast cell, and/or the PO_4^{3-} (site B) leading to an apatite less crystalline and more soluble if compared to stoichiometric apatites. However, Mg ions are bivalent as Ca ions, thus carbonate ion is not forced to substitute in the site B.^{6,8,9} Consequently, the co-substitution of Mg and CO_3 ions into HA structure has allowed to obtain a biomimetic apatite.

In the last years, great efforts have been directed toward the synthesis of iron-doped hydroxyapatites.

By stressing the importance of having nontoxic MNPs for all the above-mentioned applications, Tampieri A. et al. (2012) synthesized a novel biocompatible and bioresorbable superparamagnetic-like phase by doping hydroxyapatite with $\text{Fe}^{3+}/\text{Fe}^{2+}$ ions, minimizing the formation of magnetite as secondary phase (Italian Patent MI2010A001420). Microstructural, physico-chemical and magnetic analyses were carried out on the nanoparticles, highlighting their intrinsic magnetization and suggesting new perspectives for devices for bone tissue engineering and for anti-cancer therapies based on hyperthermia.⁴

In this further step of the research, the mechanical, biological and magnetic performances of the proposed poly(ϵ -caprolactone)/iron-doped hydroxyapatite (PCL/FeHA) nanocomposite substrates were properly evaluated.

The study has involved the design, the preparation and the characterization of magnetic substrates obtained through molding and solvent casting techniques employing different polymer-to-particle weight ratios (w/w).

3.1 Materials and Methods

3.1.1 Iron-doped hydroxyapatite synthesis

The intrinsic magnetic hydroxyapatite used in this work was suitably synthesized by the Institute of Science and Technology for Ceramics (ISTEC), National Research Council (CNR), Faenza, Italy.

As reported in literature, a new class of magnetic hydroxyapatites has been already synthesized to avoid the problems of toxicity that are usually related to iron oxide-based phases. Their synthesis involves a neutralization method used to synthesize HA nanopowders and a partial substitution of Ca ion by Fe^{2+} and Fe^{3+} ions that can enter the HA lattice, as highlighted in a previous work.⁴

In particular, by simultaneously adding both Fe species under specific and controlled synthesis conditions, it has been possible to obtain an iron-doped hydroxyapatite characterized by a (Fe–Ca)/P molar ratio very similar to the theoretical ratio ($\text{Ca}/\text{P} = 1.67$), $\text{Fe}^{3+}/\text{Fe}^{2+}$ ratio of about 3 and a negligible amount of magnetite as secondary phase.

The biocompatibility and the intrinsic magnetism of these FeHA nanoparticles have been properly assessed by Tampieri A. et al. (2012), proposing the possibility to potentially use magnetic hydroxyapatites for developing magnetic ceramic scaffolds with improved properties for bone regeneration, thus opening novel frontiers in the field of regenerative medicine.⁴

A superparamagnetic-like behavior of single-domain magnetic nanoparticles has been evidenced by the magnetization curves as a function of the applied magnetic field.⁴

FeHA nanoparticles were prepared according to the method previously described.⁴ A basic suspension of calcium hydroxide $\text{Ca}(\text{OH})_2$, (Aldrich, 95 w% pure, 50 g in 400 mL of H_2O) was stirred and heated to 40°C. $\text{FeCl}_2 \cdot 4\text{H}_2\text{O}$ (Aldrich, ≥ 99 w% pure, 12.74 g in 75 mL of H_2O) and $\text{FeCl}_3 \cdot 6\text{H}_2\text{O}$ (Aldrich, 97 w% pure, 17.86 g in 75 mL of H_2O) solutions were contemporarily added to the basic suspension as sources of Fe^{2+} and Fe^{3+} ions. The total amounts of iron ions with respect to calcium ions were adjusted so as to obtain: $\text{Fe}/\text{Ca} = 0.20$ mol.

After soon, a phosphoric-acid (Aldrich, 85 w% pure, 44.40 g in 300 mL of H₂O) solution was drop-wise added into the basic suspension of calcium hydroxide containing iron ions, over a period of 2 h, under constant heating and stirring.

The reaction products were kept in suspension by constant stirring and heating for 1 h, and then left ageing for 24 h at room temperature without further stirring. The precipitate was separated from mother liquor by centrifugation, and then washed with distilled water and centrifuged three times; finally it was freeze-dried and sieved at 150 µm. In figure 1 the iron-doped HA synthesized by ISTEC-CNR is schematically reported.

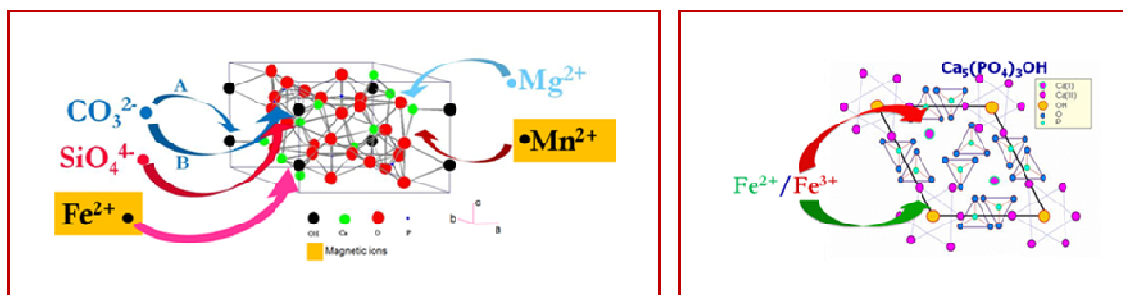


Figure 1: Schematic representation of iron-doped hydroxyapatite synthesized by ISTEC-CNR, Faenza, Italy.

Fe³⁺ ions are present preferentially at the surface level whereas at the bulk level, Fe²⁺ ions are distributed on both Ca(I) and Ca(II) with a preferential occupation of Ca(II) with sixfold coordination, on the other hand, Fe³⁺ ions are distributed on both Ca(I) and Ca(II) with a preferential occupation of Ca(I) with fourfold coordination (Figure 1).

3.1.2 Design and preparation of PCL/FeHA nanocomposite substrates

Magnetic nanocomposite substrates were produced by embedding FeHA nanoparticles into a PCL matrix.

Poly(ϵ -caprolactone) ($M_w = 65000$ – Sigma Aldrich, St. Louis, Mo) pellets were dissolved in tetrahydrofuran (THF) under stirring at room temperature.

FeHA nanoparticles having a diameter lower than 20 nm were added to the PCL/THF solution during stirring and three different polymer-to-particle weight ratios (w/w) (90/10, 80/20 and 70/30 w/w) were employed. An ultrasonic bath (Branson 1510 MT, Danbury CT) was also used to optimize the nanoparticle dispersion in the polymer solution. Then, molding and solvent casting techniques were used to manufacture miniature disk-shaped specimens (Figure 2) with a diameter of 6.4 mm and a thickness of 0.5 mm.

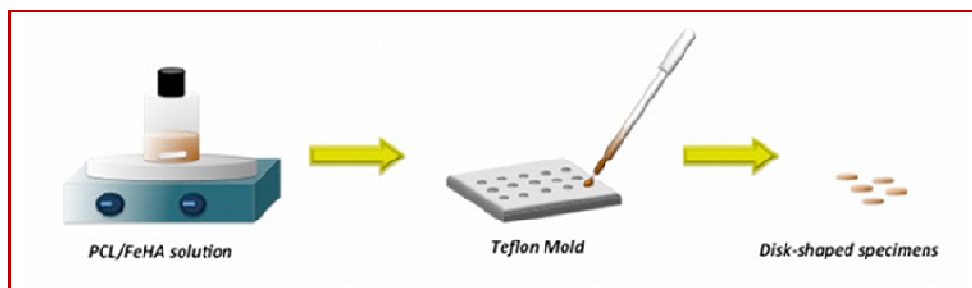


Figure 2: Schematic representation of molding and solvent casting technique used to obtain polymeric and nanocomposite disk-shaped specimens.

To determine the phase composition and crystallinity, PCL/FeHA nanocomposite substrates were analyzed through X-ray diffraction (XRD). To this aim, a D8 Advance Diffractometer (Bruker, Karlsruhe, Germany) was employed and the nanocomposite substrates were scanned from $2\theta = 10^\circ$ to $2\theta = 60^\circ$ using Cu-K α radiation.

3.1.3 Morphological Analysis: SEM/EDS and Micro-CT

In order to study the characteristics of the substrates, a Scanning Electron Microscopy/Energy Dispersive X-ray Spectroscopy (SEM/EDS) and Micro-Computed Tomography (Micro-CT) analysis were performed on PCL and PCL/FeHA substrates.

In particular, SEM was employed to evaluate the morphology of the PCL/FeHA nanocomposites by using a FEI Quanta FEG 200 scanning electron microscope (The Netherlands) while EDS was used to determine whether the small particles observed in the nanocomposites were FeHA nanoparticles or not, and SEM-EDS P-, Ca-, and Fe-mapping were considered to assess the dispersion of FeHA nanoparticles in the polymer matrix.

Finally, a Micro-CT analysis was performed on disk-shaped PCL/FeHA specimens, using a SkyScan 1072 system (Aartselaar, Belgium). A rotational step of 0.9° over an angle of 180° was employed in order to visualize the morphological features and surface topography. Cross-sections and 3D models of PCL/FeHA nanocomposite substrates were reconstructed using SkyScan's software package, Image J software, Materialise Mimics and Rapidform 2006 that allowed for analyzing the results from Micro-CT system scan.

3.1.4 Contact Angle Measurements

The hydrophilic nature of a material, together with its chemical composition and its morphological features, should be important to determine its ability to interact with the biological environment. To this aim, contact angle measurements were performed on PCL and PCL/FeHA substrates by using a DataPhysics OCA 20 apparatus. Briefly, distilled water was dropped onto at least 5 different sites on each specimen and the static contact angle was measured. Results were reported as mean value \pm standard deviation.

3.1.5 Small Punch Tests

Small punch tests were carried out on PCL/FeHA disk-shaped specimens with a diameter of 6.4 mm and a thickness of 0.5 mm according to the ASTM F 2183 standard, in order to evaluate maximum load and displacement at maximum load. All the tests were performed using an INSTRON 5566 testing machine (Bucks, UK).

The experimental setup consisted of a die, a hemispherical head punch, and a guide for the punch (Figure 3).



Figure 3: Experimental setup used to perform small punch test according to ASTM F2183 standard.

The specimen was loaded axisymmetrically in bending by the hemispherical head punch at a constant displacement rate of 0.5 mm/min until failure occurred. The values of load and displacement of the punch were recorded continuously while performing the test.

3.1.6 Magnetic Analysis

Magnetization measurements were performed by using a Superconducting Quantum Interference Device (SQUID) magnetometer. This instrument measures the total magnetic moment of a sample, including all atomic and molecular magnetic contributions. Due to size restrictions, a small part of sample material was carefully cut away from the scaffolds, and then fixed in a specially designed sample holder, which allows for cancelling background contributions to the total magnetic moment.

During the measurements, the magnetic field in the superconducting coil was either held constant at varying temperatures, or was swept at constant temperature, while the samples were consistently moved through a pick-up coil system connected to the SQUID via a flux transformer. Magnetization data were taken at temperatures $5\text{ K} < T < 350\text{ K}$ using a liquid-He cooled variable-temperature insert installed in the commercial SQUID-magnetometer setup (MPMS, Quantum Design Inc., San Diego, USA). In order to scale the measured magnetic moments to the amount of substance, the weight of the sample was determined with great care.

On the other hand, magnetic hyperthermia characterizations were performed applying a radio-frequency (RF) magnetic field to the samples, which were placed in a thermally isolated Teflon holder while temperature was simultaneously recorded with an optical fiber thermometer. Both frequency and amplitude of the oscillating magnetic field ($f=260\text{ kHz}$ and 27 mT , respectively) were generated with a home-made alternating current source feeding a refrigerated copper coil. The hyperthermia device has been designed to be into the safety specific absorption rate range for *in vivo* applications.

3.1.7 Biological Analysis

Bone marrow-derived human mesenchymal stem cells (hMSCs, Clonetics, Italy) were maintained at $37\text{ }^{\circ}\text{C}$ and 5% CO_2 in Dulbecco's modified Eagle medium (DMEM) supplemented with 10% fetal bovine serum (FBS, BioWhittaker, Walkersville, MD), 2 mM L-glutamine (Sigma Aldrich, St. Louis, MO), 1000 U/l penicillin (Sigma, St. Louis, MO) and 100 mg/l streptomycin (Sigma Aldrich, St. Louis, MO).

Disk-shaped PCL/FeHA substrates were prepared for cell seeding by soaking first in 70% ethanol for 1 h , then in 1% antibiotic/antimycotic in Phosphate-Buffered Saline (PBS) for 2 h and pre-wetted in medium for 2 h . Cells were statically seeded onto the PCL and PCL/FeHA nanocomposite substrates using a density of 1.0×10^4 cells/sample and grown in DMEM w/o FBS.

Cell Adhesion Study

Different kinds of cell-constructs (PCL-hMSCs and PCL/FeHA-hMSCs) were analyzed through Confocal Laser Scanning Microscopy (CLSM, Zeiss LSM 510/Confocor 2, Oberkochen, Germany). They were fixed with 4% paraformaldehyde, rinsed twice with PBS buffer and incubated with phosphate-buffered saline and bovine serum albumin (PBS-BSA 0.5%). Actin microfilaments were stained with phalloidin-tetramethylrhodamine B isothiocyanate (Sigma Aldrich). Phalloidin was diluted in PBS-BSA 0.5% and incubated at room temperature for a suitable time. The images of cell-constructs were acquired by using a He-Ne excitation laser at the wavelength of 543 nm and a 20X objective.

Alamar Blue™ assay

Cell viability and proliferation were evaluated by using the Alamar Blue™ assay. The Alamar Blue is a soluble and non toxic dye; it is stable in the culture medium. When it is added to the culture medium, it is taken up by cells in their cytoplasm, reduced from the metabolic activity, very intense in the cells in the proliferation stage, and returned to the medium. Alamar Blue™ assay is based on a redox reaction, that occurs in the mitochondria of the cells and that is accompanied by significant variations in color and fluorescence intensity; the colored product, transported out of the cell, can be measured through a spectrophotometer. The number of viable cells correlates with the magnitude of dye reduction^{1,11-14} and it is expressed as a percentage of Alamar Blue™ reduction according to the manufacturer's protocol.

In particular, at 7, 14, and 21 days after seeding, the cell-constructs were rinsed with PBS (Sigma Aldrich, Italy), and for each sample, 200 µl of Dulbecco's modified Eagle's medium (DMEM) without Phenol Red (HyClone, UK) containing 10% (v/v) Alamar Blue™ (AbD Serotec Ltd, UK) was added, followed by incubation in 5% CO₂ diluted atmosphere for 4 h at 37°C.

A specific volumetric amount of solution was then removed from the wells and transferred to a new 96-well plate. The optical density was immediately measured using a spectrophotometer (Sunrise;

Tecan, Männedorf, Zurich, Switzerland) at wavelengths of 570 and 595 nm. Each test was repeated at least three times in triplicate.

ALP/DNA assay

As CLSM analyses and Alamar Blue™ assay have allowed for obtaining qualitative and quantitative information on cell adhesion and viability/proliferation, respectively, Alkaline Phosphatase (ALP/DNA) measurements were used to assess the osteogenic expression of hMSCs as ALP is an early marker for the osteogenic differentiation of cells. The alkaline phosphatase is a dimeric glycoprotein (hydrolase enzyme) of the cell membrane, which is responsible for removing phosphate groups from many types of molecules, including nucleotides, proteins, and alkaloids. The process of removing the phosphate group is called dephosphorylation. This enzyme has a critical role in the formation of hydroxyapatite crystals and, therefore, in the beginning of the extracellular matrix mineralization.

Samples were removed from the medium and washed twice with PBS on days 7, 14 and 21. The substrates were then submerged into 1 mL of lysis buffer. ALP activity was measured using a specific biochemical assay. The substrates were then centrifuged and the supernatant was used to calculate the alkaline phosphatase activity by the p-nitro phenyl phosphate (p-NPP) method (Sensolyte® pNPP Alkaline Phosphatase Assay Kit). In particular, alkaline phosphatase is associated with a secondary antibody, using paranitrophenyl-phosphate (pNPP) as substrate. pNPP after being dephosphorylated by the ALP, is yellow colored making it possible to detect its presence at a wavelength of 405 nm. Thus the ALP activity can be detected by measuring the amount of p-nitrophenol at 405 nm.

ALP/DNA was then reported by using the Quant-iT™ PicoGreen® assay kit that allows to detect and quantify DNA. Cultures were performed in both standard and osteogenic differentiation medium (+OM, Sigma–Aldrich).

3.2 Results and Discussion

Magnetic activation results in an interesting strategy that has been previously proposed to answer the increasing need for assisted bone and vascular remodeling.⁴

The idea to design biodevices that should be biologically manipulated or activated *in situ* by applying an external magnetic field results in a great challenge in tissue engineering.

Accordingly, trying to benefit from the biocompatibility/degradability of superparamagnetic FeHA nanoparticles that should overcome the side effects of long-term cytotoxicity, an interesting idea has been to develop nanocomposite substrates for bone tissue engineering by embedding FeHA nanoparticles into a PCL matrix.

XRD analysis has confirmed that the synthesis process used to realize such PCL/FeHA magnetic substrates does not modify the structure and the crystallinity of the magnetic iron-doped hydroxyapatite. Just as an example, the XRD analysis relative to PCL/FeHA 70/30 nanocomposite is reported in figure 4. The XRD analysis has evidenced the presence of peaks ascribed to the organic (PCL) phase and also to the inorganic (FeHA) phase which shows the same features of the starting FeHA powder (Figure 4)⁴.

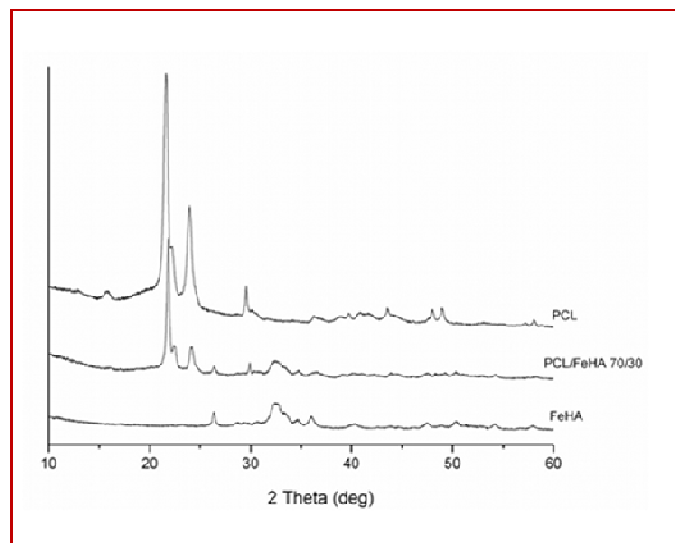


Figure 4: XRD spectra relative to PCL, FeHA and the nanocomposite containing the biggest amount of magnetic phase (PCL/FeHA 70/30).

3.2.1 Morphological Analysis: SEM/EDS and Micro-CT

SEM analysis has allowed to evaluate morphological features of the substrates. In particular, all of the substrates have the same structure and morphology except for PCL/FeHA 90/10 nanocomposite, which is characterized by the presence of several pores, randomly distributed, due to solvent extraction. Just as an example, in figure 5 SEM images of PCL/FeHA 90/10 and PCL/FeHA 80/20 are reported.

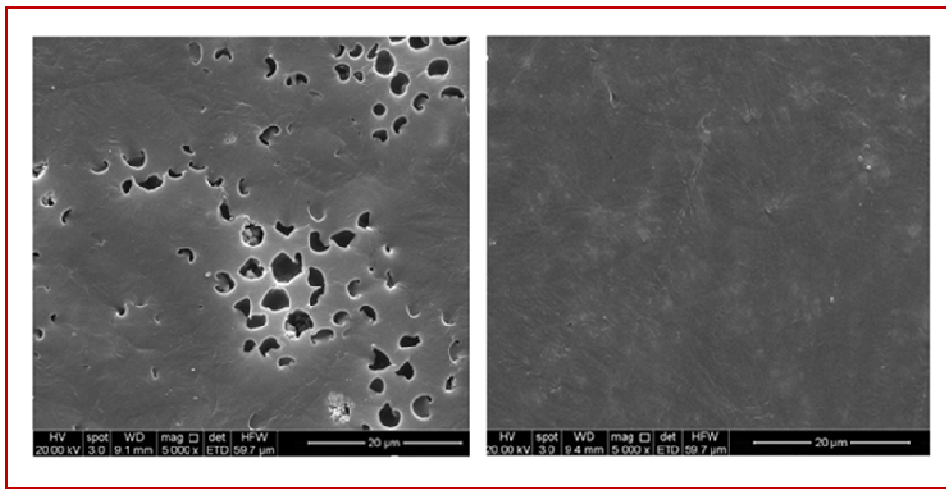


Figure 5: SEM image of (left) PCL/FeHA 90/10, (right) PCL/FeHA 80/20 nanocomposites.

SEM/EDS analysis (Figure 6) has allowed to verify that FeHA is characterized by a (Fe–Ca)/P molar ratio very similar to the theoretical ratio ($\text{Ca/P} = 1.67$).

With regard to the nanoparticle distribution, all the nanocomposite substrates have shown that MNPs and aggregates are uniformly distributed in the matrix.

Just as an example, the EDS images of the PCL/FeHA 80/20 nanocomposite, as well as the SEM–EDS P-, Ca-, and Fe-mapping photographs are presented in figure 6.

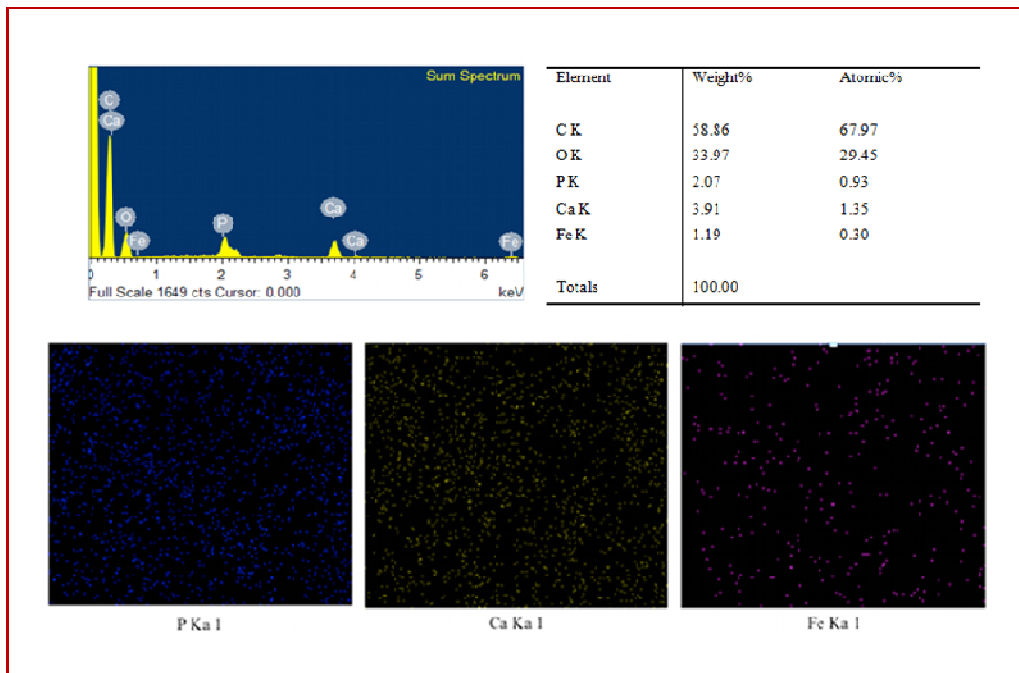


Figure 6: (up) EDS analysis, (down) SEM-EDS P-, Ca- and Fe-mapping photographs of PCL/FeHA 80/20 nanocomposite.

Micro-CT analysis has allowed for obtaining 3D reconstructions of the PCL and PCL/FeHA substrates, qualitatively evidencing the morphological features, the surface topography, and the presence of eventual defects (i.e., clusters, voids) (Figure 7).

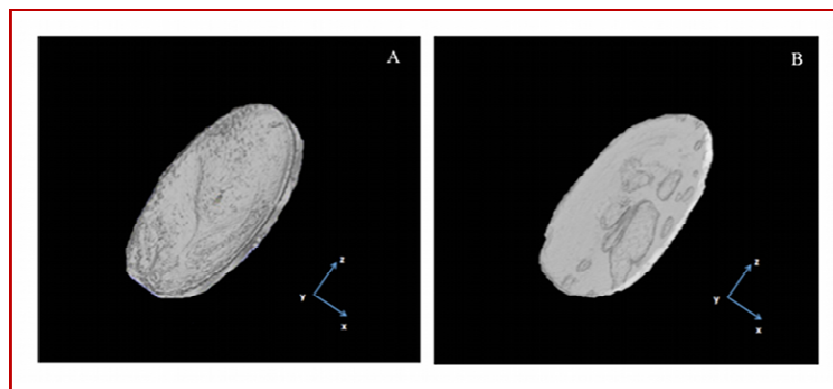


Figure 7: Results obtained from Micro-CT analysis: reconstruction of (A) PCL/FeHA 90/10, (B) 70/30 w/w, obtained by integrating SkyScan's software package, Image J software, Materialise Mimics and Rapidform 2006.

3.2.2 Contact Angle Measurements

The hydrophilicity of the manufactured PCL/FeHA substrates was examined by measuring the water contact angle and the results were compared to those obtained from the neat PCL ones (Figure 8, Table I).

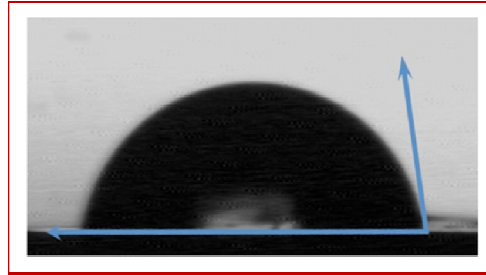


Figure 8: Typical image qualitatively representing the water contact angle.

Materials	Water Contact Angle, θ (deg)
PCL	81.4 ± 4.4
PCL/FeHA 90/10	75.7 ± 4.6
PCL/FeHA 80/20	74.8 ± 2.6
PCL/FeHA 70/30	64.9 ± 8.2

Table I: Water contact angles reported as mean value \pm standard deviation for PCL and PCL/FeHA substrates.

The water contact angle of PCL/FeHA nanocomposite substrates is lower than that of neat PCL ones, thus indicating that the presence of FeHA nanoparticles embedded into the polymeric matrix makes the surface more hydrophilic. In particular, the higher the amount of the FeHA nanoparticles, the lower is the water contact angle; its values basically span from 81.4° for PCL substrates to 64.9° for PCL/FeHA 70/30 w/w.

All of the above mentioned results might be ascribed to the synergetic contribution of both surface chemistry and topography that can be clearly varied by including the FeHA nanoparticles. However, it is well known that PCL is a hydrophobic polymer and the water contact angle measured for PCL substrates should be greater than 90° . In contrast to this, with regard to PCL

substrates, Table I reports a water contact angle of $81.4 \pm 4.4^\circ$. This result may be related to the specific techniques (molding and solvent casting) used to manufacture the substrates that obviously alter the surface topography and roughness, thus reducing the value of the water contact angle.

3.2.3 Small Punch Tests

As a first step towards the mechanical characterization, the small punch test has been chosen to assess the performances of the proposed disk-shaped PCL/FeHA nanocomposite substrates as it may be considered as a reproducible miniature specimen test method. This test method has been already taken into consideration to evaluate the mechanical properties of retrieved acrylic bone cement, and PCL reinforced with sol-gel synthesized organic-inorganic hybrid fillers.^{11,15}

It is worth noting that this test does not yield a numerical value for the Young's modulus; however a numerical simulation of the small punch test setup using the finite element method (FEM) should be performed in order to find a precise correlation between the test results and the Young's modulus of the materials.¹² Results from small punch tests on PCL and PCL/FeHA substrates have shown load-displacement curves generally characterized by an initial linear trend, followed by a decrease of the curve slope until a maximum load is reached. Finally, it is well evident that a decrease of the load until failure has occurred for all specimens (Figure 9).

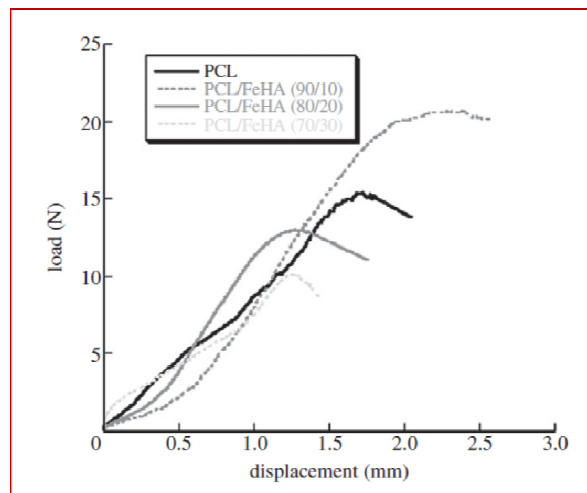


Figure 9: Load-displacement curves obtained from small punch tests performed on poly(ϵ -caprolactone) (PCL) reinforced with iron-doped hydroxyapatite (FeHA) nanoparticles.

Maximum load and displacement at maximum load obtained from PCL and PCL/FeHA substrates are reported as mean value \pm standard deviation in Table II.

Materials	Maximum load (N)	Displacement at maximum load (mm)
PCL	15.30 \pm 1.30	1.60 \pm 0.20
PCL/FeHA 90/10	22.51 \pm 0.60	2.40 \pm 0.45
PCL/FeHA 80/20	12.19 \pm 0.57	1.32 \pm 0.12
PCL/FeHA 70/30	10.27 \pm 1.05	1.12 \pm 0.18

Table II: Results from small punch tests: maximum load and displacement at maximum load are reported as mean value \pm standard deviation.

Figure 9 and Table II highlight that the inclusion of 10% by weight of FeHA nanoparticles represents an effective reinforcement in terms of higher maximum load, providing mechanical performances that are better than those obtained for the neat PCL substrates and the other compositions of nanocomposite.

In particular, PCL/FeHA 90/10 w/w substrates have provided higher values of maximum load (22.51 \pm 0.60 N) and displacement at maximum load (2.40 \pm 0.45 mm) in comparison to neat PCL and other nanocomposites, thus resulting to be stronger but flexible and tough at the same time. However, it is worth noting that PCL substrates show values of maximum load (15.30 \pm 1.30 N) that are greater than those achieved by PCL/FeHA 80/20 and 70/30 w/w.

It is well known that weakness in the structure may be clearly due to discontinuities in the stress transfer and generation of stress concentration at the nanoparticle/matrix interface, which may be ascribed to the difference in ductility between the polymeric matrix and the inorganic nanofillers.

These experiments suggest that beyond a specific limit of nanoparticle amount, by further increasing the nanoparticle concentration, the mechanical performances of the nanocomposite substrates decrease since the nanoparticles act as “weak points” instead of reinforcement for the polymeric matrix.

3.2.4 Magnetic Analysis

The approach to design magnetic scaffolds for tissue engineering clearly rises from the challenging idea of guiding tissue regeneration process benefiting from a magnetic field.

As already specified, even though, the magnetic guiding process is already well known in nanomedicine (i.e., drug delivery, hyperthermia treatment of tumors), this concept is not yet employed in the field of scaffolds for tissue engineering. For this reason, as a first step, preliminary magnetic measurements have been carried out in terms of magnetization and susceptibility. In particular, three different measurement modes have been used to perform a magnetic characterization of the samples: field dependence of the magnetization $M(H, T)$ at body temperature ($T = 310\text{ K}$), temperature dependence of the magnetization in a small field ($H = 50\text{ Oe}$), and frequency dependence of the magnetic susceptibility $\chi(f)$ at $T = 310\text{ K}$. The results of these measurements confirmed the superparamagnetic character of the FeHA nanoparticles in the samples, indicated by a very low coercive field, a defined saturation magnetization, and a strong history dependence in temperature sweeps.

The results of the field-dependent magnetization measurements are depicted in figure 10.

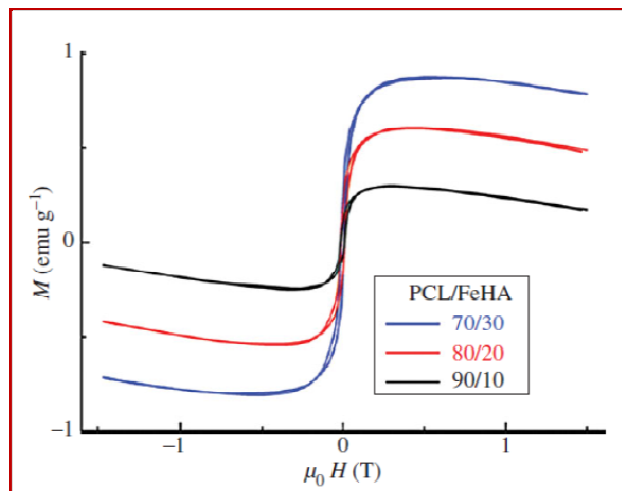


Figure 10: Field-dependent magnetization of the three PCL/FeHA compositions investigated in the article. Each curve was taken at $T = 310\text{ K}$ (human body temperature). The coercive field is approximately 15 Oe, independent of the composition.

Independent of their FeHA content, the coercive field of all samples took a value of 15 Oe at body temperature, indicating vanishingly small interactions between the MNPs. The saturation magnetization values were found to be strictly proportional to the FeHA content. The magnetization curves are superimposed by a diamagnetic background originating from the PCL and FeHA content of the samples. This diamagnetic background can be roughly ascribed to a value of χ_{PCL} which is equal to $-1.46 \cdot 10^{-7} \text{ emu} / (\text{g}\% w_{PCL} \text{Oe})$ at 310 K.

The temperature dependence of the magnetization of one sample (PCL/FeHA 90/10) is shown in figure 11.

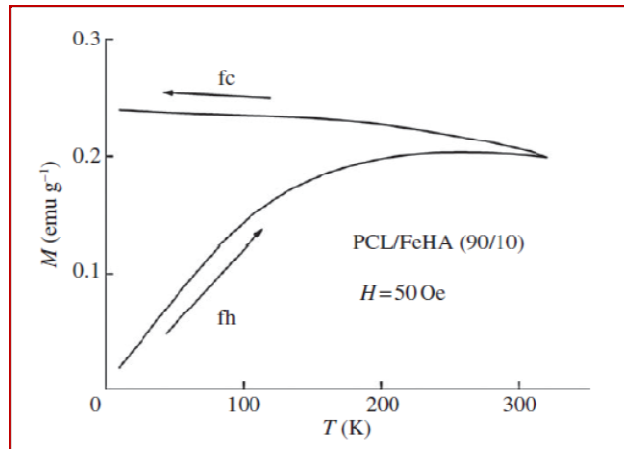


Figure 11: Temperature dependence of the magnetization of the PCL/FeHA 90/10 sample. The sample was cooled in a zero field, then heated in a small field (50 Oe – fh branch) and again cooled in field (fc branch).

The results for the other compositions investigated in this research are similar to those given in the figure 11. The data were taken in a zero-field cooling – field heating – field cooling sequence in order to trace the polarization process (see Appendix). Within the temperature range shown, the field-heating and field-cooling curves do not seem to overlap, making it difficult to determine the blocking temperature unambiguously. From the temperature value at the maximum of the field-heated curve we derive an effective MNP-core diameter of $d_{eff} = 13 \text{ nm}$.¹⁶

The frequency-dependent susceptibility is an important indicator for the applicability of these materials to hyperthermia treatment methods. All the measurements discussed here have been taken

at a background field much smaller than 5 Oe. The results for the sample of PCL/FeHA 90/10 are shown in figure 12, again representing the other compositions that showed similar results.

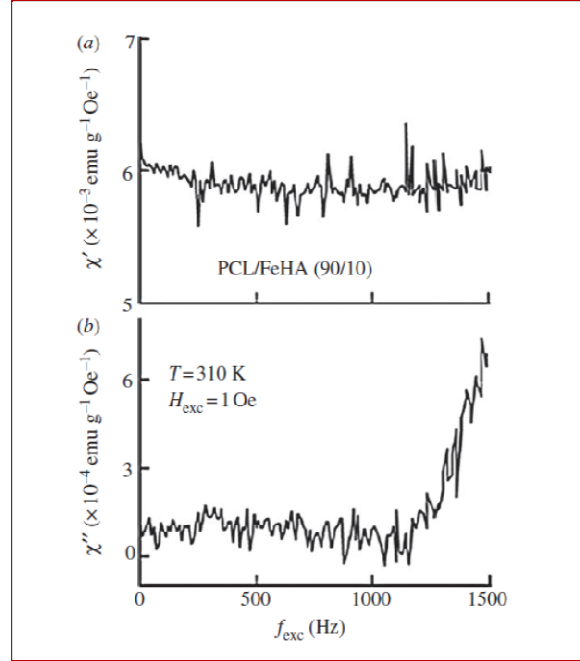


Figure 12: Frequency dependence of the real (a) and imaginary (b) part of the magnetic susceptibility of PCL/FeHA 90/10 nanocomposite substrate.

At a fixed excitation and 310 K, $\chi'(f)$, which is the real part of $\chi(f)$, takes a constant value of $6 \cdot 10^{-3}$ emu/(g Oe) within the frequency range $0 \text{ Hz} < f < 1500 \text{ Hz}$, increasing linearly with the excitation amplitude. The imaginary part $\chi''(f)$ is approximately zero below $f = 1200 \text{ Hz}$. For frequencies above 1200 Hz, $\chi''(f)$ increases approximately linearly with frequency, reaching a value of $7 \cdot 10^{-4}$ emu/(g Oe) at 1500 Hz.

This increase of $\chi''(f)$ can be interpreted as an onset of a maximum of dissipation, which is due to thermally agitated directional fluctuations rather than to ferromagnetic resonance.¹⁷

Regarding the heating properties, figure 13 shows the temperature increase of the PCL/FeHA magnetic composites under an alternating magnetic field of 27 mT at a frequency of $f=260 \text{ kHz}$.

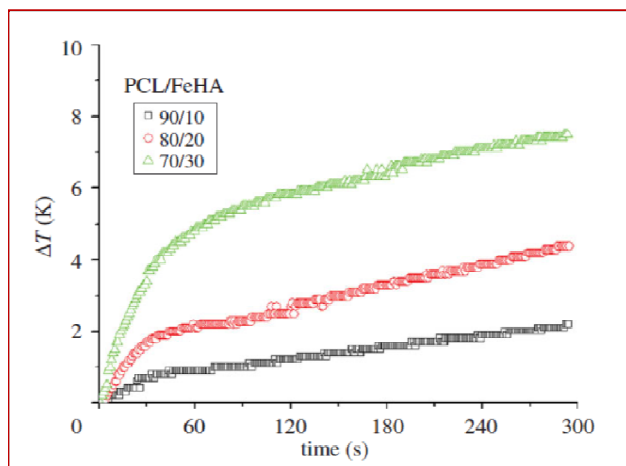


Figure 13: Hyperthermia curves of the PCL/FeHA magnetic substrates under application of a RF magnetic field of $f=260$ kHz and $H=27$ mT, suitable for *in vivo* applications.

Basically, it can be observed that all the samples show a magnetically induced thermal response, due to the energy released through the Néel relaxation process, which is the only mechanism contributing for superparamagnetic nanoparticles embedded in a rigid solid. Significant temperature increases between 2 K and 10 K were achieved after 5 minutes of exposure to an external magnetic field for all the PCL/FeHA compositions. A progressive increase in the heating rate is observed as the amount of magnetic FeHA nanoparticles increases in the composite.

These results provide PCL/FeHA scaffolds with unique properties to be used in *in vivo* applications, since their functionality can be remotely fine-tuned by controlling both the amount of magnetic nanoparticle concentration and the time of the magnetic field exposure.

3.2.5 Biological Analysis

Cell Adhesion Study

The biocompatibility of the PCL/FeHA nanocomposite substrates has been studied *in vitro* by using hMSCs. The results of the *in vitro* study are reported in figures 14-16. Firstly, CLSM analyses performed on all the cell-constructs have qualitatively provided interesting results in terms of hMSCs adhesion and spreading at 7, 14 and 21 days after seeding (Figure 14).

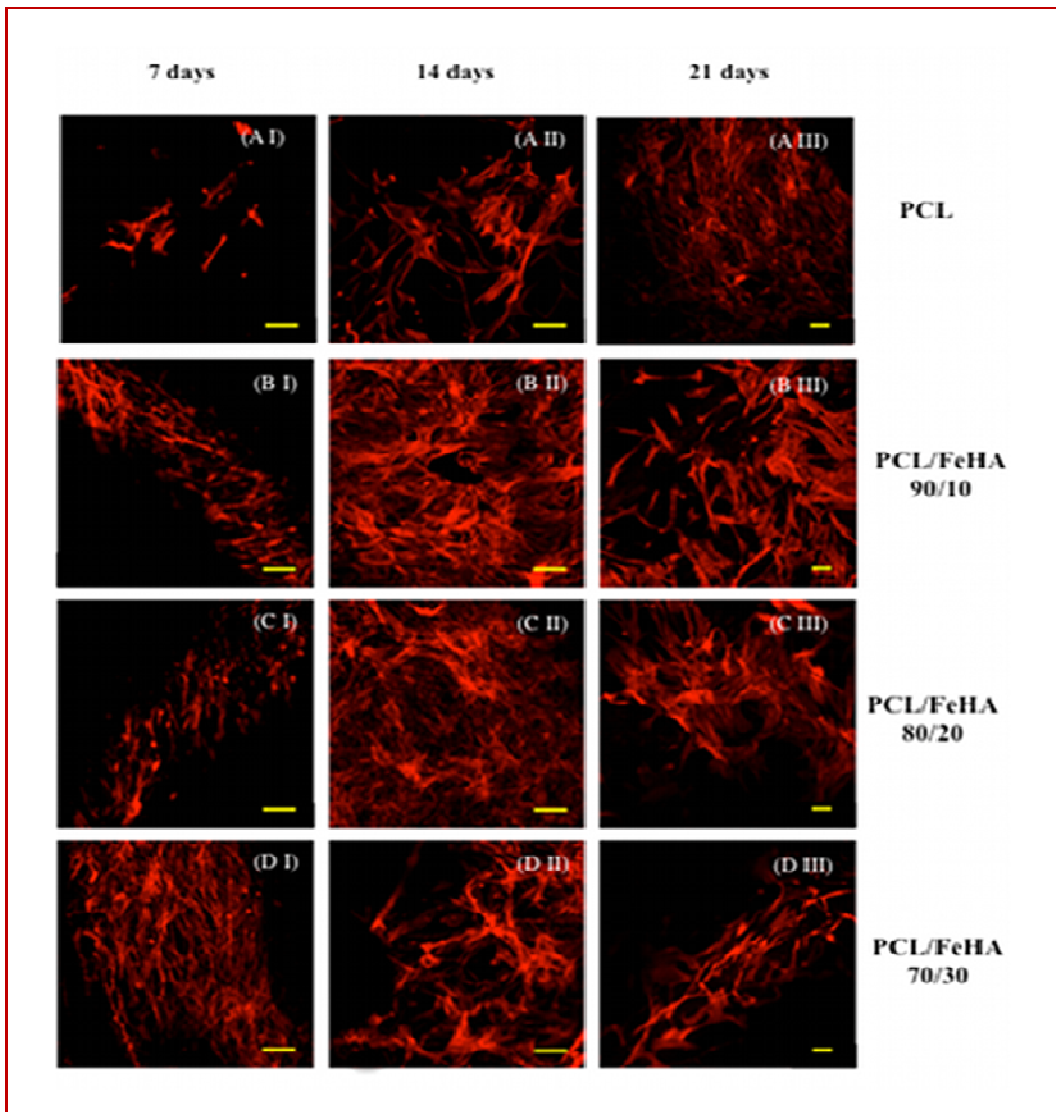


Figure 14: Cell adhesion study: CLSM images at different times after cell seeding. A I, B I, C I and D I represent PCL, PCL/FeHA 90/10, 80/20 and 70/30 at 7 days after cell seeding. A II, B II, C II and D II are PCL, PCL/FeHA 90/10, 80/20 and 70/30 at 14 days after cell seeding. A III, B III, C III and D III represent PCL, PCL/FeHA 90/10, 80/20 and 70/30 at 21 days after cell seeding. Scale Bar: 100 μ m.

Figure 14 highlights the cell cytoskeleton organization over the time. In particular, hMSCs were well spread and better adhered on PCL/FeHA nanocomposites in comparison to cells seeded on PCL substrates, as qualitatively suggested by actin-cytoskeleton staining. In addition, an increase in the adhered number of hMSCs is well evident in the case of FeHA nanocomposites.

Alamar Blue™ assay

The Alamar Blue™ assay has provided information on cell proliferation and viability over the culture time through a quantitative evaluation of the percentage of Alamar Blue™ reduction for the substrates. The results are graphically shown in figure 15 where they are reported as mean value and error bars represent standard deviation.

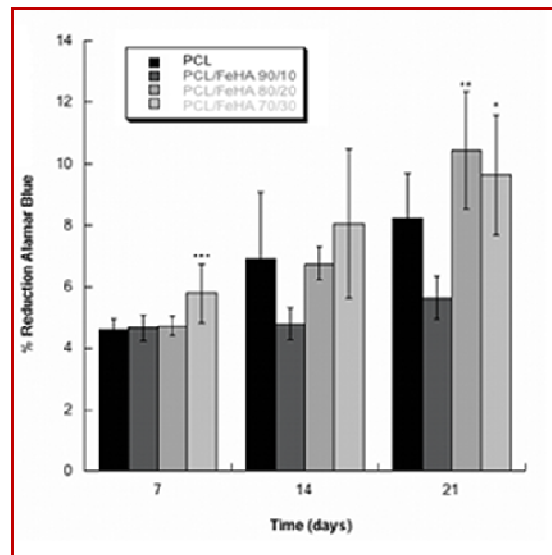


Figure 15: Results obtained from Alamar Blue™ assay at 7, 14 and 21 days after seeding. Error bar represents the standard deviation. * $p < 0.05$; ** $p < 0.01$; *** $p < 0.001$, indicate statistically significant differences between nanocomposite and poly(ϵ -caprolactone) substrates, at the same time from cell seeding (one-way ANOVA followed by Tukey post hoc test).

The results obtained from the Alamar Blue™ assay have evidenced that hMSCs were viable on both PCL and PCL/FeHA substrates over time, as the percentage of Alamar Blue™ reduction increases with time. In particular, even though at 7 days after seeding there is no great difference among the PCL and PCL/FeHA substrates, some differences may be noticed at 14 and 21 days.

In particular, PCL/FeHA 70/30 and 80/20 w/w substrates have provided higher values of the percentage of Alamar Blue™ reduction at 21 days after seeding.

It seems that especially the results obtained at 21 days are correlated with the values of water contact angle. The inclusion of FeHA nanoparticles intrinsically enhances the hydrophilicity and modifies the substrate topography, thus favoring cell viability and proliferation.

ALP/DNA assay

As previously stated, ALP activity was measured using a specific biochemical assay. The osteogenic differentiation of the hMSCs cells has been assessed by normalized ALP activity and reported as mean value and standard deviation over time (Figure 16).

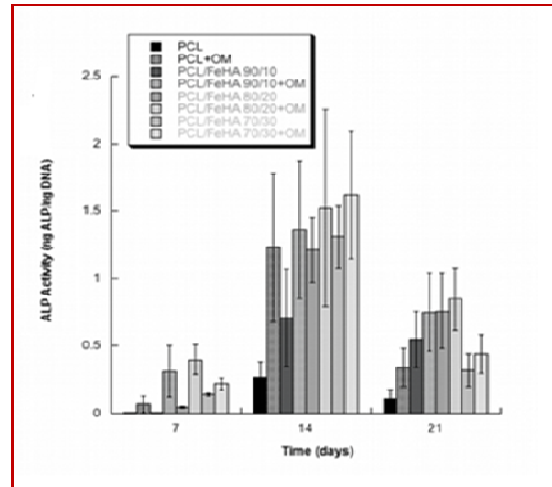


Figure 16: Results obtained from ALP/DNA assay at 7, 14 and 21 days after cell seeding. Error bar represents the standard deviation.

The significant increase of the ALP activity from day 7 to 14 clearly suggests that cells were induced to differentiate during this period, thus evidencing the ability of both polymeric and nanocomposite substrates to support the osteogenic differentiation of hMSCs. The decrease of the ALP activity from day 14 to 21 is also consistent with that reported for the MG63 cells seeded on hydroxyapatite/collagen nanocomposite sponges and ascribed to the expression of later-stage osteogenic markers and to the begin of calcium deposition.¹⁸

However, especially for PCL substrates, the effect of the osteogenic medium (OM) is well evident; ALP activity of the osteogenically-induced hMSCs results higher than that obtained from cultures under standard conditions. Furthermore, taking into account the values of ALP activity reported in figure 16, it may be noticed how, under standard culture conditions, the nanocomposite PCL/FeHA substrates seem to better promote the osteogenic differentiation than the PCL ones. These results

are also consistent with those previously obtained from quantitative biological analyses (CLSM analysis and Alamar BlueTM assay); stressing the importance of how the chemistry of FeHA nanoparticles and/or the different surface topography and roughness of the nanocomposites can enhance cell adhesion.

Conclusions

Nanocomposite substrates were firstly designed by embedding iron-doped hydroxyapatite nanoparticles into a poly(ϵ -caprolactone) matrix.

XRD analysis has been used as a tool to demonstrate that the process used to make the substrates does not affect the structure and crystallinity of the magnetic iron-doped hydroxyapatite, whilst the effect of nanoparticle inclusion on the mechanical performances of the substrates has been evaluated through small punch tests.

On the other hand, a magnetic characterization has been carried out to assess the magnetization as a function of field and temperature, as well as the frequency dependence of the susceptibility. In addition to the magnetic performances of the nanocomposites, the thermal activity obtained by magnetic hyperthermia experiments reveal this material to be extremely useful for remotely controlled *in vivo* applications.

The biological performances of the nanocomposite substrates have been properly evaluated through Alamar BlueTM and ALP/DNA measurements as well as through CLSM analysis. In particular, confocal laser scanning microscopy and Alamar BlueTM have provided qualitative and quantitative information on hMSC adhesion and viability/proliferation, respectively, whilst the ability of the nanocomposite substrates to support the osteogenic differentiation has been assessed through ALP/DNA assay. Furthermore, it is worth noting how the results obtained from biological analyses are correlated with the values of water contact angle. The present study may be considered as a first step of a future complex work that should be aimed by the design of 3D magnetic nanocomposite

scaffolds for bone tissue engineering, benefiting from the eventual effect of the magnetic field on the tissue regeneration process.

Prof. A. Tampieri from the Institute of Science and Technology for Ceramics, National Research Council, Faenza, Italy, is gratefully acknowledged for kindly providing FeHA nanoparticles.

Dr. M. Bañobre-López, dr. Y. Piñeiro-Redondo, prof. J. Rivas from Applied Physics Department, University of Santiago de Compostela, Santiago de Compostela, Spain and from International Iberian Nanotechnology Laboratory (INL), Braga Portugal, dr. M. Uhlarz, and prof. T. Herrmannsdörfer from Helmholtz-Zentrum Dresden-Rossendorf (HZDR), Dresden High Magnetic Field Laboratory (HLD), Dresden, Germany, Prof. V.A. Dediu from the Institute of Nanostructured Materials, National Research Council, Bologna, Italy, are gratefully acknowledged for their support and collaboration in the magnetic analysis of nanocomposite scaffolds.

References

1. Gloria A., Russo T., D'Amora U., Zeppetelli S., D'Alessandro T., Sandri M., Bañobre-López M., Piñeiro-Redondo Y., Uhlarz M., Tampieri A., Rivas J., Herrmannsdörfer T., Dediu V.A., Ambrosio L., De Santis R. *Magnetic poly(ϵ -caprolactone)/iron-doped hydroxyapatite nanocomposite substrates for advanced bone tissue engineering*. J. R. Soc. Interface. 80 (10): 1-11, 2013.
2. Singh N., Jenkins G.J.S., Asadi R., Doak S.H. *Potential toxicity of superparamagnetic iron oxide nanoparticles (SPION)*. Nano Reviews. 1: 53–8, 2010.
3. Lewinski N., Colvin V., Drezek R. *Cytotoxicity of nanoparticles*. Small. 4: 26–49, 2008.
4. Tampieri A., D'Alessandro T., Sandri M., Sprio S., Landi E., Bertinetti L., Panseri S., Peponi G., Goettlicher J., Bañobre-López M., Rivas J. *Intrinsic magnetism and hyperthermia in bioactive Fe-doped hydroxyapatite*. Acta Biomater. 8: 843-51, 2012.
5. Berry C.C., Curtis A.S.G. *Functionalisation of magnetic nanoparticles for applications in biomedicine*. J. Phys. D. Appl. Phys. 36: 198–206, 2003.
6. Pon-On W., Meejoo S., Tang I.M. *Incorporation of iron into nano hydroxyapatite particles synthesized by the microwave process*. Int. J. Nanosc. 6(1): 9–16, 2007.
7. Jiang M., Terra J., Rossi A.M., Morales M.A., Baggio Saitovitch E.M., Ellis D.E. *Fe²⁺/Fe³⁺ substitution in hydroxyapatite: Theory and experiment*. Phys. Rev. B. 66: 224107, 2002.
8. Landi E., Tampieri A., Mattioli-Belmonte M., Celotti G., Sandri M., Gigante A., Fava P., Biagini G. *Biomimetic-Mg- and Mg₂CO₃- substituted hydroxyapatites: synthesis characterization and in vitro behaviour*. J. Europ. Cer. Soc. 26: 2593-2601, 2006.
9. Barinov S.M., Rau J.V., Fadeeva I.V., Nunziante Cesaro S., Ferro D., Trionfetti G., Komlev V.S., Bibikov V.Y. *Carbonate loss from two magnesium-substituted carbonated apatites prepared by different synthesis techniques*. Mat. Res. Bull. 41: 485-494, 2006.
10. Gervaso F., Scalera F., Padmanabhan S.K., Sannino A., Licciulli A. *High-Performance Hydroxyapatite Scaffolds for Bone Tissue Engineering Applications*. Int. J. Appl. Ceram. Technol. 9 (3): 507–516, 2012.
11. Russo T., Gloria A., D'Antò V., D'Amora U., Ametrano G., Bollino F., De Santis R., Ausanio G., Catauro M., Rengo S., Ambrosio, L. *Poly(ϵ -caprolactone) reinforced with sol-gel synthesized organic-inorganic hybrid fillers as composite substrates for tissue engineering*. J. Appl. Biomater. Biomech. 8: 146-152, 2010.
12. De Santis R., Gloria A., Russo T., D'Amora U., D'Antò V., Bollino F., Catauro M., Mollica F., Rengo S., Ambrosio L. *Advanced Composites for Hard-Tissue Engineering Based on PCL/Organic-Inorganic Hybrid Fillers: From the Design of 2D Substrates to 3D Rapid Prototyped Scaffolds*. Pol. Comp. DOI 10.1002/pc.22446.

13. Nociari M.M., Shalev A., Benias P., Russo C. *A novel one-step, highly sensitive fluorometric assay to evaluate cell-mediated cytotoxicity*. J. Immunol. Meth. 213: 157-67, 1998.
14. Goegan P., Johnson G., Vincent R. *Effects of serum protein and colloid on the AlamarBlue™ assay in cell cultures*. Toxic. In Vitro. 9: 257-66, 1995.
15. Dunne N.J., Leonard D., Daly C., Buchanan F.J., Orr J.F. *Validation of the small punch test as a technique for characterizing the mechanical properties of acrylic bone cement*. Proc. Inst. Mech. Eng. Part H. 220: 11-21, 2006
16. Candela G.A., Haines R.A. *A method for determining the region of superparamagnetism*. Appl. Phys. Lett. 34: 868-870, 1979.
17. Brown W.R. Jr. *Thermal Fluctuations of a Single-Domain Particle*. Phys. Rev. 130: 1677-1686, 1963.
18. Yoshida T., Kikuchi M., Kyama Y., Takakuda K. *Osteogenic activity of MG63 cells on bone-like hydroxyapatite/collagen nanocomposite sponges*. J. Mater. Sci. Mater. Med. 4: 1263–1272, 2010.

Chapter 4

From the design of 2D substrates to 3D poly(ϵ -caprolactone)/iron-doped hydroxyapatite nanocomposite magnetic scaffolds

Preface

The aim of this step of the research was to develop and to study 3D rapid prototyped scaffolds consisting of a poly(ϵ -caprolactone) (PCL) matrix reinforced with iron-doped hydroxyapatite (FeHA) nanoparticles, benefiting from the previous experimental analyses performed on the 2D nanocomposite magnetic substrates.¹ The effects of the nanoparticle inclusion on the mechanical, magnetic and biological performances of the substrates were evaluated.¹ Results obtained from the above mentioned studies have allowed to select the polymer-to-nanoparticle weight ratio (w/w) showing the best compromise between mechanical, magnetic and biological properties. In particular a PCL/FeHA weight ratio (w/w) of 80/20 was used. In this study, the mechanical and biological performances of the proposed PCL/FeHA nanocomposite scaffolds were properly evaluated.

In particular, preliminary biological analyses have involved magnetic scaffolds and sinusoidal magnetic fields, in order to highlight the influence of a magnetic stimulation on cell adhesion and proliferation.

Further analyses, using magnetically-charged cells and magnetic scaffolds, have been performed, the aim being to assess if the application of a magnetic field at time of scaffold loading provides some benefits in terms of the efficiency of cell loading.

Finally, *in vivo* experiments and preliminary hystological analyses have been carried out.

4.1 Materials and Methods

4.1.1 Design and preparation of 3D PCL/FeHA nanocomposite scaffolds

As a first step toward the design of 3D nanocomposite magnetic scaffolds through the rapid prototyping technique, nanocomposite PCL/FeHA pellets were suitably prepared. Poly(ϵ -caprolactone) ($M_w = 65000$ - Sigma Aldrich St. Louis, MO) pellets were dissolved in tetrahydrofuran (THF) with stirring at room temperature. FeHA nanoparticles and, subsequently, ethanol were added to the PCL/THF solution during stirring. A PCL/FeHA weight ratio (w/w) of 80/20 was used.

An ultrasonic bath (Branson 1510 MT, Danbury CT) was employed to optimize the nanoparticle dispersion in the polymer solution. Homogenous paste was obtained and the solvent was then properly removed. Successively, nanocomposite pellets were made by machining.

3D well organized scaffolds were manufactured by processing PCL/FeHA pellets through a 3D fiber deposition technique.

In particular, nanocomposite scaffolds were built by extruding and depositing the fibers along specific directions according to the selected lay-down pattern. PCL/FeHA (80/20 w/w) pellets were initially placed in a stainless steel syringe and then heated to a temperature of 130-140°C using a heated cartridge unit placed on the mobile arm of a bioplotter dispensing machine (Envisiontec GmbH, Germany). Successively, an appropriate nitrogen pressure (i.e., 8.5-8.9 bar) was applied to the syringe through a cap. The nozzle used to extrude PCL/FeHA fibers presented an inner diameter of 600 μm . A deposition speed of 30-40 mm/min was generally used. Scaffolds were characterized by the fiber diameter (depending on the needle diameter and/or the deposition speed), the fiber spacing (strand distance, i.e. center-to-center distance) and layer thickness, which influence the overall pore size.

Block-shaped and cylindrical scaffolds were manufactured to highlight the feasibility of the process and to preliminarily study their mechanical and biological performances.

An image of a block-shaped PCL/FeHA magnetic scaffold is reported in figure 1.

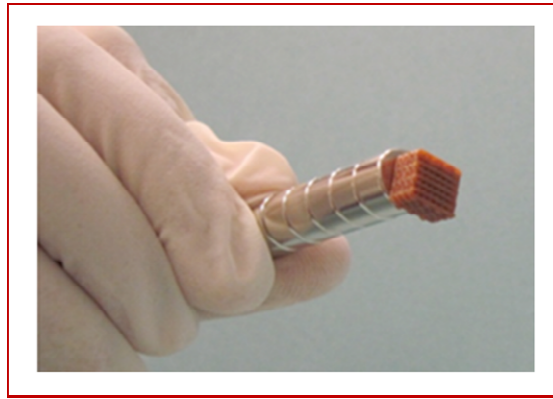


Figure 1: Image of a block-shaped 3D PCL/FeHA scaffold attracted to a neodymium magnet.

4.1.2 Morphological Analysis: SEM and TEM

In order to evaluate the morphology of the PCL/FeHA nanocomposite scaffolds, Scanning Electron Microscopy (SEM) was employed by using a FEI Quanta FEG 200 scanning electron microscope (The Netherlands).

On the other hand, Transmission Electron Microscopy (TEM), was employed to obtain an image strongly magnified related to the internal structure of the same, morphological (i.e. grain size, defects) and crystallographic information on PCL/FeHA nanocomposites, by using a FEI Tecnai G2 Spirit TWIN apparatus (The Netherlands).

4.1.3 Compression Tests on PCL/FeHA nanocomposite scaffolds

Compression tests were carried out on 3D cylindrical scaffolds characterized by a diameter (D_0) of 6.0 mm, a height (h_0) of 6.5 mm and a $0^\circ_2/90^\circ_2$ pattern. Scaffolds were characterized by a layer thickness of 390-400 μm , a fiber spacing of 1000 μm and a fiber diameter of 490-500 μm . All the tests were performed at a rate of 1 mm/min up to a strain value of 0.4 mm/mm, using an INSTRON 5566 testing machine (Bucks, UK). The stress ($\sigma=F/A_0$) was defined as the ratio between the force

(F) measured by the load cell and the apparent cross-section of the scaffold ($A_0 = \pi D_0^2/4$). The strain ($\varepsilon = \Delta h/h_0$) was evaluated as the ratio between the scaffold height variation (Δh) and the initial height (h_0).

4.1.4 Biological Analyses

4.1.4.1 The effect of a sinusoidal magnetic field on cell adhesion and proliferation

Introduction

One of the promising challenges in tissue engineering approach is to provide living constructs that can integrate with the surrounding tissue. To overcome the limitations related to the static culture systems, such as limited diffusion and inhomogeneous cell-matrix distribution, scaffold and several bioreactors have been designed. As already explained in the Chapter 1, scaffold should possess a set of chemical, biochemical and morphological cues, in order to promote and to control specific events at the cellular and tissue levels. On the contrary, the ideal feature of a bioreactor is that it should supply suitable levels of oxygen, nutrients, cytokines, growth factors, and mechanical stimulation to populate the volume of the scaffold with cells and their extracellular matrix.

A valuable candidate for tissue engineering applications should be a 3D rapid prototyped magnetic scaffold. It should satisfy all the above requirements. It will provide a morphologically controlled and tailored structure with interconnected pores of specific scale. Furthermore, a superparamagnetic (see Appendix) scaffold should be used also as its own bioreactor. The possibility to magnetically switch-on/switch-off the scaffold should be used at the same time for delivering biofactors, such as angiogenic ones, and stem cells, and for stimulating cells to adhere, proliferate and differentiate.

In order to better understand the possible range of biomedical applications of magnetic devices and their potentials, the effects of magnetic fields on human tissues need to be well investigated.

The influence of static or variable magnetic fields on biological systems has become a topic of considerable interest.

In the literature, many works aimed to investigate the influence of static magnetic field on biological systems. Static Moderate-intensity Field (SMFs) (1 mT - 1 T) are capable of affecting a number of biological phenomena such as cell proliferation,^{2,3} migration^{2,4} and orientation.^{2,5}

It has been demonstrated that SMFs have no lethal effect on cell growth and the cells have the ability to survive under normal growing conditions.⁶⁻⁸ SMFs can prevent decrease in bone mineral density,^{2,9} and promote the healing of bone fractures.^{2,10,11} Using an electromagnetic bioreactor (magnetic field intensity, 2 mT; frequency, 75 Hz), Fassina L. et al. (2006) investigated the effect of the electromagnetic stimulation on proliferation and calcified matrix production of a human osteogenic sarcoma cell line (SAOS-2); cell proliferation was twice as high whilst expression of decorin, osteocalcin, osteopontin, type I collagen, and type III collagen was greater and calcium deposition was five times as great as under static conditions without electromagnetic stimulation.¹²

Chiu K.H. et al. (2007) studied the differentiative effect of osteoblasts after treatment with a static magnetic field (0.4 T for 6 hours).¹³ The authors highlighted that during SMF stimulation, the cellular membrane is assumed to be the target. Phospholipids can be oriented by SMF, resulting in an over-deformation of the cellular membrane. SMF affects osteoblastic maturation by increasing the membrane rigidity, reducing its fluidity and the proliferation-promoting effects of growth factors at the membrane domain. Consequently, they observed an increase in the Alkaline Phosphatase (ALP) activity and a change in cell morphology.¹³ Feng S.W. et al. (2010) demonstrated a similar effect. In particular, they studied the influence of static magnetic field on osteoblast cells grown on poly(L-lactide) (PLLA) scaffolds. The results of their study suggested that human osteosarcoma cells (MG63) seeded on PLLA scaffolds and treated with SMF had a more differentiated phenotype.¹⁴

The effect of SMFs on cell morphology has been evaluated, showing that their effect depends on cell type and field strength.

Along these lines, the work of Sato K. et al. (1992) shows that the application of a static magnetic field of 1.5 T for 96 h on “immortal” cervical cancer cells (HeLa) did not produce significant

changes in cell shape,¹⁵ in contrast to the results obtained from the investigation of Pacini S. et al. (1999) who reported dramatic changes in the morphology of human neural cells derived from human olfactory epithelium (FNC-B4) after exposure to a magnetic resonance tomography.¹⁶

Pacini S. et al. (2003) reported an alteration of cell morphology of human skin fibroblasts associated with a decrease in the expression of glycoconjugate sugar residues when cells were exposed to a magnetic field of 0.2 T.¹⁷

Other studies have suggested that static magnetic fields have a detrimental effect on cell proliferation.¹⁸ Specifically, Cunha C. et al. (2012) analyzed for the first time the effect of a moderate intensity static magnetic field (320 mT) on MG-63 human osteoblast cells seeded *in vitro* on magnetic scaffolds. The application of a SMF, either continuously or applied for 1 h per day, resulted in a negative effect on cell proliferation and osteocalcin secretion.

However, the effect was not correlated with an increase in cellular apoptosis, stress or disruption of membrane integrity and morphological features and gene expression resulted unaltered.¹⁸

Regarding the application of variable magnetic fields, several studies have shown that continuous and prolonged exposure of cells to magnetic fields modify cell physiological parameters such as proliferation, synthesis and secretion of growth factors.^{6,19-21} These physiological changes depend largely on the physical properties of electromagnetic fields such as waveform and frequency, while the applied electromagnetic field dose is a function of field strength and duration of exposure.^{6,22}

It was found that application of Extremely Low Frequency (ELF) magnetic fields demonstrates advantages for *in vitro* generation of osteogenic tissue,^{23,24} stimulates angiogenesis and osteogenic precursor proliferation, and can also promote bone formation within suitable matrices.²⁴

Among the first published studies, Liboff A.R. et al. (1984) assessed the influence of a sinusoidal magnetic field with frequency of 76 Hz and intensity of 0.16 μ T on the process of fibroblast proliferation. The authors highlighted a positive effect due to the application of the field during the proliferation process.²⁵

De Mattei M. et al. (1999) evaluated the effect of a pulsed electromagnetic field with frequency of 75 Hz and 1.3 ms pulses on the proliferation process of different cell lines, showing that the magnetic field favors cell proliferation.²⁶

P. et al. (2002) analyzed the effect of a magnetic field of 7mT and 15 Hz on the proliferation of murine calvarial cells (MC3T3-E1), observing an increase in the proliferation process after constant exposure.²⁷

Furthermore, Chang W.H.S. et al. (2004), reported the effect of a pulsed electromagnetic field with frequency of 15 Hz and magnetic field strength of 0.1 mT on primary cultures of mouse calvaria in the proliferation and differentiation processes, reporting that constant exposure of 8 h per day for 14 days accelerated the process of proliferation without altering cell differentiation.²⁸

Recently, Martino C.F. et al. (2008) evaluated the effect of a pulsed magnetic field of 20 G and 15 Hz on the growth of SAOS-2 cells. The results of their research suggest that the electromagnetic field does not alter cell growth during constant exposure to the field.²⁹

The aim of the present study was to preliminary investigate the effect of variable magnetic field on *in vitro* adhesion and proliferation of Human Mesenchymal Stem Cells (hMSCs) seeded on 3D fiber deposited superparamagnetic scaffolds.

In particular, it was decided to analyze the effect of a sinusoidal magnetic field with frequency of 70 Hz and intensity of 25-30 mT, a value that falls in a specific range (1 mT to 1 T) which was demonstrated to have particular implications in a number of biological phenomena.^{18,30,31}

3D well organized block-shaped PCL and PCL/FeHA 80/20 scaffolds (8 mm x 8 mm x 2 mm) with a 0°/90° lay-down pattern, a strand distance of 1 mm, a layer thickness of 390-400 μm and a fiber diameter of 500 μm, were manufactured through 3D fiber deposition technique.

Cell culture

Human mesenchymal stem cells (hMSCs; Clonetics, Italy), at the fourth passage, were cultured in α -modified Eagle's medium (α -MEM) (Bio-Whittaker, Belgium) containing 10% (v/v) fetal bovine serum, 100 U/mL penicillin and 0.1 mg/mL streptomycin (HyClone, UK), in a humidified atmosphere at 37°C and 5% CO₂. Scaffolds for cell-culture experiments were prepared for cell seeding by soaking first in 70% ethanol (1 h) and then in 1% antibiotic/antimycotic in phosphate-buffered saline (PBS) (2 h), and pre-wetted in medium (2 h). Cells (density 1.0*10⁴ cells/sample), resuspended in 1 mL of medium, were statically seeded onto the substrate.

Sinusoidal Magnetic Field - Exposure System

At 1 day from cell seeding, two different exposure conditions have been considered.

- Group 1: continuous exposure for 6 h per day.
- Group 2: 6 h per day distributed in 18 minute of exposure, followed by 54 minutes of *stasis*.

Cell-constructs placed in the same incubator not subjected to a magnetic stimulation were used as control. Figure 2 is a schematic representation of the exposure system used. The electromagnet was placed below the wells to expose the cultures to sinusoidal magnetic field. Two adjacent wells used for culture were set apart by more than 10 mm as the edge-to-edge distance, so that the mutual influence of the magnetic field would be excluded.

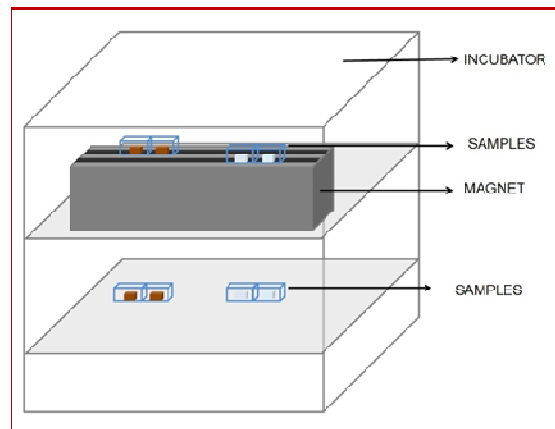


Figure 2: Schematic representation of the experimental setup used to perform biological analyses.

Alamar Blue™ assay

Cell viability and proliferation were evaluated by using the Alamar Blue™ assay. This is based on a redox reaction that occurs in the mitochondria of the cells; the colored product is transported out of the cell and can be measured spectrophotometrically.

After 1, 4, 7, 14, 21, 28, 35 days from cell seeding, the cell-constructs were rinsed with PBS (Sigma Aldrich, Italy), and for each sample, 200 µl of Dulbecco's modified Eagle's medium. (DMEM) without Phenol Red (HyClone, UK) containing 10% (v/v) Alamar Blue™ (AbD Serotec Ltd, UK) was added, followed by incubation in 5% CO₂ diluted atmosphere for 4 hours at 37°C.

One hundred microliters of the solution was subsequently removed from the wells and transferred to a new 96-well plate. The optical density was immediately measured with a spectrophotometer (Sunrise; Tecan, Männedorf, Zurich, Switzerland) at wavelengths of 570 and 595 nm. The number of viable cells correlates with the magnitude of dye reduction and is expressed as a percentage of Alamar Blue™ reduction, according to the manufacturer's protocol. Each experiment was repeated at least 3 times in triplicate.

Scanning Electron Microscopy (SEM)

In order to evaluate morphological features, cell adhesion and shape, scanning electron microscopy was performed through a FEI Quanta FEG 200 scanning electron microscope (The Netherlands).

The culture media was removed and the samples were rinsed three times with PBS. Then, cell-constructs were fixed in 2.5% glutaraldehyde (pH 7.4) (Sigma Aldrich, Italy) for 20 min at room temperature. The samples were washed and dehydrated in an ethanol series (70, 80, 90, 95, and 100% v/v), dried air, gold sputtered and analyzed by SEM.

4.1.4.2 Magnetically-charged cells and magnetic scaffolds: Scaffold-cell loading

Introduction

Cell labeling with magnetic nanoparticles is attracting growing interest, both in the field of magnetic resonance imaging and cell therapy.³²⁻³⁴

Recently, a great number of studies have looked at magnetic targeting of cells. *In vivo* studies have shown that magnetic labeling, particularly with superparamagnetic iron oxide nanoparticles (SPIONs), is relatively easy and safe.³⁵⁻³⁸

However, limited work has been done on using magnetic fields to guide SPION-labeled cells to specific targets.^{35,39}

This approach is a current method for monitoring cell migration in cell therapy trials.^{32,40,41}

Magnetically-labeled cells can be remotely manipulated by external magnetic fields for cell-sorting applications^{32,42} or to influence migration and organization of cells in engineered substrates or tissues.^{32,39,43-45} Tissue engineering and cellular therapy could both benefit from cellular magnetic targeting and control.^{32,46}

With the term “magnetic force-based tissue engineering”, Shimizu K. et al. (2005) have proposed an innovative cell-seeding methodology which could help to overcome the problems related to conventional cell seeding. In conventional static cell seeding, the cell suspension is seeded into small scaffolds using small volumes of highly concentrated cell suspension.⁴⁷ The inevitable problem is that the seeded cell suspension flows away with the medium and few cells remain in the scaffolds. If magnetically-labeled cells are used, magnetic forces could attract and prevent them from flowing away, thus allowing for the efficiency of cell seeding.

Benefiting from the above reported studies, the main driving idea of this work has been the design of a 3D rapid prototyped magnetic scaffold, the aim being to enhance the cell-seeding process.

A superparamagnetic scaffold should be able to attract and take up magnetically-charged cells via a driving magnetic force when it is necessary because it may be magnetically “turned off” upon removal of the magnetic field.

In particular, the efficiency of human breast cancer cell loading has been analyzed. Four-layer cylindrical PCL/FeHA 80/20 scaffolds were designed in order to optimize cell-assay in 96-multi-well-plate. In order to optimize pore size, 3D fiber deposited scaffolds with a $0^{\circ}_2/90^{\circ}_2$ lay-down pattern, a fiber diameter of $500\ \mu\text{m}$ and a layer thickness of $390\text{-}400\ \mu\text{m}$, were characterized by a three type of architectures (Figure 3):

- Group A - PCL/FeHA 80/20, 4 layers, strand distance $1835\ \mu\text{m}$;
- Group B - PCL/FeHA 80/20 4 layers, strand distance $1375\ \mu\text{m}$;
- Group C - PCL/FeHA 2 layers with a strand distance of $1835\ \mu\text{m}$, 2 layers with a strand distance of $1375\ \mu\text{m}$.

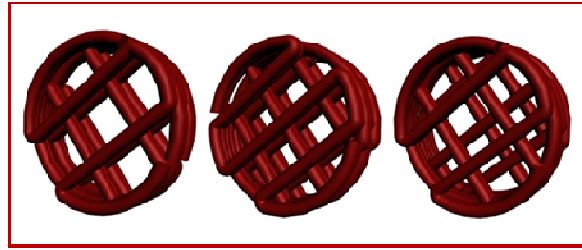


Figure 3: Different architectures of 3D fiber deposited scaffolds with a $0^{\circ}_2/90^{\circ}_2$ lay-down pattern, a fiber diameter of $500\ \mu\text{m}$, a layer thickness of $390\text{-}400\ \mu\text{m}$ and characterized by: (left) a strand distance of $1835\ \mu\text{m}$, (central) a strand distance of $1375\ \mu\text{m}$ and (right) 2 layers with a strand distance of $1835\ \mu\text{m}$, 2 layers with a strand distance of $1375\ \mu\text{m}$.

Cell Culture

Human breast cancer (hBrCa) cells, isolated from a primary tumor, were used.

hBrCa cells display cell-surface adhesion molecules, such as the $\alpha_v\beta_3$ integrin, which bind to bone matrix proteins. There are striking similarities between breast and bone *stroma*, which may contribute to the ability of hBrCa cells to survive and proliferate in bone. The stromal matrix of both tissues is rich in collagen type-I, osteopontin, laminin, and fibronectin.^{48,49}

Briefly, hBrCas (1.0×10^5 cells) were seeded into a 60 mm cell culture dish. After 24 h of incubation, in order to permit internalization of the nanoparticles, the medium was replaced with

medium containing SPIONs and the cells were reincubated. hBrCas avidly internalized magnetic nanoparticles (MNPs), thus obtaining magnetically-charged hBrCas.

Magnetically-charged hBrCas were loaded on 3D well-organized scaffolds by applying or not a magnetic field and by changing culture medium 24 h after cell seeding. Furthermore, before first change of medium, scaffold loading time was 24 h.

A magnetic field was applied for 1 h, and then for 4 h or 24 h of the loading period; the results were clearly compared with a negative control in which no magnetic field was applied.

The assay readout was the cell number measured as DNA content. Standard plots used as internal controls allowed DNA content to be reported in terms of cell numbers. Measurements were made at least in triplicate for each treatment.

At 24 h after seeding, loaded scaffolds were transferred to fresh wells, and the cells present in the scaffold and those not associated with the scaffold were assayed.

The fresh wells were round-bottomed, to minimize well contact with the scaffold, and so prevent cell outgrowth from the scaffold onto the well surface.

Thereafter, the cell-based assay was run for 72 h. At 72 h, the scaffold was again transferred to a fresh well, and the cells present in the scaffold as well as those remaining in the previous well were assayed.

4.2 *In vivo* experiments and histological analysis

PCL and PCL/FeHA 80/20 cylindrical scaffolds were successfully rapid prototyped for *in vivo* experiments into rabbits. Scaffold design was developed according to a large bone defect. Cylindrical scaffolds (diameter of 6.0 mm and a height of 8 mm) with a lay-down pattern of $0^{\circ}/90^{\circ}_2$ and a layer thickness of 390-400 μm were built. The fiber spacing was set to 1835 μm and the fibers were characterized by a diameter of 490-500 μm (Figure 4).

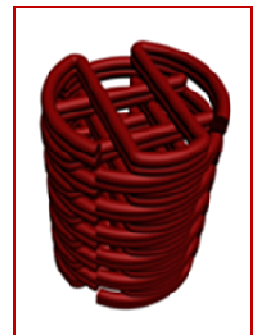


Figure 4: Scaffold for *in vivo* analysis.

The study was performed in accordance with EC guidelines (EC Council Directive 86/609, 1986) and the Italian legislation on animal experimentation (Decreto L.vo 116/92). The research protocol on animals has been approved by the Ethical Committee of Rizzoli Orthopaedic Institute and by the responsible public authorities. Six male rabbits (*Oryctolagus cuniculus*, Charles River, Lecco, Italy), 2.4 ± 0.2 kg body weight, were housed at a controlled temperature of $22 \pm 1^\circ\text{C}$ and relative humidity of $55 \pm 5\%$ in single boxes and fed a standard diet (Mucedola, Milano, Italy) with filtered tap water *ad libitum*. After quarantine of at least 10 days, the animals were fasted for 24 h before surgery. The animals were subjected to surgery to implant the scaffolds at the distal femoral epiphysis under general *anaesthesia* and in aseptic conditions. After having shaved and disinfected the posterior legs, the animals underwent a lateral longitudinal incision of lateral femoral condyle. Femoral lateral condyle trabecular bone was cross-sectionally drilled at low speed and a profuse irrigation with cold sterile 0.9% NaCl solution was maintained throughout the process to prevent the risk of bone necrosis. A critical bone defect of 6.00 mm in diameter and 8.00 mm in depth was made in each lateral femoral condyle. All six animals were subjected to the implantation of one PCL/FeHA scaffold and one PCL scaffold was implanted in the contralateral condyle as a control group. Scaffolds were sterilized by 25 kGy γ -ray radiation. Finally, the skin was sutured. General anaesthesia was induced by an intramuscular injection of 44 mg/kg ketamine (Imalgene 1000, Merial Italia S.p.A, Milan, Italy) and 3 mg/kg xylazine (Rompun, Bayer SpA, Milano, Italy) under assisted ventilation with $\text{O}_2/\text{N}_2\text{O}$ (1-0.4 l/min) mixture and 2.5% isofluorane (Forane, Abbot SpA, Latina, Italy). Post-operatively, antibiotics and analgesics were administered: 0.6 mL/kg flumequil (Flumexil, (FATRO S.p.A., Bologna, Italy) and 0.1 mL/kg per day metamizole sodium (Farmolisina, Ceva Vetem SpA, Monza-Brianza, Italy).

At 4 weeks after surgery, the animals were pharmacologically euthanized with intravenous administration of Tanax (Hoechst, Frankfurt am Main, Germany), under general anaesthesia. The operated bone segments were excised and stripped of soft tissue and the presence of haematomas, oedema, and inflammatory tissue reactions were macroscopically evaluated. The bone segments

were fixed in 4% buffered paraformaldehyde for 24 h, dehydrated in a graded series of alcohol and finally embedded in a methylmethacrylate resin (Merck Schuchardt OHG, Hohenbrunn, Germany). Using a saw microtome (Leica SP1600, Leica Microsystems S.r.l., Italy), three consecutive central sections to the major axis of the implant for each bone segment were cut ($60 \pm 20 \mu\text{m}$) and polished (Struers Dap-7, Struers Tech A/S, Rodovre/Copenhagen, Denmark). Then, thinned sections ($30 \pm 10 \mu\text{m}$) were stained with Toluidine Blue, Acid Fucsin and Fast Green.

4.3 Results and Discussion

4.3.1 Morphological Analysis: SEM and TEM

Results obtained from SEM analyses (Figure 5) have allowed to highlight the well-organized structure (i.e. architecture, fiber spacing, effective fiber diameter) and to evaluate morphological features of the polymeric and nanocomposite scaffolds. In particular, PCL and PCL/FeHA fibers have a mean diameter of $500 \mu\text{m}$. It is worth noting that the nanocomposite magnetic surface is characterized by a greater roughness, due to the presence of FeHA nanoparticles, which has been shown to strongly affect cell behaviors. As already explained above, surface topography and chemistry play an important synergistic role in the process of cell-material interaction.

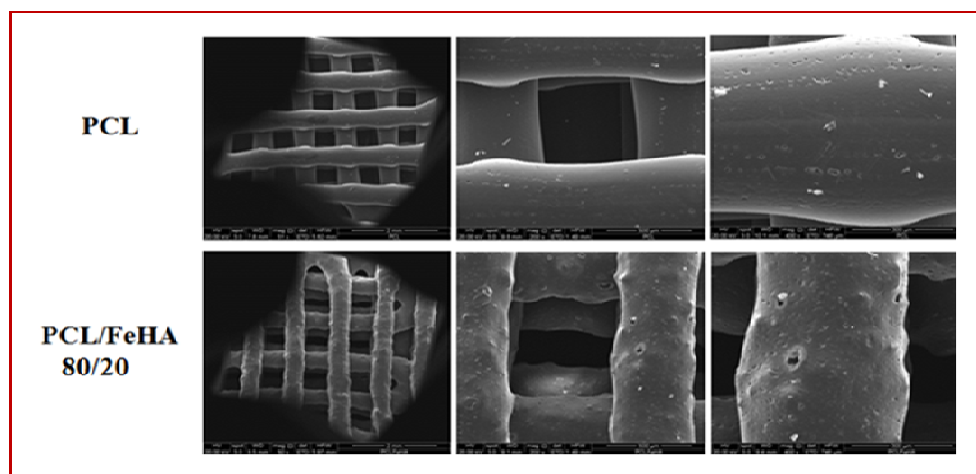


Figure 5: Different images of 3D PCL and PCL/FeHA nanocomposite scaffolds manufactured by 3D fiber deposition technique: (left) overall scaffold image, Scale Bar - 2 mm, (middle) Scale Bar - $500 \mu\text{m}$, (right) Scale Bar - $300 \mu\text{m}$.

TEM analysis (Figure 6) has allowed to confirm that MNPs and aggregates or clusters are uniformly and randomly distributed in the matrix. Furthermore, in comparison with TEM images obtained for nanocomposite magnetic substrates and those obtained for iron-doped hydroxyapatite nanoparticles,⁵⁰ it is worth noting that morphological features, size and shape of nanoparticles in the PCL matrix, are not influenced by the synthesis process used to obtain such PCL/FeHA scaffolds.

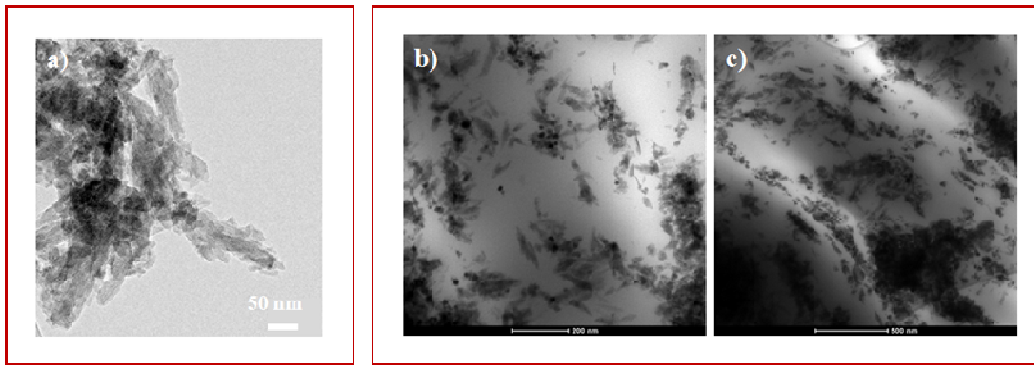


Figure 6: TEM images of: (a) FeHA nanoparticles Scale Bar - 50 nm,⁵⁰ b) PCL/FeHA 80/20 nanocomposite - Scale Bar - 200 nm, c) PCL/FeHA 80/20 nanocomposite - Scale Bar - 500 nm.

4.3.2 Compression Tests on PCL/FeHA nanocomposite scaffolds

Results from compression tests have highlighted that the 3D PCL/FeHA scaffolds show a mechanical behavior very similar to that of 3D PCL/Fe₃O₄ ones even if the polymer-to-particle weight ratio is greater (Figure 7).

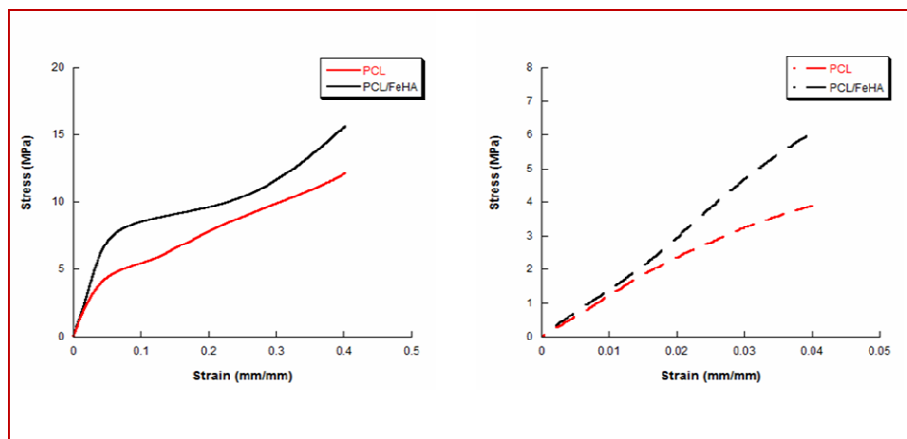


Figure 7: Typical stress-strain curves obtained from compression tests performed on PCL and PCL/FeHA cylindrical scaffolds: left) Stress-strain curves reported up to a strain level of 0.4 mm/mm; right) Stress-strain curves reported up to a strain level of 0.04 mm/mm in order to better highlight the initial mechanical behavior.

Compressive modulus and maximum stress (at a strain level of 0.4 mm/mm) have been reported in Table I.

Scaffolds	Compressive modulus, E	Maximum Stress, σ_{max}
	(MPa)	(MPa)
PCL	92.1 ± 19.1	12.1 ± 1.9
PCL/FeHA	139.2 ± 21.8	15.6 ± 2.7

Table I: Compressive modulus (E) and maximum stress (σ_{max}) at a strain level of 0.4 mm/mm reported as mean value \pm standard deviation.

4.3.3 Biological Analyses

4.3.3.1 The effect of a sinusoidal magnetic field on cell adhesion and proliferation

Results obtained from Alamar Blue™ assay performed on Group 1 (frequency 70 Hz, intensity 30 mT for 6 h per day) and control samples have shown that prolonged exposure time to a sinusoidal magnetic field seems to negatively affect cell viability (Figure 8). In particular, not magnetically stimulated PCL and PCL/FeHA scaffolds have provided generally higher values of the percentage of Alamar Blue™ reduction and a maximum viability peak at 14 days after cell seeding. On the contrary, magnetically stimulated PCL and PCL/FeHA structures have provided lower values of percentage of Alamar Blue™ reduction and a maximum viability peak at 4 days after cell seeding.

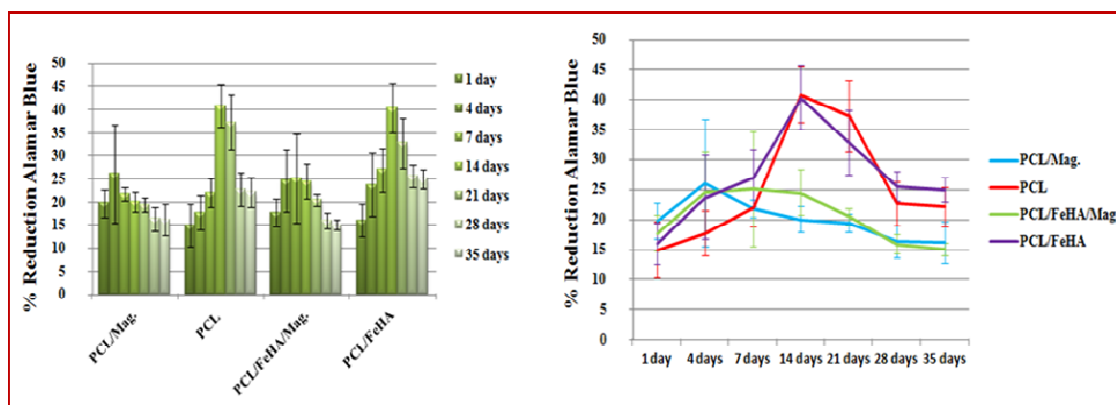


Figure 8: Results obtained from Alamar Blue™ Assay performed on Group 1 reported as mean value \pm standard deviation. PCL/MAG. and PCL/FeHA/MAG. indicate polymeric and nanocomposite scaffolds of Group 1, stimulated by a sinusoidal magnetic field. “Mag.” has been introduced to denote the application of a magnetic field.

At 35 days after cell seeding, SEM images (Figure 9) have shown that an increase in the number of hMSCs, which adhered on not magnetically stimulated PCL and PCL/FeHA scaffolds, is quite evident if compared to magnetized cell-constructs. In particular, hMSCs were well spread and better adhered on PCL/FeHA nanocomposites in comparison to those seeded on PCL substrates. On the other hand, these results seem to be consistent with those obtained from Alamar BlueTM assay.

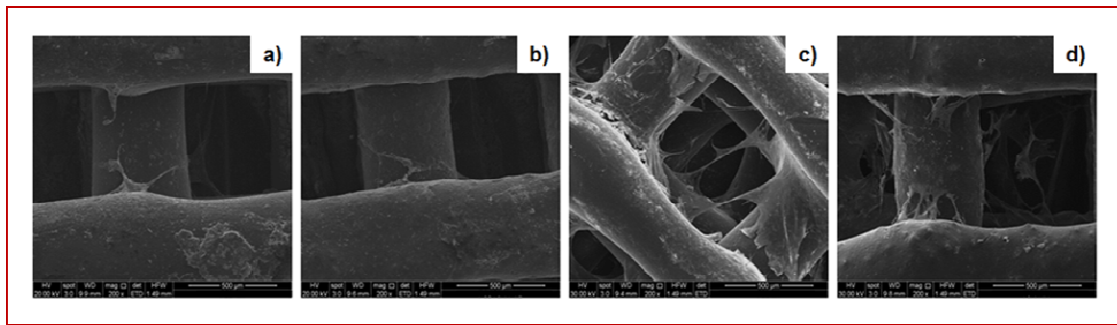


Figure 9: SEM images of different cell-constructs: a) PCL/Mag., b) PCL/FeHA/Mag., c) PCL, d) PCL/FeHA. Scale Bar - 500 µm.

Figure 10 reports an overall image of cell-construct at 35 days after cell seeding and a higher magnification of a central zone.

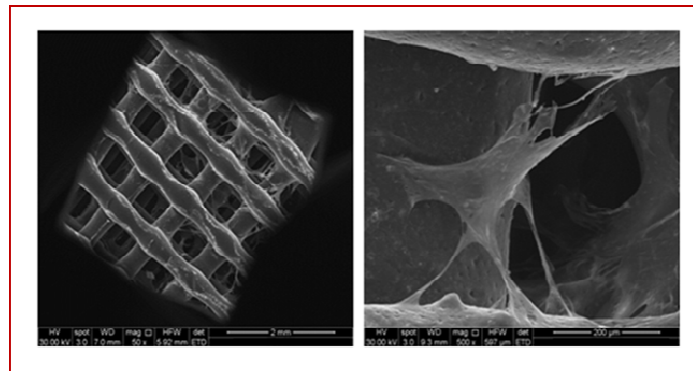


Figure 10: SEM images of: (left) cell-scaffold construct, Scale Bar - 2mm, (right) a higher magnification of a central zone, Scale Bar - 200 µm.

Alamar BlueTM assay performed on Group 2 (frequency 70 Hz, intensity 30 mT for 6 h per day distributed in 18 minute intervals) has shown interesting results in terms of cell viability/proliferation (Figure 11).

hMSCs are viable on both PCL and PCL/FeHA substrates. In particular PCL/FeHA scaffolds have provided higher values of the percentage of Alamar BlueTM reduction if compared to PCL ones. This result should be probably ascribed to the greater roughness of nanocomposites that enhances cell adhesion. On the other hand, the nanoparticle inclusion also enhances hydrophilicity of the materials, as evidenced by the lower values of water contact angle in comparison with those of neat PCL.¹

It is worth noting that not magnetically stimulated PCL and PCL/FeHA scaffolds have provided a maximum viability peak at 14 days after cell seeding whereas magnetically stimulated scaffolds at 4 days after cell seeding. This may suggest that cells should be induced to stop earlier their proliferation.

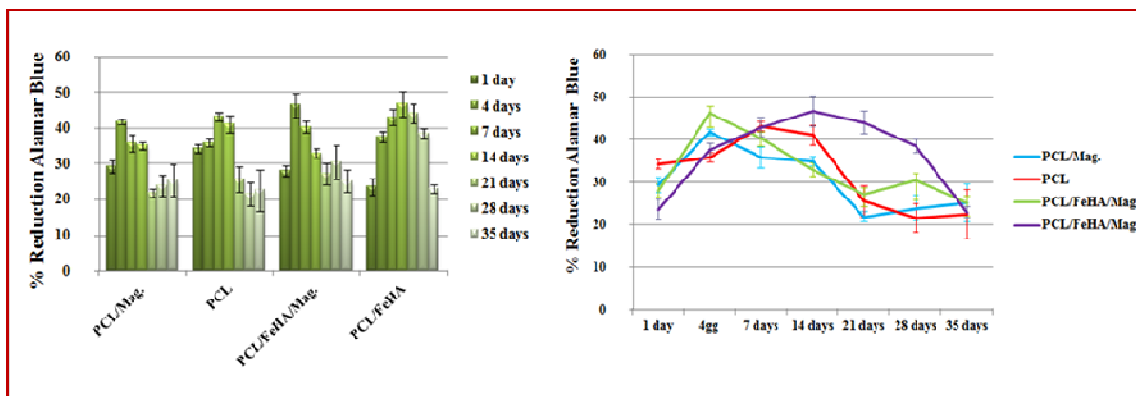


Figure 11: Results obtained from Alamar BlueTM assay performed on Group 2 reported as mean value \pm standard deviation. PCL/MAG. and PCL/FeHA/MAG. indicate polymeric and nanocomposite scaffolds of Group 2, stimulated by a sinusoidal magnetic field. "Mag." has been introduced to denote the application of a magnetic field.

At 4 days and 14 days after cell seeding, SEM analyses (Figure 12) have provided interesting results in terms of cell adhesion.

In particular, at 4 days it seems that a higher number of cells adhere and are well spread on polymeric and nanocomposite scaffolds under magnetic stimulation. Furthermore, at 14 days after cell seeding, cells would seem to be well spread on all the rapid prototyped scaffolds.

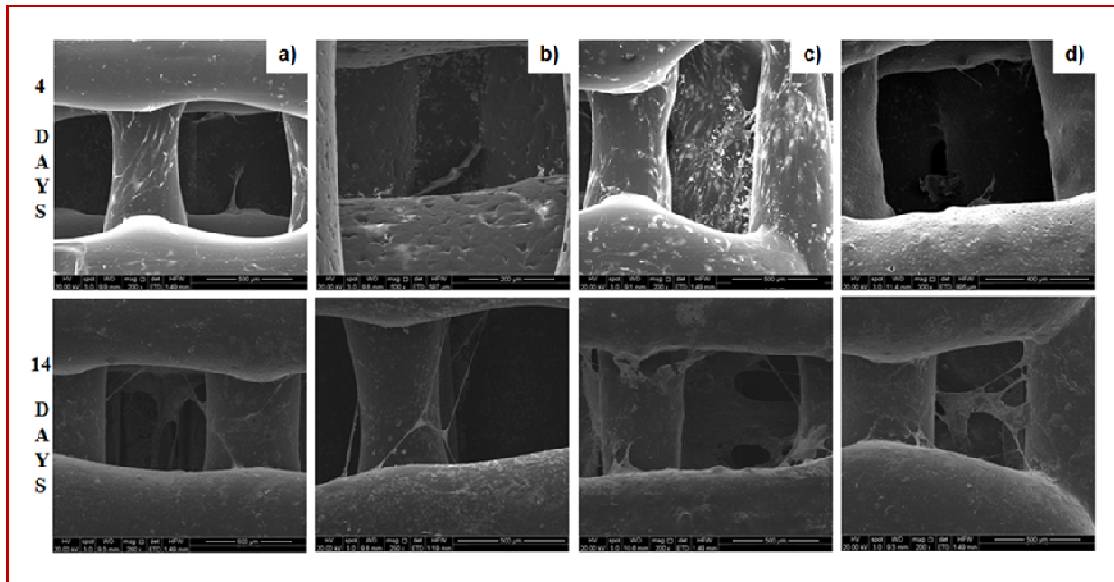


Figure 12: SEM images of different cell-constructs at 4 and 14 days after cell seeding: a) PCL/Mag., b) PCL/FeHA/Mag., c) PCL, d) PCL/FeHA. Scale Bar - 500 µm.

In conclusion, Group 1 and Group 2 constructs have shown a similar behavior.

However, Group 2 does not exhibit lower value of Alamar BlueTM reduction, as it occurs for Group 1. This effect should be ascribed to an early apoptosis due to an overheating effect of the environment.

This study may be considered as a first step of a future complex work with the aim of studying the effect of a sinusoidal magnetic field on cell differentiation.

Future works should take into account also the possibility to suitably modify the intensity and the frequency of the applied field in order to optimize the magnetic stimulation process.

4.3.3.2 Magnetically-charged cells and magnetic scaffolds: Scaffold-cell loading

Figure 13 shows the effect of the presence of a magnetic field on magnetically-charged cell loading of the scaffold.

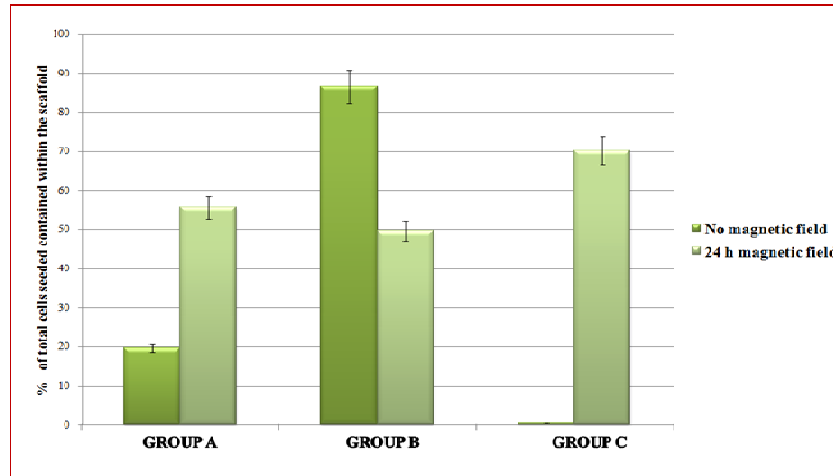


Figure 13: Cell loading of magnetic scaffolds in the presence or absence of a magnetic field. The number of MNPs-cells associated with scaffolds at 24 h is expressed as percentage of total loaded cells.

In particular, it seems that two of the three scaffolds (Group A and C) showed an increase in cell number associated with the scaffold when a magnetic field was applied throughout the 24 h loading period. Group B exhibited a behavior that results difficult to explain.

With this treatment, results have shown that there was a consistently higher number of cells present in the scaffolds at 72 h after loading in the presence of a 24 h magnetic field (Figure 14), compared with the negative control (loading in the absence of a magnetic field). However, in the case of scaffolds B and C, there was no evidence of cell population expansion during the 72 h time course of the assay. Just as an example, Group A loaded with magnetic field assistance showed growth of the cell population by ~50%, thus it should be considered as the best performing structure

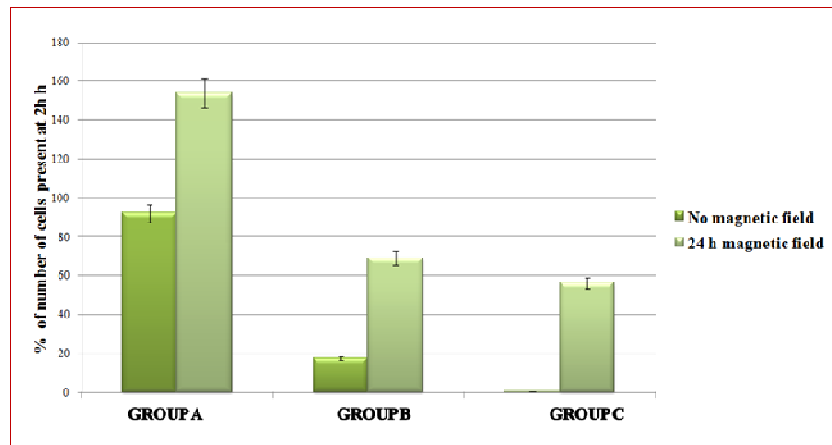


Figure 14: Scaffold content after 72 h culture. Cell content is expressed as a percentage of scaffold-associated cell number at loading

Figure 15 highlights the effect of different magnetic field exposure time on the efficiency of cell loading.

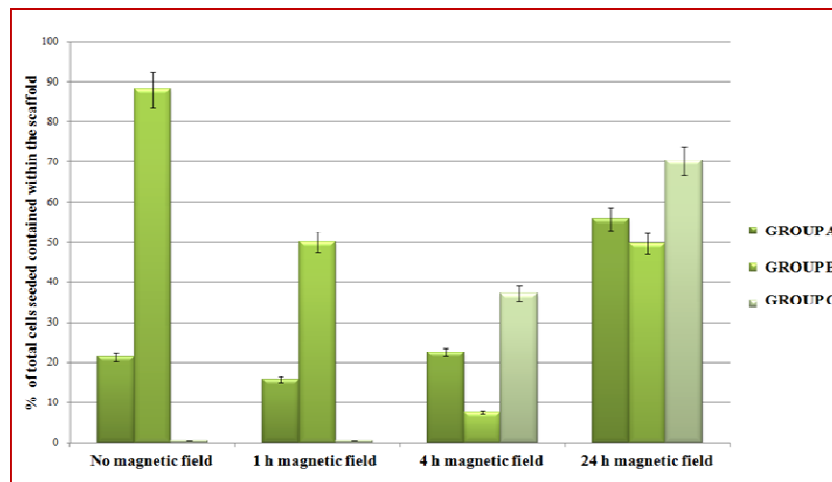


Figure 15: Effect of different magnetic field exposure time on the efficiency of cell loading. The number of MNPs-cells associated with scaffolds at 24 h is expressed as percentage of total loaded cells.

Even though both Group A and Group C have exhibited a defined behavior at 24 h, Group A showed no effect of the magnetic field until an exposure time of 24 h was considered. Group C showed a progressive increase in scaffold-cell loading with longer magnetic field exposure.

In conclusion, the experimental results have indicated that, using magnetically-charged cells and magnetic scaffolds, the application of a magnetic field at time of scaffold loading provides some

benefits in terms of the efficiency of cell loading. Interestingly, the results also suggest that there may be longer-term benefit during a subsequent cell-based assay period, as shown for the Group A in which good cell growth is quite evident.

Accordingly, magnetic forces may enhance cell anchorage at loading, thus improving the potential for cell growth and retention in the 3D environment.

4.4 *In vivo* experiments and histological analysis

At 4 weeks post-implantation, macroscopic evaluation showed the implants to be in the proper position and there was no evidence of haematoma, oedema, infection or tissue necrosis in either bone and peri-implant soft tissue associated with control or magnetic implants. Bone tissue was well visible around and inside the scaffold in both groups (Figure 16). Due to the interconnected structure, bone regenerated into the magnetic scaffold and after only 4 weeks some parts of the scaffolds were completely full of new formed bone proving a good level of histocompatibility of the scaffold comparable to the control group (Figure 16).

After 4 weeks, the PCL/FeHA construct showed mineralized tissue regeneration into its structure in a similar manner as PCL one.

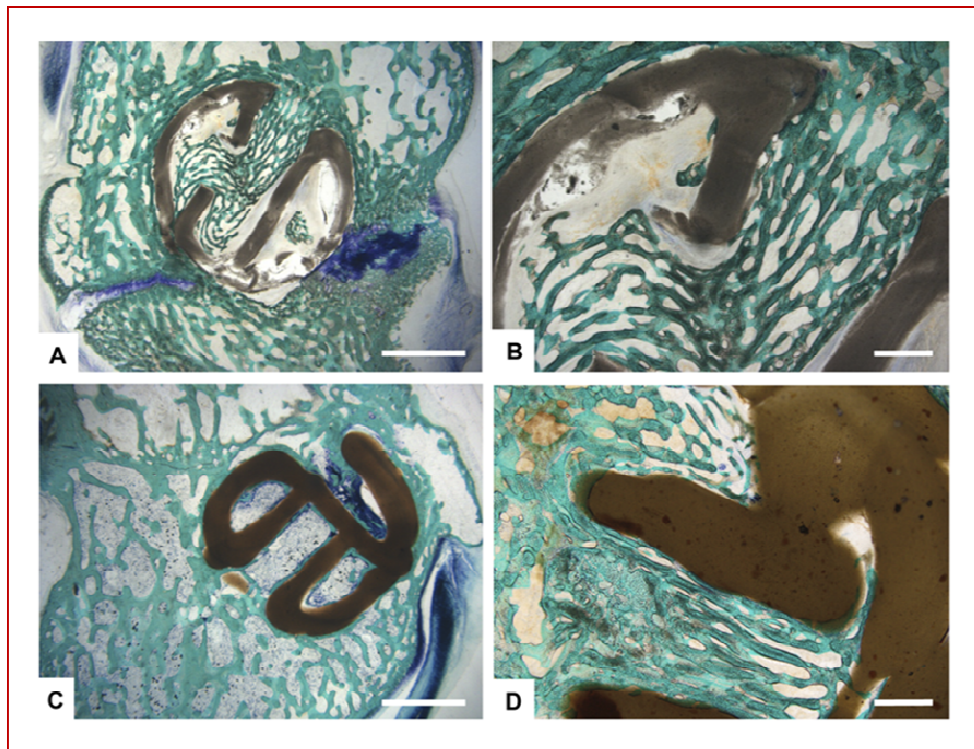


Figure 16: Histological evaluation of the *in vivo* implanted scaffolds. Toluidine Blue, Acid Fucsin and Fast Green staining shows similar histocompatibility for both scaffolds 4 weeks after implantation (n=6). A, B) Control, C, D) PCL/FeHA. Scale bars: A, C) 3.0 mm, B, D) 1.0 mm

Conclusions

Benefiting from previous results, nanocomposite scaffolds were firstly designed by embedding FeHA nanoparticles into a PCL matrix. A PCL/FeHA weight ratio (w/w) of 80/20 was used. The effect of nanoparticle inclusion on the mechanical performances of the substrates has been evaluated through compression tests, whilst morphological features were assessed through scanning electron microscopy.

Two important skills of the magnetic scaffolds have been considered. In a first step, it has been demonstrated the possibility to enhance cell proliferation employing a sinusoidal magnetic field. A second step has been focused on the feasibility to increase cell-loading efficiency by using magnetically-charged cells.

Finally, *in vivo* experiments have highlighted PCL/FeHA as a suitable candidate for bone tissue regeneration and it has opened new perspectives for the application of a magnetic field in a clinical setting of bone replacement.

Dr. V. D'Antò and dr. V. Riveccio from Department of Oral and Maxillofacial Sciences, University of Naples "Federico II", Napoli, Italy, are gratefully acknowledged for their valuable contribution in the biological analyses under magnetic stimulation.

Prof. J.W. Colin from AvantiCell Science Ltd, Scotland, United Kingdom, is kindly acknowledged for his collaboration in the biological experiments with magnetically-charged cells.

Dr. A. Russo and dr. S. Panseri from Rizzoli Orthopaedic Institute, Bologna, Italy, are kindly acknowledged for their support in the *in vivo* experiments and histological analysis.

References

1. Gloria A., Russo T., D'Amora U., Zeppetelli S., D'Alessandro T., Sandri M., Bañobre-Lopez M., Piñeiro-Redondo Y., Uhlarz M., Tampieri A., Rivas J., Herrmannsdörfer T., Dediu V.A., Ambrosio L., De Santis R. *Magnetic poly(ϵ -caprolactone)/iron-doped hydroxyapatite nanocomposite substrates for advanced bone tissue engineering*. J. R. Soc. Interface. 10: (80), 1-11, 2013.
2. Xiaolan Ba., Hadjiargyrou M., Di Masi E., Meng Y., Simon M., Tan Z., Rafailovich M.H. *The role of moderate static magnetic fields on biomineralization of osteoblasts on sulfonated polystyrene films*. Biomaterials. 32: 7831 -7838, 2011.
3. Ross S.M. *Combined DC and ELF magnetic fields can alter cell proliferation*. Bioelectromagnetics. 11: 27-36, 1990.
4. Hashimoto Y., Kawasumi M., Saito M. *Effect of static magnetic field on cell migration*. Electr. Eng. Jpn. 160: 46-52, 2007.
5. Kotani H., Kawaguchi H., Shimoaka T., Iwasaka M., Ueno S., Ozawa H., et al. *Strong static magnetic field stimulates bone formation to a definite orientation in vitro and in vivo*. J. Bone Miner. Res. 17: 1814-21, 2002.
6. Noriega-Luna B., Sabanero M., Sosa M., Avila-Rodrigueza M. *Influence of pulsed magnetic fields on the morphology of bone cells in early stages of growth*. Micron. 42: 600–607, 2011.
7. Miyakoshi J. *Effects of static magnetic fields at the cellular level*. Prog. Biophys. Mol. Biol. 87: 213–223, 2005.
8. Rosen A.D. *Mechanism of action of moderate-intensity static magnetic fields on biological systems*. Cell. Biochem. Biophys. 39: 163–173, 2003.
9. Yan Q.C., Tomita N., Ikada Y. *Effects of static magnetic field on bone formation of rat femurs*. Med. Eng. Phys. 20: 397-402, 1998.
10. Bruce J.N., Criscuolo G.R., Merrill M.J., Moquin R.R., Blacklock J.B., Oldfield E.H. *Vascular permeability induced by protein product of malignant brain tumors: inhibition by dexamethasone*. J. Neurosurg. 67: 880-4, 1987.
11. Degen I.L., Stetsula V.I. *Consolidation of bone fragments in a constant magnetic field*. Ortop. Travmatol. Protez. 32: 45-8, 1971.
12. Fassina L., Visai L., Benazzo F., Benedetti L., Calligaro A., Cusella De Anegelis M.G., Farina A., Maliardi V., Magenes G. *Effects of Electromagnetic Stimulation on Calcified Matrix Production by SAOS-2 Cells over a Polyurethane Porous Scaffold*. Tissue Eng. 12 (7): 1985-1999, 2006.
13. Chiu K.H., Ou K.L., Lee S.Y., Lin C.T., Chang W.J., Chen C.C., Huang H.M. *Static Magnetic Fields Promote Osteoblast-Like Cells Differentiation Via Increasing the Membrane Rigidity*. Ann. Biomed. Eng. 35: 11, 1932–1939, 2007.

14. Feng S.W., Lo Y.J., Chang W.J., Lin C.T., Lee S.Y., Abiko Y., Huang H.M. *Static magnetic field exposure promotes differentiation of osteoblastic cells grown on the surface of a poly-L-lactide substrate*. Med. Biol. Eng. Comput. 48:793–798, 2010.
15. Sato K., Yamaguchi H., Miyamoto H., Kinouchi Y. *Growth of human cultured cells exposed to a non-homogeneous static magnetic field generated by Sm-Co magnets*. Biochem. Biophys. Acta. 1136: 231–238, 1992.
16. Pacini S., Vannelli G.B., Barni T., Ruggiero M., Sardi I., Pacini P., Gulisano M. *Effect of 0.2 T static magnetic field on human neurons: remodeling and inhibition of signal transduction without genome instability*. Neurosci. Lett. 267: 185–188, 1999.
17. Pacini S., Gulisano M., Peruzzi B., Sgambati E., Gheri G., Bry, S.G., Vannucchi S., Polli, G., Ruggiero M. *Effects of 0.2mT static magnetic field on human skin fibroblasts*. Cancer Detect. Prev. 27: 327–332, 2003.
18. Cunha C., Panseri S., Marcacci M., Tampieri A. *Evaluation of the Effects of a Moderate Intensity Static Magnetic Field Application on Human Osteoblast-Like Cells*. Am. J. Biomed. Eng. 2(6): 263–268, 2012.
19. Chang K., Chang W.H.S., Wu M.L., Shih C. *Effects of different intensities of extremely low frequency pulsed electromagnetic fields on formation of osteoclast-like cells*. Bioelectromagnetics. 24: 431–439. 2003.
20. Chang K., Chang W.H., Huang S., Huang S., Shih C. *Pulsed electromagnetic fields stimulation affects osteoclast formation by modulation of osteoprotegerin, RANK ligand and macrophage colony-stimulating factor*. J. Orthop. Res. 23: 1308–1314, 2005.
21. Schwartz Z., Fisher M., Lohmann C.H., Simon B.J., Boyan B.D. *Osteoprotegerin (OPG) production by cells in the osteoblast lineage is regulated by pulsed electromagnetic fields in cultures grown on calcium phosphate substrates*. Ann. Biomed. Eng. 37: 437–44, 2009.
22. Chang K., Chang W.H. *The influence of pulsed electromagnetic field (PEMF) on osteopenia in an ovariectomized female rat model*. In: Proceedings of the 23rd Annual Meeting of the Bioelectromagnetics Society, St Paul, MN, 2001.
23. Park K.H., Soda A., Yamaguchi H., Kinouchi Y., Yoshizachi K. *Effects of magnetic field on collagen synthesis in osteoblasts*. In: Electricity and Magnetism in Biology and Medicine, edited by Bersani, Kluwer Academic/Plenum Publishers. 457-460, 1999.
24. Nakajima T., Ishiguro A., Wakatsuki Y. *Formation of Super Wires of Clusters by Self-Assembly of Transition Metal Cluster Anions with Metal Cations*. Angew. Chem. Int. Ed. 40 (6): 2001.
25. Liboff A.R., Williams Jr. T., Strong D.M., Wistar Jr. R. *Time-varying magnetic fields: effect on DNA synthesis*. Science. 223: 818–820, 1984.
26. De Mattei M., Caruso A., Traina G.C., Pezzetti F., Baroni T., Sollazzo V. *Correlation between pulsed electromagnetic fields exposure time and cell proliferation increase in human osteosarcoma cell lines and human normal osteoblast cell in vitro*. Bioelectromagnetics. 20: 117–182, 1999.

27. Diniz P., Shomura K., Soejima K., Ito G. Effects of pulsed electromagnetic field (PEMF) stimulation on bone tissue like formation are dependent on the maturation stages of the osteoblasts. *Bioelectromagnetics*. 23 (5): 398–405, 2002.
28. Chang W.H.S., Chen L.T., Sun J.S., Lin F.H. *Effect of pulse-burst electromagnetic field stimulation on osteoblast cell activities*. *Bioelectromagnetics*. 25: 457–465, 2004.
29. Martino C.F., Belchenko D., Ferguson V., Nielsen-Preiss S., Qi H.J. *The effects of pulsed electromagnetic fields on the cellular activity of SaOS-2 cells*. *Bioelectromagnetics*. 29: 125–132, 2008.
30. Ba X., Hadjiargyrou M., Di Masi E., Meng Y., Simon M., Tan Z., Rafailovich M.H. *The role of moderate static magnetic fields on biomineralization of osteoblasts on sulfonated polystyrene films*. *Biomaterials*. 32(31):7831-8, 2011.
31. Wang Z., Che P.L., Du J., Ha B., Yarema K.J. *Static magnetic field exposure reproduces cellular effects of the Parkinson's disease drug candidate ZM241385*. *PLoS One*. 5(11): e13883, 2010.
32. Luciani A., Wilhelm C., Bruneval P., Cunin P., Autret G., Rahmouni A., Clément O., Gazeau F. *Magnetic targeting of iron-oxide-labeled fluorescent hepatoma cells to the liver*. *Eur. Radiol*. DOI 10.1007/s00330-008-1262-9, 2008.
33. Corot C., Robert P., Idee J.M., Port M. *Recent advances in iron oxide nanocrystal technology for medical imaging*. *Adv. Drug Deliv. Rev*. 58:1471–1504, 2006.
34. Bulte J.W., Kraitchman D.L. *Iron oxide MR contrast agents for molecular and cellular imaging*. *NMR Biomed*. 17: 484–499, 2004.
35. Anat Y., Häfeli U.O., Metcalfe A.L., Soema P., Addo L., Gregory-Evans C.Y., Po K., Shan X., Moritz O.L., Gregory-Evans K. *Focused Magnetic Stem Cell Targeting to the Retina Using Superparamagnetic Iron Oxide Nanoparticles*. *Cell Transplantation*. 21: 1137–1148, 2012.
36. Tang C., Russell P.J., Martiniello-Wilks R., Rasko J.E., Khatri A. *Concise review: Nanoparticles and cellular carriers-allies in cancer imaging and cellular gene therapy?* *Stem Cells*. 28: 1686–1702, 2010.
37. Loebinger M.R., Kyrtatos P.G., Turmaine M., Price A.N.; Pankhurst Q., Lythgoe M.F., Janes S.M. *Magnetic resonance imaging of mesenchymal stem cells homing to pulmonary metastases using biocompatible magnetic nanoparticles*. *Cancer Res*. 69: 8862–8867, 2009.
38. Tiefenauer L.X. *Magnetic nanoparticles as contrast agents for medical diagnosis*. In: Vo-Dinh, T., ed. *Nano-technology in biology and medicine: Methods, devices and applications*. Boca Raton, FL: CRC Press: 1–20, 2007.
39. Wilhelm C., Bal L., Smirnov P., Galy- Fauroux I., Clement O., Gazeau F., Emmerich J. *Magnetic control of vascular network formation with magnetically labeled endothelial progenitor cells*. *Biomaterials*. 28: 3797–3806, 2007.
40. Arbab A.S., Liu W., Frank J.A. *Cellular magnetic resonance imaging: current status and future prospects*. *Expert Rev. Med. Devices*. 3: 427–439, 2006.

41. Hoehn M., Kustermann E., Blunk J., Wiedermann D., Trapp T, Wecker S., Focking M., Arnold H., Hescheler J., Fleischmann B.K., Schwindt W., Buhle C. *Monitoring of implanted stem cell migration in vivo: a highly resolved in vivo magnetic resonance imaging investigation of experimental stroke in rat.* Proc. Nat. Acad. Sci. USA. 99: 16267– 16272, 2002.
42. Pamme N., Wilhelm C. *Continuous sorting of magnetic cells via on chip free-flow magnetophoresis.* Lab Chip. 6: 974–980, 2006.
43. Wilhelm C., Riviere C., Biais N. *Magnetic control of Dictyostelium aggregation.* Phys. Rev. E Stat. Non lin. Soft Matter Phys. 75: 041906, 2007.
44. Pislaru S.V., Harbuzariu A., Agarwal G., Witt T., Gulati R., Sandhu N.P., Mueske C., Kalra M, Simari R.D., Sandhu G.S. *Magnetic forces enable rapid endothelialization of synthetic vascular grafts.* Circulation. 114:I314–I318, 2006.
45. Ito A., Hibino E., Kobayashi C., Terasaki H., Kagami H., Ueda M., Kobayashi T., Honda H. *Construction and delivery of tissue-engineered human retinal pigment epithelial cell sheets, using magnetite nanoparticles and magnetic force.* Tissue Eng. 11: 489–496, 2005.
46. Ino K., Ito A., Honda H. *Cell patterning using magnetite nanoparticles and magnetic force.* Biotechnol. Bioeng. 97: 1309–1317, 2007.
47. Shimizu K., Ito A., Lee J.K., Yoshida T., Miwa K., Ishiguro H., Numaguchi Y., Murohara T., Kodama I., Honda H. *Construction of multi-layered cardiomyocyte sheets using magnetite nanoparticles and magnetic force.* Biotech. Bioeng. 96 (4): 803–809, 2007.
48. Moreau J., Anderson K. M., Mauney J.R., Kaplan D., Rosenblatt M. *Studies of Osteotropism on Both Sides of the Breast Cancer–Bone Interaction.* Ann. N.Y. Acad. Sci. 1117: 328–344, 2007.
49. Bellahcene A., Castronovo V. *Expression of bone matrix proteins in human breast cancer: potential roles in microcalcification formation and in the genesis of bone metastases.* Bulletin du Cancer 84: 17–24, 1997.
50. Tampieri A., D’Alessandro T., Sandri M., Sprio S., Landi E., Bertinetti L., Panseri S., Peponi G., Goettlicher J., Bañobre-López M., Rivas, J. *Intrinsic magnetism and hyperthermia in bioactive Fe-doped hydroxyapatite.* Acta Biomater. 8: 843–51, 2012.

Conclusions and Future Trends

In the field of bone tissue engineering, great attention has been given toward the material and scaffold features including morphological, mechanical and transport properties through a suitable topological optimization. This work has introduced another important scaffold property. Scaffold should be also superparamagnetic in order to obtain a controlled delivery system, which should be manipulated *in situ* by means of magnetic forces providing bioagents and growth factors (i.e. vascular endothelial growth factor, VEGF). The main driving idea was, thus, the achievement of a “fixed station” that, once it is implanted *in vivo*, should offer a long-living assistance to implanted tissue engineering constructs, recruiting VEGF functionalized magnetic nanoparticles (MNPs) and releasing them when and where it is required by tissue regeneration process. A magnetic scaffold could be able to recruit magnetically-charged cells, which under application of a magnetic field gradient could behave as shuttles toward the static structure. In the field of biomedicine, magnetic nanoparticles have been widely studied for their hyperthermia features, giving them the possibility to be used in the treatment of tumors. A magnetic scaffold should be employed also in this field.

As first step, the design of 3D fiber deposited poly(ϵ -caprolactone)/iron oxide (PCL/Fe₃O₄) nanocomposite scaffolds has been described. The effect of iron oxide nanoparticle inclusion on morphological, mechanical, magnetic and biological performances has been assessed.

Successively, in order to avoid the dangerous problem of leaving any non bioresorbable magnetic inclusion (for example magnetite) inside the repaired tissue, PCL/iron-doped hydroxyapatite (FeHA) nanocomposite substrates were designed and characterized using different polymer-to-particle weight ratios. The effect of FeHA nanoparticle inclusion on morphological, mechanical, magnetic and biological performances has been assessed. This has allowed to choose the optimal polymer-to-particle weight ratio. In particular, a nanoparticle amount of 20% by weight embedded into the polymeric matrix has shown the best compromise between all the above reported features

and then, 3D morphologically controlled PCL/FeHA 80/20 (w/w) nanocomposite scaffolds have been manufactured.

The effect of a sinusoidal magnetic stimulation on adhesion and proliferation of cells seeded on PCL/FeHA scaffolds has been studied. Future works will be focused on the effect of variable magnetic field on cell differentiation.

This work may represent a first approach toward the design of morphologically controlled and fully biodegradable PCL/FeHA nanocomposite magnetic scaffolds, which should be able to improve cell recruitment and cell-loading efficiency.

Preliminary results from histological experiments performed on rabbits have shown that PCL/FeHA scaffolds were completely full of new formed bone indicating a good level of histocompatibility.

Appendix

Historical introduction

Magnetism is a subject, which has been studied for more than thousand years; when a selection of ores, such as ferrites ($MO Fe_2O_3$, $M = Fe, Mn, Zn, Sr...$), was found to be “attractive” or “magnetic” and capable of attracting small pieces of iron.

The term magnetism is derived from Magnesia, a city and region of ancient Greece known for the abundance of magnets, rocks rich in magnetite, Fe_3O_4 .

Aristotle attributes the first scientific discussion on magnetism to Thales of Miletus, who lived from about 625 to about 545 B.C. Around the same time, in ancient India, the Indian surgeon, Sushruta, was the first to make use of the magnet for surgical purposes.

In ancient China, literary reference to magnetism can be found in a 4th century B.C. book called “Book of the Devil Valley Master”: “The lodestone makes iron come or it attracts it”. The Chinese understood that a piece of iron in the vicinity of a natural magnet acquired and retained over the time the magnetization. The next step in understanding of electromagnetism was realizing that the “magnetic needle” is free to rotate naturally turn guided along the geographic North - South. In East, already in 400 A.D. magnets were used in navigation, such as compasses.

We find news of magnetic phenomena already in the writings of Pliny the Elder (Historiae Naturalis), but in 1187, Alexander Neckham, was the first in Europe to describe the compass and its use for navigation. In 1269, Peter Peregrinus de Maricourt wrote the “Epistola de magnete”, the first extant treatise describing the properties of magnets. In 1600, William Gilbert published his “De Magnete, Magneticisque Corporibus, et de Magno Magnete Tellure” (On the Magnet and Magnetic Bodies, and on the Great Magnet the Earth). In this work he described many of his experiments and he concluded that the Earth was itself magnetic and that this was the reason compasses pointed north (previously, some believed that it was the pole star (Polaris) or a large magnetic island on the North Pole that attracted the compass). In 1819 Oersted understood the connection between electric phenomena and magnetic phenomena.

In 1831 Faraday discovered that a circuit in which current flows develops the magnetic phenomena. A magnet generates a magnetic field in the surrounding space and is subject to turn to a moment of forces in an external magnetic field. James Clerk Maxwell synthesized and expanded these insights into Maxwell's equations, unifying electricity, magnetism, and optics into the field of electromagnetism. In 1905, Einstein used these laws in motivating his theory of special relativity, requiring that the laws held true in all inertial reference frames.

All the materials are influenced varyingly by the presence of a magnetic field and have magnetic properties. The term magnetism describes a range of materials that can be divided in five main groups: paramagnetic, diamagnetic, ferromagnetic, antiferromagnetic and ferrimagnetic materials.^{1,2}

Basic Principles of Magnetism

Macroscopic magnetic properties of the materials come from the magnetic moments associated with individual electrons. In the atom, each electron has magnetic moments that originate from two sources: the first is due to the orbital motion round the nucleus (orbital magnetic moment), the other is due to the rotation of the electron around its own axis, associated with a fundamental quantum property, their spin (the magnetic moment of spin). For each electron the magnetic moment of spin is $\pm\mu_B$, where μ_B is the Bohr magneton (μ_B) that has the value of $9.27*10^{-24} \text{ Am}^2$. The orbital magnetic moment is equal to $m_l\mu_B$, where m_l is magnetic quantum number of the electron.

The symbol of a magnetic field can be referred to either B or H , which are different in both unit and definition. The B field is also defined as the magnetic induction or flux density, and it is the value of the magnetic field strength of a material subjected to an H field. The unit is Tesla (T) in the S.I. system and Gauss (G) in the C.G.S. system, where one T is equal to 10 kG . The H field is also defined as the field strength and the unit is Ampere per meter ($A \text{ m}^{-1}$) in the S.I. system and is Oersted (Oe) in the C.G.S. system. The magnetic induction (B) is the sum of the applied (H) field and the external field due to the magnetization.

If a magnetic material is placed in a magnetic field of strength H , the individual atomic moments in the material contribute to its overall response, the magnetic induction:

$$B = \mu_0 H + \mu_0 M = \mu_0 (H + M) \quad (1)$$

where μ_0 is the permeability of free space ($4\pi*10^{-7} \text{ Tm/A}$), and the magnetization $M = m/V$ is the magnetic moment per unit volume.

All the materials can be conveniently classified in terms of their volumetric magnetic susceptibility, χ , defined as:

$$M = \chi H \quad (2)$$

In SI units χ is dimensionless and both H and M are expressed in Am^{-1} . Thus, the equation (2) describes the magnetization induced in a material by H .

Under conditions of time-variant magnetic field the magnetic susceptibility can be expressed as a function of the frequency of the magnetic field:

$$\chi(\omega) = \chi'(\omega) - i\chi''(\omega) \quad (3)$$

Where $\chi'(\omega)$ is the real component while $\chi''(\omega)$ is the imaginary component, in turn expressible as:

$$\chi'(\omega) = \frac{\chi_0}{1 + (\omega t)^2} \quad (4)$$

$$\chi''(\omega) = \frac{\omega t}{1 + (\omega t)^2} \chi_0 \quad (5)$$

Where χ_0 is defined as the susceptibility at the equilibrium (or at low frequency); ω is the magnetic field pulsation ($\omega = 2\pi f$, f is frequency field), t is the relaxation time. The real part of the susceptibility is proportional to the component of the magnetization that is induced in phase with the applied modulation while the imaginary part is proportional to the $\pi/2$ out of phase or quadrature component of the magnetization. This latter part is directly proportional to the dissipation in the material.

Paramagnetism and Diamagnetism

Most materials show little magnetism, and even then only in the presence of an applied field; these are classified as paramagnets, or diamagnets.

The paramagnetism is a form of magnetism that some materials show only in the presence of magnetic fields, and is manifested by a magnetization having the same direction and toward that of the external field. The susceptibility, χ is positive and spans from 10^{-6} to 10^{-1} . Since the thermal agitation randomly distributes the directions of the magnetic dipoles, an increase in temperature decreases the paramagnetic effect.^{2,3}

The characteristic of paramagnetism can be understood by postulating permanent atomic magnetic moments, which can be re-oriented in an external field. These moments can be either due to orbiting

electrons or due to atomic nuclei. The torque applied by an external magnetic field on these moments will tend to fix them parallel to the field, which then reinforces it.⁴

All the organic substances, some metals and superconductors below the critical temperatures are diamagnetic. An external magnetic field induces magnetic dipoles that are oriented antiparallel with respect to the exciting field due to Lenz's rule (magnetic field is produced in a induced current and the magnetism is parallel to the electromotive force). Therefore, the susceptibility, χ is negative and falls in the range $10^{-6} \div 10^{-1}$.

When the magnetic field is turned off, there is no permanent magnetization remaining in paramagnetic and diamagnetic materials.

Ferromagnetism, antiferromagnetism and ferrimagnetism

Some materials exhibit ordered magnetic states and are magnetic even without a field applied, these are classified as ferromagnets, antiferromagnets and ferrimagnets.

Ferromagnetic elements as iron (Fe), cobalt (Co) and nickel (Ni), which have unpaired electron spins align them spontaneously so that the material can show magnetizations without being in a magnetic field. Ferromagnetism is a so-called cooperative phenomenon, where single atoms cannot exhibit ferromagnetism, but the ferromagnetic properties arise when some of the atoms are bound together in solid form. If the field is reversed, ferromagnetic material will initially resist the field change, however most magnetic domains will eventually switch their magnetization vectors and come to the same inverse magnetization.⁵ The field produced by ferromagnetic materials (obviously magnetized) is very intense and lasts a long time after removal of the external field. The susceptibility (χ) is much higher than zero and $\mu_0 M < \mu_0 H$. From equation (1), the B field and the M result in a linear relationship.^{4,6}

This property is maintained only below a certain temperature, called the **Curie temperature** above which the ordered structure of magnetic dipoles oriented is destroyed by the increase of thermal energy and the substance behaves as a paramagnetic material (Figure I).

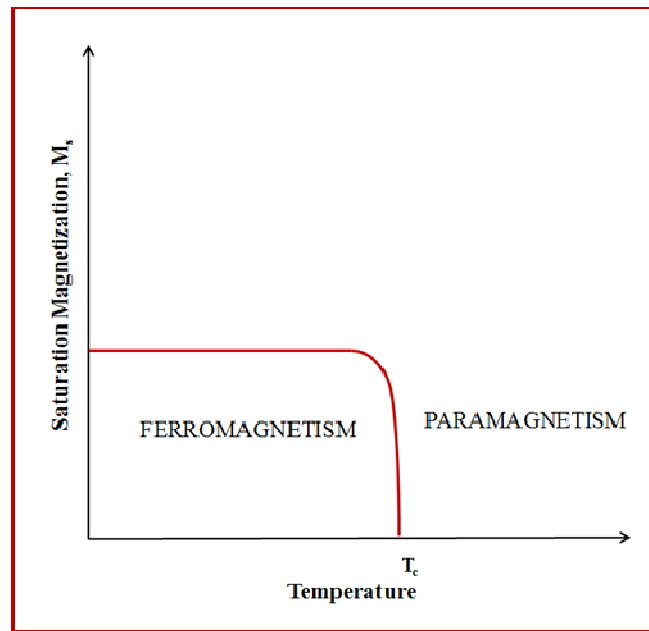


Figure I: Effect of the temperature increase on saturation magnetization (M_s) value for a ferromagnetic material under its Temperature Curie (T_c). Increasing the temperature, magnetic moments are randomly distributed and the material becomes paramagnetic.

Manganese (Mn), chromium (Cr), and other metal oxides are said antiferromagnetic. In such materials, the magnetic dipoles tend spontaneously to be arranged so as to cancel each other. At a macroscopic level, below a certain temperature, called **Néel temperature**, and in the absence of external magnetic field, the magnetization of these materials is practically zero. The Néel temperature is a temperature above which the order of the magnetic domains in the crystal structure is destroyed and the material behaves as a paramagnetic substance.

Ferrites (mixture of oxides of iron and other metals) and magnetic garnets (such as yttrium and iron garnet), which possess, as the ferromagnetic materials, permanent magnetic dipoles are named ferrimagnets. In ferrimagnetic materials the magnetic moments of the atoms are oriented in a manner similar to the antiferromagnetic materials, but the opposing moments are unequal and a spontaneous magnetization remains. This happens when the sublattices consist of different materials or ions (such as Fe^{2+} and Fe^{3+}). The ferrimagnetism is also called "decompensated antiferromagnetism", just for the fact that the opposing magnetic moments are not equal in magnitude. The ferrimagnetic materials, such as ferromagnetic ones, possess a spontaneous

magnetization under Curie temperature, and do not show magnetic order above this temperature.

The oldest known magnetic substance, magnetite (mixed oxide of iron (II, III), Fe_3O_4), is actually a ferrimagnet, it was originally classified as a ferromagnet before the discovery of Louis Néel (1904-2000, Nobel Prize for Physics in 1970) of the ferrimagnetism and antiferromagnetism.

In the following figure II, it is schematically represented the different moment orientation for paramagnetic (A), ferromagnetic (B), antiferromagnetic (C) and ferrimagnetic (D) materials.

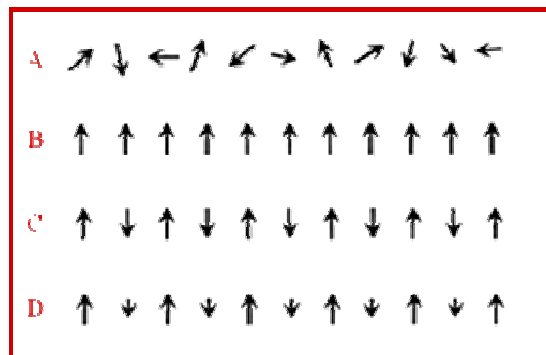


Figure II: Different moment orientation for magnetic materials.

In the following table I typical values for magnetic susceptibility, χ are reported.

Behavior	Typical values for magnetic susceptibility, χ
Diamagnetic	$-10^{-6} \div -10^{-1}$
Paramagnetic	$10^{-6} \div 10^{-1}$
Ferromagnetic	$\approx 10^3$
Antiferromagnetic	$0 \div 10^{-2}$

Table I: Typical values of magnetic susceptibility (χ) for magnetic materials.

Magnetic domains and hysteresis

Ferromagnetic and ferrimagnetic materials, under Curie temperature, consist of small volume regions where magnetic dipoles are arranged in the same direction. These regions are named domains and are magnetized up to own saturation magnetization value. Adjacent domains are separated by walls, where magnetization direction changes gradually. The domains are microscopic and in a polycrystalline material each grain can consist of several domains. The M field value for the whole solid is given by the vectorial sum of the magnetizations of all domains, weighing each domain contribution with its volume fraction. The flux density, B and the field strength H are not proportional. If the material is not initially magnetized, B depends on H as shown in figure III.

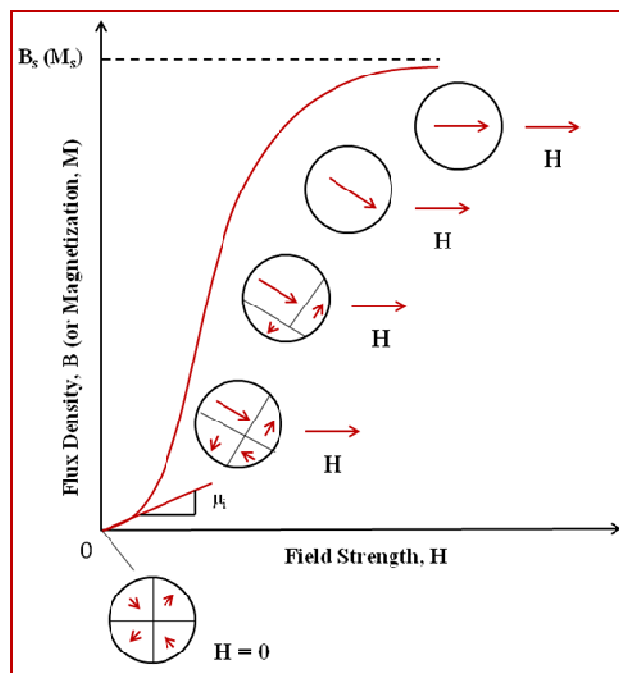


Figure III: B-H (or M-H) curve for a ferromagnetic or ferrimagnetic not initially magnetized material. The figure represents how domains change their configuration during the magnetization phenomenon.⁷

B increases slowly with the increase of H , then faster and successively becomes constant and independent from H . The maximum value of B is the flux density saturation, B_s . As the permeability μ is the slope of the curve B-H, it follows that μ varies with and is dependent on H . At $H=0$, the slope of the curve B-H is the initial permeability, μ_i . As shown in the figure III, with H increasing,

the domains change their form and dimension, due to the grain walls movement. Initially, domain magnetic moments are randomly arranged. Then, the domains arranged in the H field direction increase to the detriment of those that are randomly arranged. This phenomenon continues until the material becomes a single-domain aligned with the field. As shown in figure IV the characteristic shape of B-H (or M-H) curve is sigmoidal, with B (or M) approaching a saturation value (B_s or M_s) at large values of H . If the field is reversed, at the point “S” (figure IV), the curve does not return to the origin. This gives rise to a curve loop named hysteresis loop, where B field decreases with H field at lower speed.

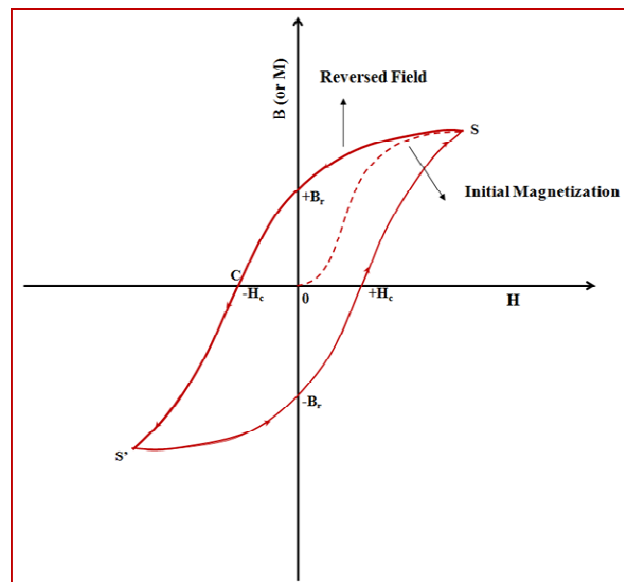


Figure IV: Characteristic sigmoidal shape of B-H (or M-H) curve, with B or M approaching a saturation value and hysteresis phenomenon for a ferromagnetic or ferrimagnetic material.⁷

The remaining magnetization value after removal of external field (at $H=0$) is B_r . The coercivity (H_c) is the H field value which is necessary to apply, in order to demagnetize the material.

The shape of magnetization curves (M-H) depends on the different type of magnetism.

Fundamentals of Magnetic Nanoparticles

Intensive studies of nanoparticles as a special class of objects started from the discovery of unusual magnetic properties. In 1930, Frenkel J. and Dorfman J. showed on the basis of energy considerations that particles of a sufficiently small size should be single-domain. These studies identified a substantial increase in the coercive force of a ferromagnet on passing from a multidomain to the single-domain structure, which is important for the creation of permanent magnets.^{8,9}

The critical diameter values corresponding to particle transition from the multidomain to the single-domain state were calculated for spherical particles with an axial magnetic anisotropy. For other types of anisotropy (cubic, hexagonal, etc.) and other particle shapes, the numerical estimation of the critical diameter for the single-domain character changes. In particular, the particle can be transferred into the single-domain state without decreasing the volume if it has a shape other than a sphere, for example, an oblong ellipsoid. The term “single-domain” does not require a necessary uniform magnetization throughout the whole particle bulk but only implies the absence of domain walls. In addition, a single-domain particle is not necessarily a “small” particle (as opposed to a “bulk” particle) as regards specific magnetic characteristics. Thus, the specific properties of nanoparticles start to be manifested at sizes much smaller than the “single-domain limit”.

One more remarkable property of the nanoparticles, which allowed their experimental discovery in the mid-20th century, is the superparamagnetism, the absence of residual magnetic force between particles upon removal of the magnetic field.⁸

Superparamagnetism

Superparamagnetism occurs when ferromagnetic or ferrimagnetic materials are reduced in size below about 50 nm in the largest dimension and present a single magnetic domain. Superparamagnetic materials may exhibit similar behavior to paramagnetism even at temperatures below the Curie temperature; magnetization can randomly flip direction under the influence of

temperature and the magnetic moment of the particle as a whole is free to fluctuate in response to thermal energy, while the individual atomic moments maintain the ordered state relative to each other.

Magnetic Anisotropy and Néel Relaxation time in absence of a magnetic field

The energy barrier to moment reversal has several origins, including both intrinsic and extrinsic effects such as the magnetically crystalline anisotropy and the shape anisotropy. The magnetically crystalline anisotropy energetically favors the alignment along a specific crystallographic direction, preferential magnetization axis (easy axis); it is an intrinsically material property, which depends on crystal lattice and its chemical environment.

The shape anisotropy, which is only present in objects of different shape from that spherical, helps to orient the magnetization along the longitudinal axis of the nanocrystal.

The magnetization anisotropy is often modeled as uniaxial and the anisotropic magnetic energy ΔE is described in its simplest form by the following equation:

$$\Delta E = K_v V \sin^2 \theta \quad (6)$$

Where K_v is the volume anisotropy energy density, V the particle volume and θ is the angle between the vector of the particle magnetic moment m and the anisotropy axis.

The anisotropy energy ΔE plays the role of energy barrier, which may be overcome in order to enable the rotations of the magnetic moments of the particles. If $\theta=0^\circ$ (i.e. the direction of magnetization corresponds to the easy axis), the potential energy reaches the minimum value. Reducing the size of a ferromagnetic nanoparticle up to a threshold value, defined as blocking dimension, to which is associated a blocking temperature, T_B , the energy ΔE becomes comparable to the thermal energy of activation, $k_B T$ (where k_B is the Boltzmann constant). In this case the anisotropic energy barrier is so small that thermal activation energy and/or an external magnetic field H can easily change the magnetization direction with respect to the axis preferential. If no

external magnetic field or surface anisotropy is present, the minimum energy of the particle is attained at the orientation of the magnetic moment, m , along the anisotropy axis. In this case, two neighboring minima are separated by a barrier with height $K_v V$.

Because of the nanoparticle magnetic anisotropy, the magnetic moment has usually only two stable orientations antiparallel to each other, separated by an energy barrier.

At finite temperature, there is a finite probability for the magnetization to flip and reverse its direction. The mean time between two flips as a result of thermal fluctuations is defined as the Néel relaxation time, τ , and is given by Néel-Arrhenius equation. The activation law for the relaxation time of the net particle magnetization was obtained by Néel:^{8,10}

$$\tau = \tau_0 \exp(\Delta E / k_B T) \quad (7)$$

where ΔE is the energy barrier to moment reversal, and $k_B T$ is the thermal energy. For non-interacting particles the pre-exponential τ_0 is of the order $10^{-10} \div 10^{-12}$ s and only weakly dependent on temperature.

At higher temperatures, $\Delta E / k_B T \leq 1$; the time required for system transition into a state with the minimum energy is short compared to the characteristic time of measurements τ_{meas} and the system is not expected to show a magnetic hysteresis, so, $\tau_{meas} \gg \tau$ and the system occurs in the superparamagnetic state and reaches an equilibrium magnetization on changing the temperature or the external field, the magnetization will not flip during the measurement, so the measured magnetization will be the instantaneous magnetization evaluated at the beginning of the measurement. In this state, an external magnetic field is able to magnetize the nanoparticles, similarly to a paramagnet. However, their magnetic susceptibility is much larger than that of a paramagnet.

In the case where $\Delta E / k_B T \geq 1$, the system transition into an equilibrium state may take a very long time depending on the particle. If $\tau_{meas} \ll \tau$, the nanoparticle magnetization will flip several times during the measurement, then the measured magnetization will average to zero.

In the former case, the nanoparticle will appear to be in the superparamagnetic state whereas in the latter case it will appear to be “blocked” in its initial state. At very low temperatures nanoparticles remain “frozen magnetically” and behave like a ferromagnetic material.

The state of the nanoparticle (superparamagnetic or blocked) depends on the measurement time. A transition between superparamagnetism and blocked state occurs when $\tau_{meas} = \tau$. In several experiments, the measurement time is kept constant but the temperature is varied, so the transition between superparamagnetism and blocked state is seen as a function of the temperature. The temperature for which $\tau_{meas} = \tau$ is defined as the blocking temperature T_b .⁸

For a zero magnetic field blocking Temperature, T_b , is given by:

$$T_B = \frac{K_v V}{k_B \ln(\tau_{meas} / \tau)} \quad (8)$$

Effect of a magnetic field

The model of an ideal superparamagnetic was mainly worked out by the early 1960s, but now it continues to develop.^{8, 11} The simplest variant of this model considers a system of non-interacting identical particles with the magnetic moment μ_{ef} . Since the magnetic moment of the particle is assumed to be large, its interaction with the magnetic field H is calculated without taking the quantum effects into account. In the case of isotropic particles, the equilibrium magnetization system is described by the **Langevin equation**:

$$M = N \mu_{ef} \left(\coth(\mu_{ef} H / k_B T) - k_B T / \mu_{ef} H \right) \quad (9)$$

Equation (9) has been derived with the assumption that single particles are magnetically isotropic (all the directions for their magnetic moments are energetically equivalent), but this condition is hardly ever fulfilled.

If the particles are magnetically anisotropic, the calculation of the equilibrium magnetization becomes more complicated.

When investigating the magnetic properties of the samples containing nanoparticles, the magnetization curve is usually measured up to magnetization. The B-H (or M-H) curve is anhysteretic, but still sigmoidal as shown in figure V. The remaining magnetization value after removal of external field and the coercivity are zero.

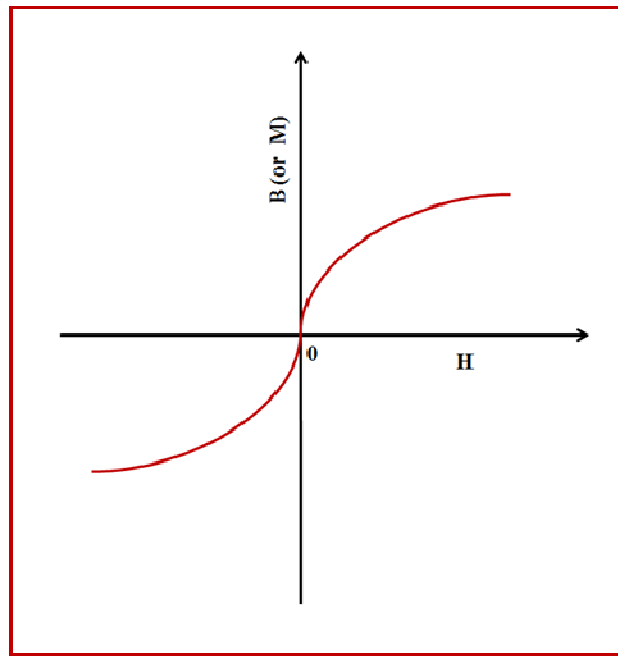


Figure V: Characteristic sigmoidal shape of B-H (or M-H) curve, with B or M approaching a saturation value for a superparamagnetic material

Zero-field cooling (ZFC) and field cooling (FC) measurements

In order to determine the temperature dependence of the magnetization M , two types of experiments are commonly carried out, namely, zero-field cooling (ZFC) and field cooling (FC). According to the ZFC procedure, the sample is cooled (usually down to the liquid helium temperature) in the absence of a magnetic field and then a moderate measuring field is applied (1 ± 100 Oe) and the temperature is gradually raised, the magnetic moment M_{ZFC} values are recorded. The FC procedure differs from ZFC only by the fact that the sample is cooled in a non-zero magnetic field “by

freezing” the alignment of the nanoparticle magnetic moments. The temperature is gradually raised in the absence of a magnetic field and the magnetic moment M_{FC} values are recorded.

For magnetic nanoparticles, the $M_{FC}(T)$ and $M_{ZFC}(T)$ curves usually coincide at relatively high temperatures but start to differ below a certain temperature T_{ir} (irreversibility temperature).

The $M_{ZFC}(T)$ curve has a maximum at some temperature T_{max} which coincides with the blocking temperature. Above this temperature value, $M_{ZFC}(T)$ curve decreases due to thermal fluctuations and the $M_{FC}(T)$ curve, most often, ascends monotonically to very low temperature. Below blocking temperature, the free movement of the magnetic moments is blocked while above T_b it is evident superparamagnetic relaxation (Figure VI).⁸

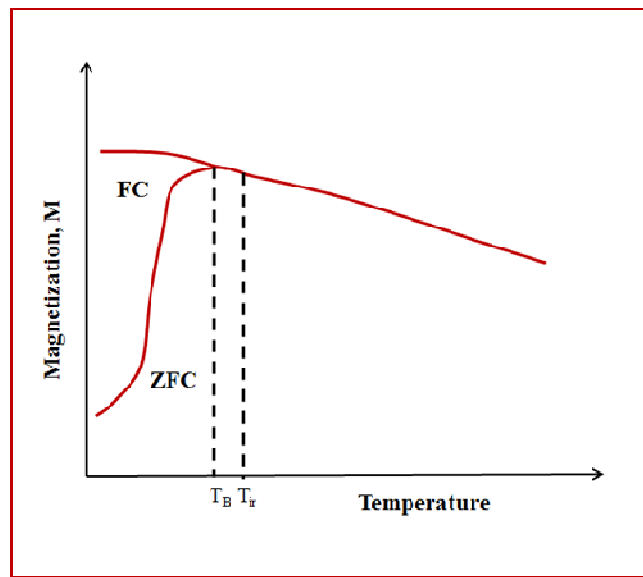


Figure VI: Temperature dependence of the magnetic moment (ZFC and FC measurements).⁸

During the ZFC process, as the temperature decreases, the potential energy tends to decrease, by aligning the magnetic moments of each particle along the magnetization preferential axis. Since the nanoparticles are randomly dispersed, at low temperature the total magnetization of the sample shows the lowest value. When the temperature increases in the presence of a magnetic field, the energy barriers are beginning to be overcome by thermal energy.

The total magnetization increases with increasing temperature and the maximum is reached when the thermal activation energy is equal to the magnetic anisotropy energy:

$$K_v V = k_B T_B \ln(\tau_{meas} / \tau) = 25 k_B T_B \quad (7)$$

where $\tau_{meas} = 100$ s (characteristic time for the static magnetic measurements) and $\tau_0 = 10^{-9}$ s.

During the FC process, when the nanoparticles are cooled in the presence of a magnetic field, the magnetization direction is “frozen” in the direction of applied external magnetic field. Below T_b , the differences between ZFC and FC measurements is due to the presence of the magnetic anisotropy energy barrier, at each temperature M_{FC} represents all the nanoparticle contribution while M_{ZFC} reflects only the magnetization of the nanoparticles whose energy barrier is exceeded by thermal energy. Starting from T_b , ZFC and FC curves overlap because the nanoparticles are thermally activated in the superparamagnetic state.

References

1. Heiman D., *Nanomagnetism*. Adv. Phys. Lab. 2009.
2. Getzlaff M. *Fundamentals of magnetism*. Berlin Heidelberg, Springer-Verlag. 2008.
3. Simon M.D., Geim A.K. *Diamagnetic levitation: Flying frogs and floating magnets*. J. Appl. Phys. 87: 6200, 2000.
4. Chen C. *Magnetism and metallurgy of soft magnetic materials*. New York: Dover Publications, Inc. 1986.
5. Elliott S.R. *The physics and chemistry of solids*. New York: Wiley. 1998.
6. Crowell B. *Simple nature*. Fullerton, California. 2008.
7. Callister W.D. *Materials Science and Engineering - An Introduction*. Fifth Edition. J. Wiley & Sons, Inc. 2000.
8. Gubin S.P., Koksharov Yu A., Khomutov G.B., Yurkov G. Yu. *Magnetic nanoparticles: preparation, structure and properties*. Russ. Chem. Rev. 74 (6): 489 - 520, 2005.
9. Pankhurst Q.A., Connolly J., Jones S.K., Dobson J. *Applications of magnetic nanoparticles in biomedicine*. J. Phys. D: Appl. Phys. 36: R167–R181, 2003.
10. Néel L., Hebd C.R. *Seances Acad. Sci.* 5 99, 1949.
11. Jacobs I.S., Bean C.P., in *Magnetism* Vol. 3 (Eds G T Rado, H Suhl) (New York: Academic Press) p. 271, 1963.

